TWIN SCREW GRANULATION: IMPROVING THE MIXING OF HYDROPHOBIC AND HYDROPHILIC POWDERS

A thesis submitted in partial fulfillment of the requirements for the degree of Doctor of Philosophy by:

Aquino L. Mundozah

Department of Chemical & Biological Engineering

The University of Sheffield

July 2019

ABSTRACT

Powders are ubiquitous to the pharmaceutical industry and represent a large proportion of formulated products i.e. granules, tablets, capsules. The quality of the formulated product is a function of the primary powder's physical properties i.e. size, shape, density, strength, morphology, wettability and granulation process parameters.

In recent years, powders which are synthesized as either excipients and/or active pharmaceutical ingredients are increasingly becoming hydrophobic (as defined by the contact angle). This property makes it difficult to design, troubleshoot and predict the wet granulation process due to the complex interactions between the liquid binder and primary powder particles.

Moreover, traditionally the granulation process is conducted in batch mode. However, efforts are being made to move to continuous twin screw granulation (TSG). Continuous TSG is attractive to the pharmaceutical industry as the equipment can be run for longer periods, thus promoting increased productivity.

Continuous TSG aids fast development of product from lab scale to pilot scale thus reducing product development time and cost to market. However, understanding of the continuous TSG process and its interplay with complex hydrophobic powders is not well understood to enable effective development of process design space to yield product with desired quality attributes i.e. uniformity, flowability, strength, stability etc.

The primary objective of this thesis was to improve understanding on how the initial interaction between the liquid binder and primary powder particles influence the granulation mechanisms taking place in TSG when using a hydrophobic component in the formulation composition. Experimental investigations were two-fold (1) initial static liquid-primary powder interactions and (2) dynamic mixing in continuous TSG.

Initially a study of spreading of single liquid droplets on powder beds is investigated from an experimental and theoretical point of view, paying particular attention to competing spreading mechanisms. The existence of two competing single liquid droplet spreading mechanisms on powder beds is shown: a) d_h spreading describes the length the liquid droplet travels horizontally across the powder bed and b) the d_v imbibition is the length the liquid droplet travels vertically into the powder bed. The spreading mechanisms are distinct from

those reported in literature because the d_h spreading is shown to be dominant when spreading is driven by capillary forces resulting in fast wetting and nucleation kinetics. In contrast, the d_v imbibition is shown to be dependent on interfacial tension between the solid and the liquid droplet where the wetting and nucleation kinetics are slow.

Experimental findings are presented on the dependence of the equilibrium contact angle on the chemical composition of the powder bed. It was found that the experimental data is inconsistent with existing Cassie-Baxter model for two-component mixtures. A new dimensionless surface coverage wetting model that predicts the contact angle behavior of two-component mixtures has been proposed. The key aspect of the model is the consideration of particle surface coverage and its relation with the contact angle behavior. In fact, it is believed that this proposed theory is necessary as mixtures consist of components with different particle sizes making surface coverage of one constituent over another inevitable.

Finally, the static liquid-powder bed behavior was linked to 'real' continuous TSG to assess how key granulation mechanisms (wetting & nucleation, consolidation & coalescence and breakage & attrition) affect mixing and segregation behavior within the TSG process. This link was achieved by using: a) specific mechanical energy and proposed dimensionless mixing number and b) results from Residence Time Distribution and Near Infra-Red Chemical Imaging.

When the static behavior between the liquid droplet and powder bed particles was driven by capillary forces this led to more rapid granulation resulting in greater extent of granulation and formation of stronger granules. However, in the interfacial tension driven regime the granulation behavior was very slow resulting in larger amounts of un-granulated fines. Granulation in this regime was successful when mechanical dispersion was applied as the stress was able to force the distribution of the liquid binder through the powder bed, resulting in improved granule properties i.e. extent of granule formation and strength.

This contribution is expected to make it possible to design, control, troubleshoot and optimize the TSG granulation process, to allow for better control of final granular properties.

"It always seems impossible until its done"

Nelson Mandela

ACKNOWLEDGEMENTS

PUBLICATIONS FROM THIS RESEARCH

- Mundozah, A.L., Catwright, J.J., Tridon, C.C, Hounslow, M.J., Salman, A.D., (2017) **Development of a mapping approach for TSG powder flow regimes**, 8th International Granulation Workshop.

- Mundozah, A.L., Catwright, J.J., Tridon, C.C, Hounslow, M.J., Salman, A.D., (2018) **Hydrophobic/Hydrophilic Powders: Competing Horizontal Spreading and Vertical Imbibition mechanisms of single droplet**, Powder Technology, 330, 275-283.

- Mundozah, A.L., Catwright, J.J., Tridon, C.C, Hounslow, M.J., Salman, A.D., (2019) **Hydrophobic/Hydrophilic Powders: Practical Implications of Screw Element Type on the Reduction of Fines in Twin Screw Granulation**, Powder Technology, 341, 94-103.

- Mundozah, A.L., Catwright, J.J., Tridon, C.C, Hounslow, M.J., Salman, A.D., (2019) **Wetting of binary powder mixtures** , International Journal of Pharmaceutics, In press.

- Mundozah, A.L., Yang, J., Catwright, J.J., Tridon, C.C, Hounslow, M.J., Salman, A.D., (2019) **Assessing Particle Segregation using Near-Infrared Chemical Imaging in Twin Screw Wet Granulation**, International Journal of Pharmaceutics, In press.

TABLE OF CONTENTS

SYMBOLS AND ACRONYMS

The following list of symbols and acronyms contains the most nomenclature. Additions to this nomenclature are given in the text of the thesis.

Latin Symbols

Symbol	Meaning	Units
C	Concentration	$[\text{mol m}^{-3}]$
d	Diameter	$[\text{m}]$
d_h	Horizontal spreading of the liquid droplet	$[\text{m}]$
$d_h\text{max}$	Maximum horizontal spreading diameter on the powder bed surface	$[-]$
d_{nuclei}	Nuclei diameter after complete liquid droplet imbibition into the powder bed surface	$[\text{m}]$
d_0	Initial liquid droplet diameter	$[\text{m}]$
d_v	Vertical Imbibition of the liquid droplet	$[\text{m}]$
$d_{3,2}$	Sauter mean diameter	$[\mu\text{m}]$
d_{50}	Mean granule/particle size	$[\mu\text{m}]$
D_L	TSG barrel length	$[\text{m}]$
$E(t)$	Residence time function	$[-]$
f	Area fraction of components	$[-]$
f_{SC}	Fractional surface coverage	
g	Gravitational acceleration	$[\text{m}^3\text{kg}^{-1}\text{s}^{-2}]$
h	Height	$[\text{m}]$
h_0	Initial liquid droplet thickness	$[\text{m}]$
K	Nucleation ratio	$[-]$
L/D	Axial length to diameter ratio of the TSG	$[\text{m}]$
L/S ratio	Liquid to solid ratio	$[-]$
l_c	Capillary length	$[\text{m}]$

$\dot{m}_p$	Mass flow rate of the powder	$[\text{kg s}^{-1}]$
n	Screw speed	[rpm]
p	Plug flow fraction	$[-]$
p_2	Projected area of small particles	
r	Liquid droplet radius	[m]
r_e	Equilibrium liquid droplet contact radius	[m]
s_1	Surface area of larger particles	
t	Time	[s]
t_0	Initial time delay of the liquid droplet spreading process	[s]
t_1	Time the tracer is first detected	[s]
t_{out}	Time tracer is first out	[s]
t_{CDA}	Liquid droplet imbibition for constant drawing area case	[s]
t_{DDA}	Liquid droplet imbibition for decrease drawing area case	[s]
t_{dp}	Liquid droplet imbibition time	[s]
$\bar{t}_m$	Mean residence time	[s]
t_{max}	Time required to reach d_{max}	[s]
T	Torque	[N m]
U	Velocity	$[\text{m s}^{-1}]$
v_D	Darcy rate of imbibition	$[\text{s}^{-1}]$
$\bar{v}_D$	Adimensional imbibition rate	$[\text{s}^{-1}]$
V	Volume	$[\text{m}^3]$
V_o	Initial drop volume	$[\text{m}^3]$
V_{cap}	Volume of the liquid droplet based on spherical approximation	$[\text{m}^3]$
V_{free}	Free volume	$[\text{m}^3]$
V_t	Volume of the liquid drop remaining on the powder bed surface at a specific time	$[\text{m}^3]$
W	Work of adhesion or cohesion	$[\text{m N m}^{-1}]$

Greek Symbols

Symbol	Meaning	Units
γ	Surface tension	$[\text{N m}^{-1}]$
ε	Porosity of powder bed or granule	$[-]$
θ	Liquid-solid contact angle	$[°]$
θ_E	Equilibrium contact angle	$[°]$
θ^*	Apparent contact angle	$[°]$
θ_D^*	Dynamic contact angle	$[°]$
θ_i^*	Dimensionless apparent contact angle calculated based on spherical cap approximation	$[-]$
$\overline{\cos\theta^*}$	Normalised contact angle	
ρ	Bulk density	$[\text{kg m}^{-3}]$
μ	Dynamic liquid viscosity	$[\text{N s m}^{-2}]$
υ_D	Darcy rate of imbibition	
$\bar{v}_D$	Adimensional imbibition rate	
φ	Twin screw granulation fill level	$[-]$
ϕ	Volume fraction	$[-]$
ϕ_c	Critical volume fraction	$[-]$
$\varnothing$	Shape factor	
$\varnothing_p$	Shape factor of primary particle	
Ψ	TSG back mixing	$[\%]$

Acronyms

Symbol	Meaning
CE	Conveying element
lCE	Large conveying element
fCE	Fine conveying element
DP	Demixing potential
EDN	Energy density number
KE	Kneading element
ME	Mixing element
NIR $-$ CI	Near Infra-red chemical imaging
PFN	Powder flow number
RT	Residence time
RTD	Residence time distribution
TME	Tooth mixing element
SME	Specific mechanical energy
TSG	Twin screw granulation

Subscripts

Symbol	Meaning
A	Adhesion
C	Cohesion
L	Liquid
P	Powder
S	Solid
V	Vapour

LIST OF FIGURES

xviii

LIST OF TABLES

1   AN OVERVIEW OF WET GRANULATION

1.1   Introduction

Wet granulation is a size enlargement process whereby primary particles are made to adhere together to form larger aggregates in the form of granules [1]. This process occurs through addition of a liquid binder to a bed of particles under constant agitation. During the size enlargement process, the actions of capillary and viscous forces will encourage the formation of temporary liquid bridges, where-after permanent solid bridges are formed from drying the granules. The wet granulation process plays a crucial role in many applications for various industries including pharmaceutical, detergent, agricultural, food and chemical.

The continued interest in the wet granulation process for the various industries is due to its advantages of improving powder flowability, reducing caking, lump, dust formation and particle segregation which are useful in increasing productivity, reducing production cost and product rejection [2]. However, wet granulation is a complex process which makes manufacturing of reproducible product with desired properties difficult, especially in the pharmaceutical industry where the formulations are comprised of ingredients with different chemical compositions (hydrophilic/hydrophobic) [3]. Therefore, thorough understanding of the wet granulation process is required to enable effective formulation development and adequate process design when using more challenging formulations.

1.2   Mechanisms

A multitude of wet granulation equipment exists, choice of which depends on the desired granule properties. Typically, granulation equipments are commonly classified by the way in which the powder is agitated: fluidized bed granulators, tumbling granulators (pan or drum) and mixer granulators (batch high-shear and continuous twin screw granulation "TSG") [4]. The science of granulation in these equipments has been explained through use of three key mechanisms which determined the final granule attributed [2]:

- **Wetting and Nucleation**: Wetting is a process whereby the liquid binder is initially brought in contact with the powder bed to form nuclei (primary granules) which are often loosely held. The liquid binder is distributed in the granulator using agitation.

- **Consolidation & Coalescence**: The wet nuclei are deformed and densified when colliding with neighboring granules and granulator surface. This process will force the liquid to migrate to the outer granule surface to allow coalescence and consolidation, forming larger granules. Coalescence occurs if the adhesive forces between the colliding granules are large enough to overcome the agitation separation force and the rebound kinetic energy. The colliding process promotes densification of granules though consolidation.

- **Attrition & Breakage**: When the collision stress exceeds a critical value of which the granules can withstand, granule breakage and attrition occurs resulting in smaller granule fragments. This mechanism alters the granule size distribution and other properties e.g. strength which are undesirable in some applications.

In batch granulation, these mechanisms are described as occurring simultaneously within the process. However, TSG is a regime separated process with the granulation mechanisms occurring one after the other along the length of the barrel channel [5]. Although these mechanisms are well accepted in wet granulation, problems related to granulation of challenging formulations e.g. hydrophobic are difficult to fix due to the complexity involved in the interactions of the liquid binder and primary powder particles. This complexity is currently a major aspect researchers are working towards in order to move granulation approach from art to science so as to reduce the extensive experimental investigations which are often performed to determine which conditions result in desired granule properties.

1.3 Thesis Objectives

Fundamental challenges in wet granulation have been to conquer the segregation and preferential wetting problems, which are notable when using hydrophobic powders in the formulation composition as a result of the powders' poor wetting properties. These challenges are difficult to fix, mostly because our fundamental understanding of the granulation mechanisms when using hydrophobic powders is lacking. This makes it difficult to understand, control and troubleshoot the TSG process.

Studying the granulation mechanisms is challenging, due to the vast amount of complexity involved with regards to the interactions between the liquid binder and solid particles and granulation mixing considerations. As such, our fundamental understanding of continuous TSG

process does not meet industrial needs, representing a serious gap in the knowledge required to design, control and optimize the continuous TSG process.

The primary objective of this thesis was to improve understanding on how the initial interaction between the liquid binder and primary powder particles influence the granulation mechanisms taking place in TSG when using a hydrophobic component in the formulation composition.

To meet this objective, several steps were taken:

1. Examine literature on hydrophobic powders, focusing on granulation mechanism and existing theories.
2. Challenge existing theories on wetting of hydrophobic powders and propose new theories based on experimental investigations, taking into consideration the cohesive and adhesive interactions between the liquid and primary powder particles.
3. Relate the observed wetting behavior to 'real' granulation behavior by, performing carefully designed experiments to better understand how liquid binder and primary powder particles properties and TSG operating variables affect the dominant granulation mechanisms taking place and the resultant granular properties.

The ultimate goal of this thesis is to gain an insight into the micro-level physics of wetting and relate this to the 'real macro-level' granulation behavior, in order to provide a knowledge foundation by which it is possible to design, control and optimize the wet granulation process.

1.4 Thesis Outline

To achieve the objectives detailed above, experimental investigations were performed using different liquid binder and primary powder properties and TSG process variables:

- **Chapter 2**, a literature summary of current understanding on powder wetting phenomena and TSG is given.
- **Chapter 3**, the details of the material properties and methodologies used are provided.
- **Chapter 4**, competing spreading mechanisms of a liquid droplet impacting on static powder beds are investigated. Experimental results are then compared to existing

3

theories describing horizontal spreading and rate of imbibition of the liquid droplet into powder bed surface.

- **Chapter 5** is a continuation of Chapter 4, the static contact angle is used to characterize the wetting behavior of two-component powder systems. The experimental results are compared to existing theory and a novel contact angle model is presented which allows for excellent prediction of static contact angle for particulate powder mixtures.

- **Chapter 6** the influence of liquid and powder properties on the TSG process is shown to be described using a single parameter, specific mechanical energy by studying TSG mass hold-up, defined as the amount of material remaining in the TSG barrel and extent of granule formation 'yield', granule strength. A TSG mapping approach is presented which links the wetting behavior of the powder bed with 'real' granulation behavior. The product yield impacts production costs as in the pharmaceutical industry, the aim is always to maximize yield and minimize the production loss and reduce the recycling ratio.

- **Chapter 7**, there is a black box approach to the arrangement of the screw elements in the screw configuration in most of the work reported in the TSG area. In order to move beyond this 'black box approach', this chapter attempts to rationalize the positioning of various screw elements along the TSG barrel length by studying reduction in un-granulated fines, the granule size, granule porosity, liquid binder and residence time distribution results.

- **Chapter 8**, Near Infra-Red Chemical Imaging is utilized to study particle segregation phenomena in TSG. A TSG segregation regime map is proposed which links the dispersion energy by shear force using a proposed dimensionless mixing number and particle de-mixing behavior in TSG. The regime mapping approach suggests how to rationally design and control the TSG process in order to minimize content un-uniformity in the final granular product.

- Finally, in **Chapter 9**, the conclusions and future recommendations are detailed.

2   LITERATURE REVIEW

The investigations of wet granulation of hydrophobic powders has been two-fold, focusing on the initial static liquid-primary powder interactions and then linking this behaviour to the dynamic mixing in TSG. In this section, literature on the two aspects: a) powder wetting and b) TSG are reviewed to identify knowledge gaps with respect to wet granulation of hydrophobic powders.

2.1   Powder Wetting Phenomena

The initial wetting and nucleation stage in wet granulation involves the addition and distribution of the liquid binder on a powder bed inside the granulator to form initial nuclei. The liquid binder can be added as either a solid or a liquid (spraying or pouring directly into the powder bed). Efficient wetting of the powder bed requires successful liquid binder deposition, sufficient spreading and coverage of the primary powder particles, as this step assumes that the powder bed displays good wetting behaviour [2]. However, this is not always the case as the structural complexity of new drug molecules means that it is common for entire classes of drug compounds to be hydrophobic [3].

Granule formation and the resultant granular attributes are fundamentally dependent on the wetting properties of the formulation and granulation processing conditions. Powder wetting and liquid distribution uniformity is significant in the initial wetting and nucleation stage in order to produce homogenous granules with a narrow size distribution [6]. These properties are essential for improved product quality as particle segregation may also occur, if there is preferential wetting of one constituent over another inside the granulator. It is for this reason that the wetting and nucleation stage has been subject to a lot of research especially in granulation of hydrophobic powders.

In the wetting and nucleation zone the first critical process to consider during formulation development in the pharmaceutical industry is the initial nuclei formation which is a function of wetting thermodynamics and kinetics [7]. Thermodynamic studies are used to determine whether or not wetting is energetically favourable and have focused on the contact angle formed between the liquid and powder bed surface and spreading coefficients of the liquid over the powder bed or vice versa. Wetting kinetics studies have focused on the spreading dynamics and imbibition of the liquid into the powder bed. These aspects are prone to physical and

chemical changes occurring on the powder bed surface [2]. The following sections discusses the aspects of wetting thermodynamics and kinetics in more detail.

2.2 <u>Contact Angle</u>

When a liquid droplet comes into contact with the powder bed surface, the liquid droplet wets the powder bed surface. This wetting phenomenon is determined by the interactions between the molecules of the two phases coming into contact, forming a three-phase contact line, where the liquid, powder bed surface and vapour co-exist. The three-phase contact line will continue to advance to an equilibrium contact angle (θ_E) in which the liquid droplet takes the shape that minimizes the total free energy of the system, (see Figure 2-1).
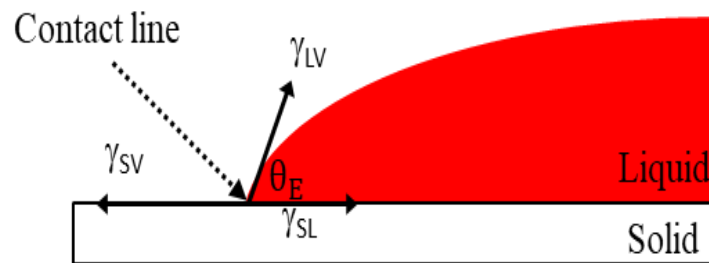
Figure 2-1. Cross sectional contact angle profile of a liquid droplet on a solid surface at a three-phase contact line.

where γ_{SL}, γ_{SV} and γ_{LV} are the three-interfacial tensions: solid-liquid, solid-vapour and liquid-vapour respectively.

A well-known relation for θ_E was developed by Young [8] assuming an idealized smooth and homogeneous solid surface and that the liquid droplet does not spread further after reaching its equilibrium contact line radius. Young [8] proposed that the equilibrium contact angle of a liquid droplet resting on a solid surface is determined by the three interfacial tensions involved in the wetting process: solid-liquid, solid-vapour and liquid vapour using the expression:

$$\cos \theta_Y = \frac{\gamma_{SV} - \gamma_{SL}}{\gamma_{LV}}$$

Equation 2-1

where θ_Y is the ideal (Young) contact angle.

A liquid is said to wet a surface $\gamma_{SV} - \gamma_{SL} \geq \gamma_{LV}$ ($\cos \theta \leq 1, \theta = 0$) and non-wetting if

$\gamma_{SV} < \gamma_{SL}$ ($\cos\theta$ is negative).

However, in reality solid surfaces are not ideal and have some imperfections, particularly pharmaceutical powders where there are several factors that affect the measured apparent contact angle (θ^*) such as contact line surface heterogeneities (roughess), chemical composition of the liquid and solid surface [9–12].

Wenzel [9] first related the θ^* to solid surface heterogeneities assuming that the liquid droplet fills the grooves of a rough solid surface completely using a simple expression (see Figure 2-2):

$$\cos\theta^* = r_{sf} \cdot \cos\theta_Y$$

Equation 2-2

where r_{sf} is the surface roughness, defined as the ratio of the true surface area to the projected area.
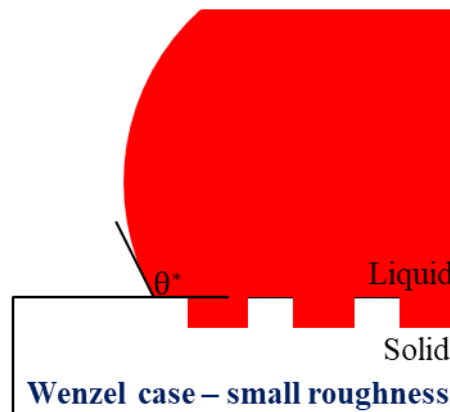
Figure 2-2. Wenzel's assumption.

Wenzel's theory was developed on the basis of earlier work of Gauss [13]. In summary, Gauss reported that surface energy was related to the liquid-solid contact area as a result of the existence of attractive forces in a liquid. Wenzel applied this concept in relation to the contact angle on rough surfaces and proposed that on a hydrophilic solid surface, surface roughness enhances its wetting behaviour since there is a greater net energy decrease to induce spreading. In hydrophobic powder beds, the non-wetting behaviour of a solid surface is exaggerated with surface roughness. However, Wenzel's theory is valid for one-component solid systems. In the pharmaceutical industry, solid systems are however frequently mixtures.

For two-component mixtures Cassie-Baxter [10] related the apparent contact angle with the wetted fraction of surface area of a solid based on the assumption that the solid surface is smooth and consists of a grid of cylinders using the following expression, (see Figure 2-3):

$$\cos \theta^* = f_1 \cos \theta_1^* + f_2 \cos \theta_2^*$$

$$f_1 + f_2 = 1$$

<div align="right">**Equation 2-3**</div>

where f_1 and f_2 are the area fractions of component 1 and 2, θ_1^* and θ_2^* are the apparent contact angles of component 1 and 2 respectively.
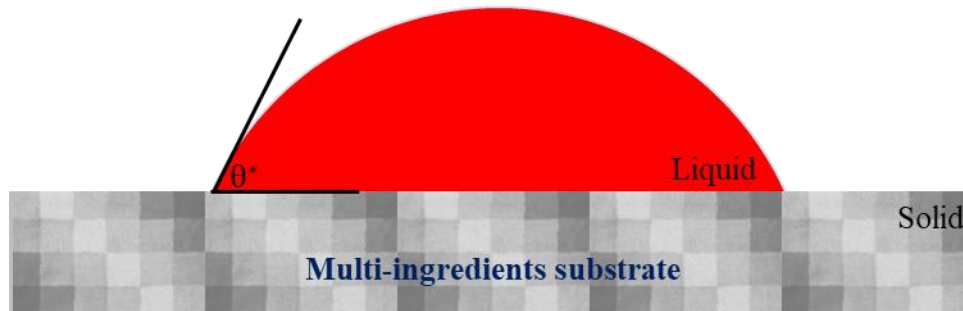
Figure 2-3. Cassie-Baxter's assumption on wetting on heterogeneous surface.

There are a number of limitations with the Cassie-Baxter approach: a) in practise real solid surfaces do not consist of cylindrical particles and have complex pore structures in which the liquid droplet is able to spread on the solid surface and fill the pores in any direction and b) Cassie and Baxter studied systems in which the components were not free to rearrange and so the surface fraction of each component was fixed and simple to determine.
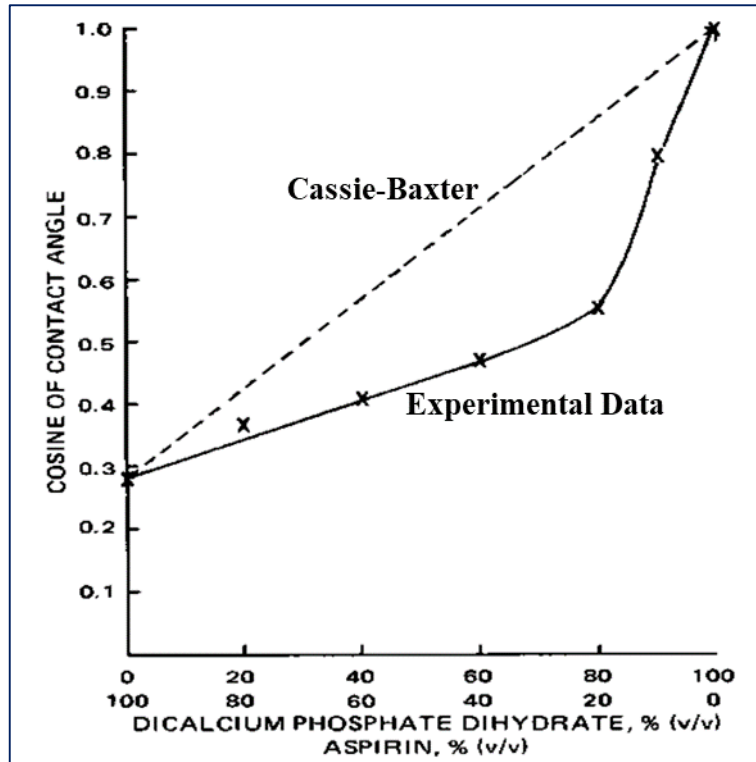
Figure 2-4. Comparison of measured cos θ* for di-calcium phosphate (hydrophilic) and aspirin (hydrophobic) versus predicted Cassie-Baxter values of Equation 2-3 [14].
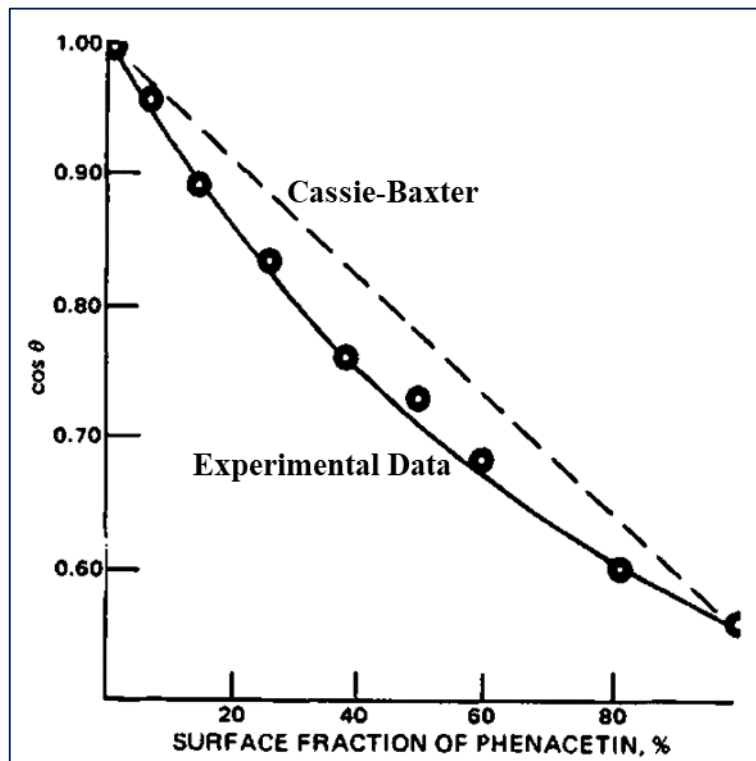
Figure 2-5. Comparison of measured cos θ* for microcrystalline cellulose (hydrophilic) and phenacetin (hydrophobic) versus predicted Cassie-Baxter values of Equation 2-3 [15].

9

The Cassie-Baxter theory has been found to be invalid for experimental data reported in a majority of publications investigating its use in predicting contact angle behaviour on solid surface with complex pore structures consisting of hydrophilic and hydrophobic particles, (see Figures 2-4 - 2-5) [3,14–17]. These publications have concluded that when the size of the heterogeneities (surface roughness) of the solid surface become larger, $r_{sf} \leq 1$ the dominance of the hydrophobic component is over exaggerated then the contact angles will become invalid to Cassie-Baxter theory. This is not a new contention; it is essentially the same point that was made in Wenzel's theory Equation 2-2.

Although the Wenzel and Cassie-Baxter theories are widely used to predict contact angle behavior, several authors have questioned the validity of the Cassie-Baxter theory and suggested that the three-phase contact line alone and not the interfacial contact area is important in determining the contact angle behavior [18,19]. This result was explained to be due to the different behavior of solid molecules in comparison to liquid molecules. At the three-phase contact line, solid molecules are not mobile and cannot contact to obey area minimization when a liquid droplet is placed on them. Put simply, the laws of liquids cannot be directly applied to solids. In this thesis, an attempt is made to correct the misconceptions of Cassie-Baxter theory.

The expressions of Wenzel and Cassie-Baxter were proposed based on the assumption that the size of the powder bed surface roughness is smaller than the initial size of the liquid droplet used and that the liquid droplet will reach an equilibrium contact line radius. However, according to Marmur [20], for real powder bed surfaces θ may change from one point to another on the three-phase contact line, (see Figure 2-6). This range of θ is referred to as advancing contact angle (θ_a) and receding contact angle (θ_r), where $\theta_a > \theta_r$. The difference between θ_a and θ_r yields a phenomenon termed contact angle hysteresis ($CAH \equiv \theta_a - \theta_r$) (see Figure 2-6).
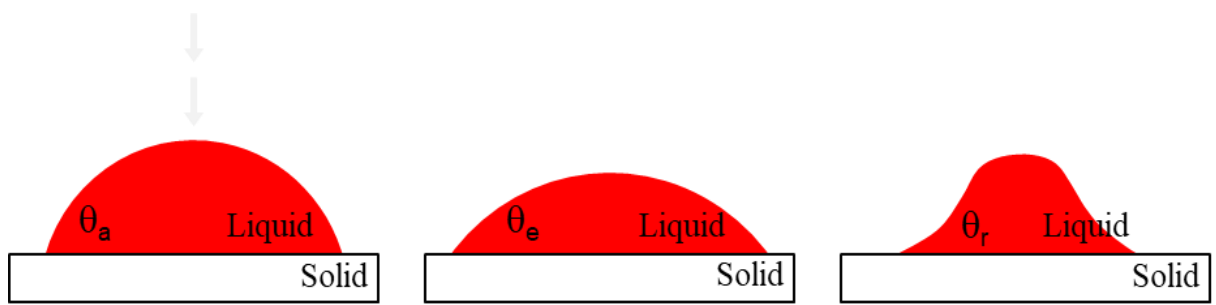
Figure 2-6. Different types of contact angles $\theta_a > \theta^* > \theta_r$.

The significance of CAH has been extensively investigated and concluded to arise from either kinetic, CAH changes with time and/or thermodynamic effects e.g. powder bed surface roughness and chemical composition. However, accurate measurements of θ_a and θ_r are very difficult and require considerable amounts of effort due to liquid droplet imbibition into the powder bed and evaporation [13]. This results in the θ^* of a liquid droplet resting on a powder bed surface being the only measurable contact angle for these powder bed surfaces [20]. According to Tadmor (2004), $\cos\theta_\gamma$ can be calculated from θ_a and θ_r [21]. However, estimating contact angles on non-ideal surfaces is meaningless in terms of Young's equation as there is no contact angle hysteresis observed on real powder bed surfaces.

In real granulation systems, the dynamic contact angle (θ_D^*) defined as the contact angle formed between the liquid droplet and powder bed under agitation, is a function of the moving contact line. An experimental relationship for θ_D^* was proposed by Joos et al. [22]:

$$\cos\theta_D^* = \cos\theta^* - 2(1 + \cos\theta^*)Ca^{\frac{1}{2}}$$

Equation 2-4

$$Ca = \frac{\mu U}{\gamma_{LV}}$$

Equation 2-5

where Ca is the capillary number, U is the liquid droplet flow velocity and μ is the viscosity of the liquid.

However unlike static contact angles, the moving contact line makes it difficult to describe θ_D^* as a powder bed surface property as constant agitation during granulation has been shown to assist in wetting of the powder bed by the liquid binder [23,24]. Therefore, in this thesis the static θ^* is utilised to describe the wettability of the powder bed surface.

2.3 <u>Wetting Energies</u>

The wetting and non-wetting states of a three-phase contact line can be described using surface energies. When a liquid droplet contacts a powder bed surface, a new surface is formed as they come into contact. According to Rowe [25], the formation of a new surface occurs when

11

the cohesive forces of the liquid molecules are displaced by the adhesive forces of the liquid and powder bed surface, (see Figure 2-7).
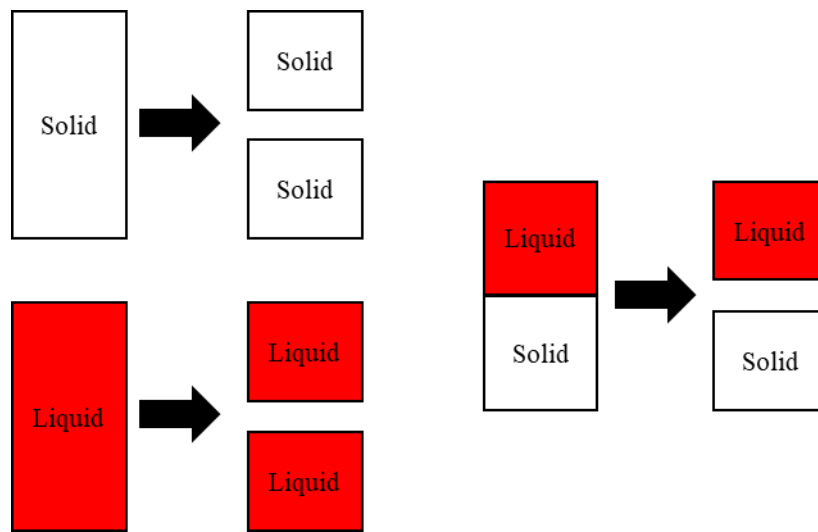
Figure 2-7. Works of cohesion and adhesion.

The work of cohesion (W_C) is defined as the work required for separating a unit area of a material from itself.

Work of cohesion of a powder bed surface (W_{CS}):

$$W_{CS} = 2\gamma_{SV}$$

Equation 2-6

Work of cohesion of a liquid (W_{CL}):

$$W_{CL} = 2\gamma_{LV}$$

Equation 2-7

However, the work of adhesion is defined as the work required to separate a unit of an interface of two materials held together.

Work of adhesion of a liquid and powder bed surface:

$$W_A = \gamma_{SV} + \gamma_{LV} - \gamma_{SL} = \gamma_{LV}(\cos\theta^* + 1)$$

<div align="right">**Equation 2-8**</div>

The competition between W_A and W_C determines the resultant contact angle behaviour. This relationship is represented by a simplified version of Young's equation:

$$\cos\theta_Y = \frac{2W_A}{W_C} - 1$$

<div align="right">**Equation 2-9**</div>

The difference between W_C and W_A gives the spreading coefficient (λ) which defines the tendency of a liquid and powder bed particles to spread over each other [26]. Essentially, λ provides information on whether the replacement of γ_{SV} interface with γ_{SL} interface will be thermodynamically favourable. The W_C and W_A are important in predicting the type of interaction the liquid will have with the powder bed. This will have an effect on the initial primary nuclei formed and subsequent resultant granular properties.

There are three possibilities of liquid-over powder bed/powder bed over liquid spreading [25]:

When λ_{LS} is positive, the liquid will spread over the powder bed particles. In granulation this results in the formation of temporary liquid bridges between the contacting particles and subsequent drying creates strong dense granules.

This is behaviour is represented as:

$$\lambda_{LS} = W_A - W_{CL} \text{ or } \lambda_{LS} = \gamma_{LV}(\cos\theta^* - 1)$$

<div align="right">**Equation 2-10**</div>

When λ_{SL} is positive, the powder bed particles may spread or adhere to the liquid in a process termed solid-spreading nucleation, where bonds are formed were the liquid and powder bed particles initially touch. This phenomenon is observed when the granules formed are a result of a layer of small hydrophobic powder bed particles spreading over the surface of a larger liquid droplet. The resultant granules are very porous (hollow) with fewer and weaker bonds.

This behaviour is represented as:

$$\lambda_{SL} = W_A - W_{CS} \text{ or } \lambda_{SL} = -2\gamma_{SV} + \gamma_{LV}(\cos\theta^* + 1)$$

When λ_{LS} and λ_{SL} are negative, both the liquid and powder bed particles have high works of cohesion. This means that no spreading/wetting occurs because the liquid molecules/ powder bed particles stick together due to mutual attraction.

Although the spreading coefficient theory has been successfully applied in the wet granulation process to predict liquid affinity to powder bed particles, fundamental problems exist particularly with the techniques used to acquire the surface energy values. These techniques are very diverse, however information acquired highly depends on the method used. This makes the use of the resultant experimental data in predictions to give varied results. Rather than rely on the spreading coefficient theory alone, it is suggested that other factors which determine the behaviour of the liquid affinity to powder bed particles should be taken into consideration i.e. contact angle, spreading dynamics etc.

2.4 Nucleation Thermodynamics: Kinetics of Nuclei Formation

2.4.1 Spreading Dynamics of a Liquid Droplet on a Powder Bed

Figure 2-8 illustrates the possible outcomes, when the liquid droplet is placed on a solid surface [27]. When inertia is rapidly dissipated, the liquid droplet will immediately spread to form a thin film. This behaviour is typically observed for high works of adhesion (see Equation 2.8). The liquid droplet will attain its equilibrium θ^* once the force balance between gravity, capillary and viscous forces is reached when $\gamma_{SV} = \gamma_{SL}(\cos\theta^* = 0)$. However, inertia may cause the liquid droplet to rebound, splash and break, forming secondary liquid droplet in the case of when $\gamma_{SV} < \gamma_{SL}(\cos\theta^*$ is negative).
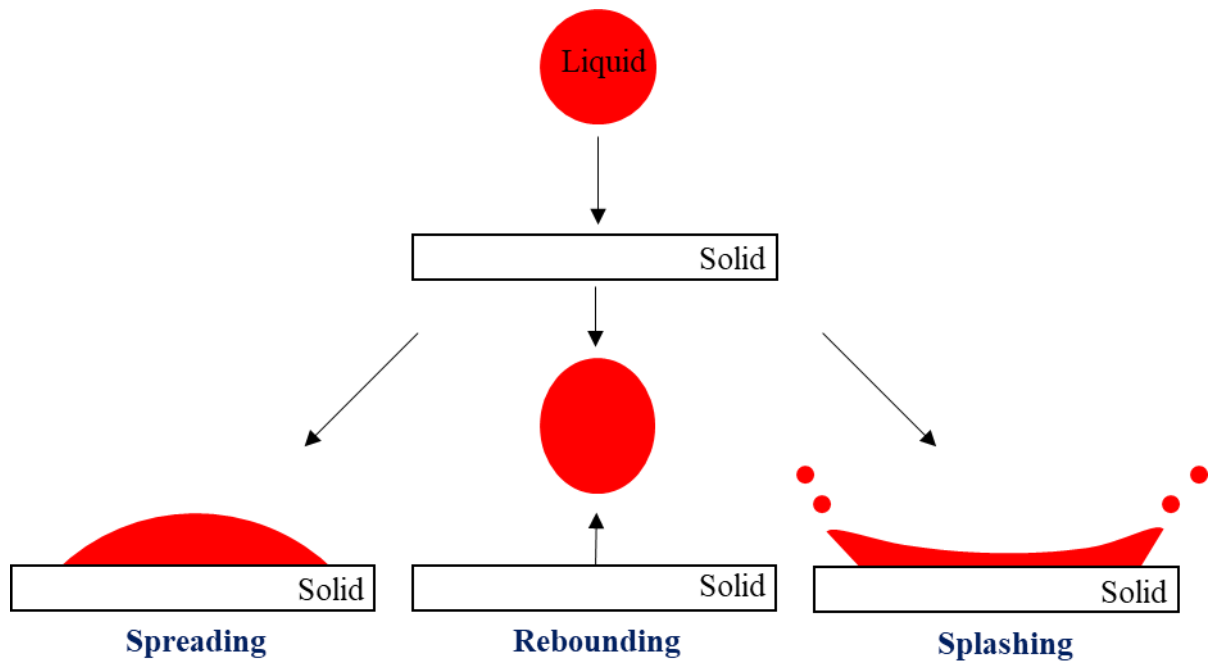
Figure 2-8. Single liquid droplet impacting on powder bed.

The liquid droplet spreading dynamics have been described using the dimensionless parameters (see Equation 2-12 - 2-16) [28]. The Reynolds number (Re) Equation 2-12 compares the liquid droplet inertia effects to the viscous forces. Reynolds number shows that if it decreases, highly viscous liquid droplets will spread to a lesser extent on the powder bed. The importance of inertia to surface energy is expressed in the Weber number (We) (Equation 2-13). As We increases the inertia effects dominate which causes the liquid droplet to rebound. Ohms number (Oh) (Equation 2-14) incorporates the relative effect of viscous, inertia and surface tension forces. Gravity effects are described using the Bond number (Bo) (Equation 2-15) and Froude number (Fr) (Equation 2-16).

$$Re = \frac{\rho_L U d_0}{\mu}$$

Equation 2-12

$$We = \frac{\rho_L U^2 d_0}{\gamma_{LV}}$$

Equation 2-13

$$Oh = \frac{\sqrt{We}}{Re}$$

<div align="right">**Equation 2-14**</div>

$$Bo = \frac{\rho_L g d_0{}^2}{\gamma_{LV}}$$

<div align="right">**Equation 2-15**</div>

$$Fr = \frac{U^2}{g d_0}$$

<div align="right">**Equation 2-16**</div>

where ρ_L is the liquid droplet density and g is the gravity.

However, gravity effects are considered negligible during liquid droplet impact, as the liquid droplet radius used for studying static powder bed interactions are typically less than the capillary length (l_c) given as:

$$l_c = \sqrt{\frac{\gamma_{LV}}{\rho_L g}}$$

<div align="right">**Equation 2-17**</div>

Generally, the liquid droplet spreading process for these droplets always increases with decrease in capillary number (see Equation 2-5).

Most experimental analyses assume that when the gravitational effects are negligible, the liquid droplet takes the shape of a spherical cap when in contact with the powder bed, once it has reached its equilibrium. The volume of the spherical cap (V_{cap}) is related to the liquid droplet height (h) and its radius (r) via:

$$V_{cap} = \frac{1}{6}\pi h(3r^2 + h^2)$$

<div align="right">**Equation 2-18**</div>

For a given volume, the shape of the liquid droplet on the solid surface is directly correlated to θ^* using the expression [29]:

$$\theta_i^* = \frac{4V_0}{\pi r^3}$$

<div align="right">**Equation 2-19**</div>

where πr^3 is the wetted area of the solid surface.

Note: Equation 2-19 gives θ_i^* in its dimensionless form.

 Experimental analysis has shown that the liquid droplet radius increases linearly with time $(r(t))$ in the earlier stages of the liquid droplet spreading process, however $r(t)$ will reach a plateauing region where it will slow. The earlier relation of $r(t)$ is commonly given by :

$$r(t) \approx \left(\frac{10\gamma_{LV}}{9A\mu} \left(\frac{4V_0}{\pi}\right)^3 t \right)^{0.1} \propto t^n$$

<div align="right">**Equation 2-20**</div>

where A is a constant determined experimentally and t is time.

Equation 2-20 is commonly referred to as the Tanner spreading law, which predicts a power law scaling relationship of the initial liquid droplet spreading on a powder bed with time [30]. Tanner's relation is expressed in terms of either the dynamic contact radius $r(t)$ or contact angle θ^* via:

<div align="center">17</div>

$$r \sim t^{0.1}$$

$$\theta^* \sim t^{-0.3}$$

Tanner's law has been successfully applied to describe the evolution of $r(t)$ for various powder beds and liquid droplet model systems [31–33]. However, Tanner's derivation does not consider λ, a measure of the tendency of a liquid droplet and powder bed particles to spread over each other. The λ would essentially be the driving force for the spreading process.

According to de Gennes [12] , the liquid droplet spreading process is driven by a balance between viscous dissipation and surface energies occurring near the three-phase contact line. If the liquid droplets are small i.e. less than the capillary length (see Equation 2-17), the surface energy of the γ_{SL} and γ_{LV} interface only need to be considered [29]:

$$F_s = \frac{4V_0{}^2 \gamma_{LV}}{\pi r^4} - \pi \lambda_{LS} r^2$$

where F_s is the surface free energy.

In practise, when $\lambda_{LS} > 0$ the liquid droplet will spread over the powder bed. This is expected to lead to a reduction in surface free energy, however the surface energy $\pi \lambda_{LS} R^2$ cannot be directly converted to actual hydrodynamics of the liquid droplet [12,29]. Instead, the wetting process is preceded by the initial formation of a thin film around the liquid droplet, (see Figure 2-9).
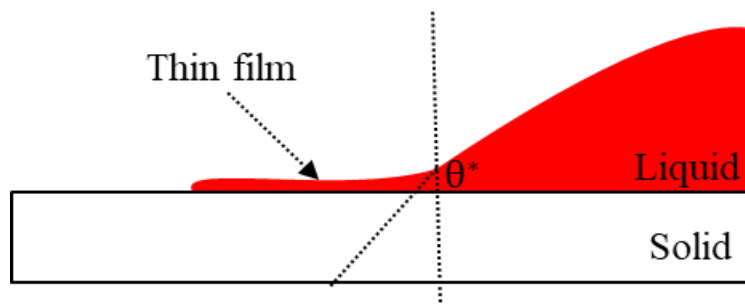
Figure 2-9. Liquid droplet profile of an advancing contact line.

As the liquid droplet is advancing on the powder bed, the formation of the thin film uses up the energy corresponding to $\pi\lambda_{LS}r^2$, that could have gone towards the liquid droplet spreading process. On the time scale the liquid droplet spreads, F_s becomes very small and λ_{LS} reaches its equilibrium [12,29,34–36]. This phenomenon explains why the liquid droplet spreading process slows with time as reflected by Tanner's law ($r\sim t^{0.1}$, $\theta^*\sim t^{-0.3}$). However, Tanner law is only applicable for liquid droplet radius smaller than l_c. As the radius of the liquid droplet increases, this assumption becomes invalid as the liquid droplet radius grows to be greater than the l_c.

Harth & Schubert [37] considered the influence of gravitational, viscous and capillary forces on the initial liquid droplet spreading process by considering a balance of forces based on the spherical cap approximation:

Complete wetting case ($\gamma_{SV} - \gamma_{SL} \geq \gamma_{LV} (\cos\theta^* \geq 1, \theta^* = 0)$)

$$r(t) = \left[\left(\gamma_{LV} \frac{96\text{\O}_L V_0^4}{\pi^2\mu}(t+t_0) \right)^{\frac{1}{2}} + \left(\frac{\text{\O}_L(t+t_0)}{\mu} \right)^{\frac{2}{3}} \frac{24\rho g V^{\frac{8}{3}}}{7 \cdot 96^{\frac{1}{3}}\pi^{\frac{4}{3}}\gamma_{LV}^{\frac{1}{3}}} \right]^{\frac{1}{6}}$$

Equation 2-24

Partial wetting case ($\gamma_{SV} = \gamma_{SL} (\cos\theta^* = 0)$)

$$r(t) = r_e \left[1 - \exp\left(-\left(\frac{2\gamma_{LV}}{r_e^{12}} + \frac{pg}{9r_e^{10}} \right) \frac{24\,\text{\O}_L V_0^4(t+t_0)}{\pi^2\mu} \right) \right]^{\frac{1}{6}}$$

Equation 2-25

where $\text{\O}_L$ is the shape factor based on spherical shape assumption , t_0 is the initial time delay of the liquid droplet horizontal spreading process when the liquid is still spherical and r_e is the equilibrium liquid droplet contact radius.

Equation 2-24 - 2-25 were derived on the basis that the liquid droplet volume on the solid surface remains constant and doesn't penetrate into the solid surface. However, in the case of "real" powder beds, the liquid droplet may penetrate to some extent during the liquid spreading process. This consideration means that the liquid droplet volume will change with time. Nevertheless, it is important to examine the implication of Harth & Schubert's model in

19

predicting the initial liquid spreading process for real powder beds, where it has not been applied. This will be examined in a later chapter section.

2.4.2 Maximum Spreading of a Liquid Droplet

In examining the liquid droplet spreading process on a powder bed, a parameter of interest in understanding the physics behind the dynamics of the liquid droplet spreading process, is the maximum horizontal spreading factor ($d_h max$). The $d_h max$ is defined as the ratio of the maximum horizontal spreading diameter (d_h) on the powder bed surface to the initial liquid droplet diameter (d_0):

$$d_h max = \frac{d_h}{d_0}$$

Equation 2-26
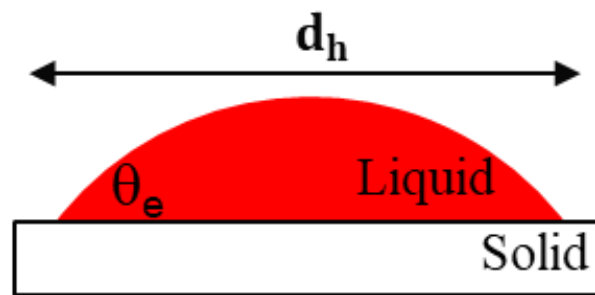
Figure 2-10. Maximum liquid droplet horizontal spreading profile on a powder bed surface.

According to Roisman et al. [38], the $d_h max$ can be described using three liquid droplet spreading scenarios. The first is at low We and Re numbers where the liquid droplet spreading process is governed by capillary and viscous forces, whilst for high We and Re numbers the process is dominated by inertia. In the second scenario when the capillary forces are dominant, $d_h max$ is reached when $t_{max} < t_{BL}$. The final scenario, the dominance of the viscous forces is represented by $t_{max} > t_{BL}$. t_{max} is defined as the time required to reach d_h and t_{BL} is defined as the time that the viscous forces play a dominate role in the liquid droplet spreading process. Roisman et al. (2004) scenarios demonstrate the reliance of $d_h max$ on viscous and surface tension forces, which has also been highlighted in several studies in literature [12,28,39–41].

Accurate prediction of $d_h max$ is of key importance in many industrial applications. For example, in the pharmaceutical industry the granule quality is dependent on the extent of liquid

spreading which is directly related to $d_h\text{max}$, where greater extent of spreading represents good wetting of the powder bed. Many authors have proposed expressions for predicting $d_h\text{max}$. These expressions are typically derived on the basis of an energy balance before and after liquid droplet impact on the powder bed [42]:

$$E_{K1} + E_{SL2} + E_{SS1} = E_{K2} + E_{SL2} + E_{Si2} + E_{V2}$$

<div align="right">**Equation 2-27**</div>

where E_K is the initial liquid droplet kinetic energy, E_{SL} surface energy of the liquid, E_{SS} is the surface energy of the solid, E_{SL2} is the liquid and solid interfacial energy and E_{V2} is the viscous dissipation energy.

Jones [43]proposed a simple model to predict $d_h\text{max}$ in order to evaluate viscous energy dissipation:

$$d_h\text{max} = \left(\frac{4}{3}\text{Re}^{\frac{1}{4}}\right)^{\frac{1}{2}}$$

<div align="right">**Equation 2-28**</div>

However, Jones' model neglects the surface tension effects which have been linked to poor agreement of predictions with experimental results [44]. In contract to Jones' model, Collings et al. [45] argued that viscous dissipation energy effects were negligible and proposed an expression based on surface tension effects:

$$d_h\text{max} = \left(\frac{\text{We}}{6}\right)^{\frac{1}{2}}$$

<div align="right">**Equation 2-29**</div>

Colling's model was derived based on the assumption that the liquid droplet takes the form of $\theta_\gamma = \pi$ when in contact with the powder bed. However, θ_γ is only applicable in equilibrium conditions when the liquid droplet has come to rest on an ideal, smooth and chemically homogenous powder bed, whilst $d_h\text{max}$ is a complicated function of the contact line speed.

Chandra & Avedisian [46] recognised the importance of both viscous dissipation and surface tension effects in predicting $d_h\text{max}$ and proposed the following expression:

$$\frac{\frac{9}{2}d_h max^4}{Re} + \frac{3\big((1-\cos\theta^*)d_h max^2 - 4\big)}{We} = 1$$

The results predicted using Chandra & Avedisian's model were found to deviate by 20.60 % of the experimental results [47,48]. This discrepancy is attributed to the model not taking into account the contribution of viscous dissipation accurately. Further expressions of $d_h max$ have been proposed in an attempt to accurately include viscous dissipation and surface tension effects, these are summarized in Table 2-1.

Table 2-1. Summary of the proposed existing models for $d_h max$

Model	Reference
$\dfrac{3d_h max^2}{We} + \dfrac{1}{Re}\left(\dfrac{d_h max}{1.2941}\right)^5 = 1$	Madejski (1976) [49]
$d_h max = \sqrt{\dfrac{We + 12}{3(1-\cos\theta^*) + 4(\frac{We}{\sqrt{Re}})}}$	Pasandideh.Fard et al. (1996) [50]
$\left(0.2Oh^{0.33}We^{0.665} + \dfrac{1}{4}(1-\cos\theta^*)\right)d_h max^2 + \dfrac{2}{3}d_h max^{-1} = \dfrac{We}{12} + 1$	Mao et al. (1997) [40]
$(We + 12)d_h max = 8 + d_h max^3\left(3(1-\cos\theta^*) + 4\dfrac{We}{\sqrt{Re}}\right)$	Ukiwe & Kwok (2005) [51]
$(We + 12)d_h max = 8 + d_h max^3\left(3(1-\cos\theta^*) + 4\dfrac{We}{\sqrt{Re}}\right)$	Vadillo et al. (2009) [52]

However, these models still exhibit large discrepancies when predictions are compared to experimental data due to their reliance on specific empirical fitting parameters or correction factor [48]. Thus, complications involved in deriving models to predict $d_h max$ remain largely unresolved and the physical properties of the powder bed surface i.e. porosity, roughness, pore

structure, chemical heterogeneities and liquid i.e. viscosity, surface tension that affect $d_h max$ are not well accounted for in existing models proposed in literature.

2.5 Nucleation Thermodynamics: Nucleation Formation

According to Waldie et al. [53], one liquid droplet tends to form one nuclei i.e. primary granule using the expression:

$$d_{nuclei} \propto d_0^B$$

Equation 2-31

where d_{nuclei} is the resultant nuclei diameter and B is the experimental correlation coefficient.

However, two or more liquid droplets can coalescence leading to the formation of larger nuclei. This relation is expressed as [54]:

$$\frac{\pi}{6} d^3_{nuclei} = K \frac{\pi}{6} d_0^3 N_d$$

Equation 2-32

$$K = \frac{1}{S_w \varepsilon}$$

Equation 2-33

where N_d is the number of liquid droplets, K is the nucleation ratio, S_w is the wetting saturation and ε is the powder bed porosity.

Schaefer & Mathiesen [55] proposed two nucleation formation mechanisms based on the relative size of the primary powder particles to that of the liquid droplet size, assuming that the thermodynamics of wetting are favourable. The first immersion, occurs when the liquid droplet size is larger than the primary powder particle size and produces nuclei with saturated pores. The second distribution, occurs when the liquid droplets are smaller than the primary powder particle size. This results in the liquid coating the surface of the primary powder particles and producing nuclei which may have air trapped inside.

However, the liquid binder does not always spread on the powder bed which results in λ being negative. The immersion-distribution hypothesis also does not consider the possibility of solid spreading over a liquid droplet (λ_{SL}) which has been reported in many experimental observations [56–58]. Figure 2-11 summarizes all the possible scenarios of the immersion-distribution hypothesis which have been extended to wet granulation. However, nuclei morphologies and properties of the final granules produced from each mechanism differ dependent on the primary powder formulation and process conditions used.
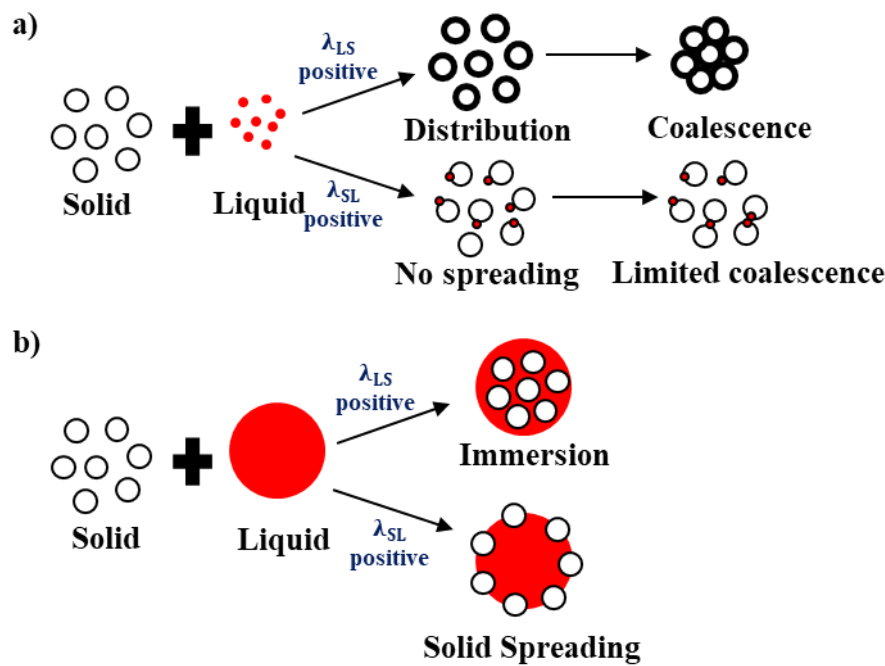
Figure 2-11. Nuclei formation mechanisms: (a) liquid droplets are smaller than the solid particles (b) liquid droplet size is larger than the primary powder particles.

The immersion nucleation mechanism is of particular interest in this thesis as it represents typical liquid droplet and primary powder bed particle model systems used in the pharmaceutical industry. There are two key theories of immersion nucleation which have been proposed in literature [59,60]. The first is the immersion nucleation theory proposed by Hapgood et al. [60], where the imbibition of a liquid droplet into a powder bed is modelled as a bundle of cylindrical particles. The second was proposed by Hounslow et al. [59] where particles are immersed into the liquid droplet and form a critical packing fraction inside a nucleus. These theories are discussed in the following sections in more detail.

2.5.1 Nucleation by Liquid Droplet Imbibition

When a liquid droplet contacts the powder bed, the time required for complete imbibition of the liquid droplet into the powder bed is referred to as the liquid droplet imbibition time (t_{dp}). Liquid droplet imbibition time is typically used as an indication for the nuclei formation kinetics i.e. fast imbibition times demonstrate that the thermodynamics of wetting are favourable.
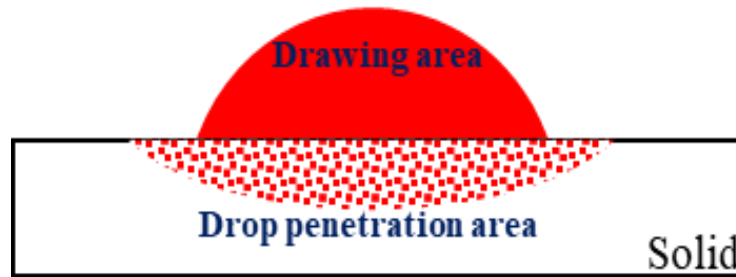
Figure 2-12. Liquid droplet penetration on a powder bed.

Denesuk et al. [61] first related the t_{dp} to the three-phase contact line behaviour of the γ_{SL} interfaces using two limiting cases. (see Figure 2-12). The first limiting case is the constant drawing area (t_{CDA}) case, which assumes that the contact radius of the γ_{SL} interface remains stationary and the θ^* decreases as the imbibition of the liquid droplet is proceeding. The t_{CDA} case represents the fastest possible time as the t_{CDA} case ensures that a maximum number of pores are available or liquid droplet imbibition.

However, in the second case the decreasing drawing area (t_{DDA}) assumes that the θ^* is pinned at a constant position and the contact radius of the γ_{SL} interface decreases as the liquid droplet imbibition process is proceeding. The t_{DDA} is representative of higher t as the number of available pores decreases with decrease in the drawing area.

The process for liquid droplet imbibition into a powder bed is driven by capillary pressure and resisted by viscous forces using the Washburn equation [62] :

$$l = \sqrt{\left(\frac{R_{pore}\gamma_{LV}\cos\theta^*}{2\mu}\right)t}$$

<div align="right">

Equation 2-34

</div>

where l is the liquid droplet imbibition distance and R_{pore} is the capillary pore radius.

Theories for liquid droplet imbibition into the powder bed apply the Washburn equation to develop expressions to predict the t_{dp} [60–62]:

$$t_{CDA} = 1.35 \frac{V_0^{\frac{2}{3}}}{\varepsilon_{eff}^2 R_{eff}} \frac{\mu}{\gamma_{LV} \cos \theta^*}$$

<div align="right">**Equation 2-35**</div>

$$t_{DDA} = 9\tau_{CDA}$$

<div align="right">**Equation 2-36**</div>

$$R_{eff} = \frac{\emptyset_p d_{3,2}}{3} \frac{\varepsilon_{eff}}{1 - \varepsilon_{eff}}$$

<div align="right">**Equation 2-37**</div>

where ε_{eff} is the effective porosity, R_{eff} is the effective pore radius, $\emptyset_p$ is the shape factor of the primary particle size and $d_{3,2}$ is the sauter mean diameter.

The key assumptions used to derive Equation 2-35 – 2-37 are:

i.   The primary particles are spherical in shape.

ii.   The powder bed has an irregular pore structure.

iii. The powder bed macrovoids do not participate in the liquid droplet imbibition process.

iv.   The liquid droplet doesn't spread on the powder bed surface and the maximum contact radius of the γ_{SL} interface is equal to the initial liquid droplet radius.

Validation for the t_{dp} theory has been presented experimentally by a few authors [60,63,64]. Inconsistencies between experimental data and theoretical predictions have been reported. Oostveen et al. (2015) observed that d_h exceeds d_0 i.e. on a powder bed the liquid droplet spreads to a greater extent compared to its initial radius, without providing an explanation [64]. This means that the assumption that the contact radius of the γ_{SL} interface is equal to the radius of the initial liquid droplet is misleading in the t_{dp} theory. To enable the development of effective predictive models for t_{dp}, thorough understanding of the controlling parameters that influence t_{dp} is crucial.

Another important consideration in the liquid droplet imbibition process is the rate of imbibition into the powder bed. The rate of imbibition into a powder bed is described using Darcy's Law which accounts for one-dimensional (1D) liquid flow along a Laplace capillary pressure gradient [31,32,65]:

$$v_D = \frac{k}{\mu} \frac{2\gamma_{LV} \cos \theta^*}{R_{pore} h}$$

where v_D is the Darcy rate of imbibition, k is the permeability, z is the distance travelled by the liquid.

However, the liquid droplet imbibition process is a three-dimensional process (3D) of which the Darcy relation does not account for. By considering the contact area of the γ_{SL} interface at a specific time, v_D can be related to the 3D imbibition rate via [32]:

$$v_D = \frac{V_o - V_t}{d^2 t}$$

where V_o is the initial drop volume and V_t and d are the volume and diameter respectively of the drop remaining on the surface at a specific time.

Substitution of normalised spreading and imbibition rate i.e. $\frac{d}{d_0}$ and $\frac{V_o - V_t}{V_o}$ into Equation 2-39 yields an adimensional imbibition rate ($\bar{v}_D$):

$$\bar{v}_D = \frac{\left(\dfrac{V_o - V_t}{V_0}\right)}{\left(\dfrac{d}{d_0}\right)^2 t}$$

In essence $\bar{v}_D$, Equation 2-40 assumes that the d_v imbibition mechanism is time dependent on the liquid droplet volume height (h) remaining on the powder bed. This relation is expressed as:

Based on Equation 2-38, let,

$$C = \frac{k}{\mu} \frac{2\gamma_{LV}\cos\theta^*}{R_{pore}h}$$

Then Equation 2-38 becomes:

$$v_D = \frac{C}{h}$$

The rate of change for h will be:

$$\frac{dh}{dt} = \frac{C}{h}$$

Equation 2-43 is solved analytically to yield a modified Darcy rate law [31]:

$$h \times dh = C \times dt$$

$$\int_0^h h \cdot dh = C \cdot \int_0^t dt$$

$$\frac{h^2}{2} = Ct$$

$$h \propto t^{0.5}$$

The approach used to derive Equation 2-40 describes a case slightly more realistically for liquid droplet imbibition into powder beds. However, experimental validation of the theory has not yet been done. Applicability of the liquid imbibition rate theory is one of the major objectives of this thesis.

In reality, the liquid droplet imbibition behaviour is expected to be between the two limiting cases t_{CDA} and t_{DDA} as when the liquid droplet contacts the powder bed, the liquid droplet can proceed simultaneously in two directions: (i) increase in the liquid droplet base (radius) until the d_h max spreading is reached and (ii) decrease in the drop base (radius) as a result of vertical liquid droplet imbibition (d_v) into the powder bed to form nuclei [66]. These two phenomenon are classified as two competing spreading and imbibition mechanism of a liquid droplet [65–68] .

The liquid droplet spreading and imbibition process has been extensively investigated as a single phenomenon in a number of studies. However, there has been little published work on the competing d_h spreading versus d_v imbibition liquid droplet mechanisms. This work includes the studies carried out by Clarke et al. [65], where it was reported that on porous paper, an inkjet liquid droplet will initially spread to reach its d_h max spreading before it begins to recede vertically into the powder bed. In contrast, Holman et al. [68] found that the competing liquid droplet mechanisms of a inkjet liquid droplet occur on similar time scales, precluding their treatment as separate phenomena. Haidara et al. [31] investigated the competing liquid droplet mechanisms of silicon oil drops of varying viscosities on nanoporous membranes and found that the d_h spreading rate had a greater dependency on changes in viscosity in comparison to the liquid droplet imbibition process [31].

Grzelakowski et al. [32] investigated the influence of the nanoporous membrane pore structure on the competing liquid droplet mechanisms. Although it was expected that the small interconnected pores would enhance liquid flow via lateral transport, the imbibition rate was found to be higher for larger straight pores. The small interconnected pores slow down the imbibition process whilst promoting the d_h max spreading rate. These studies have provided meaningful insight into the competing liquid spreading and imbibition mechanisms. However, they have been limited to inkjet-printing and nanotechnology applications in which the structure of the substrate i.e. solid surface does not change during the liquid droplet spreading and imbibition process.

In the pharmaceutical industry, the competing spreading and imbibition mechanisms of a liquid droplet on a powder bed is of fundamental importance because the extent of spreading influences the granulation behaviour and the resultant granule attributes. The powder beds have complex structures which contain macrovoids and consists of irregular shaped particles that are randomly packed, which have been reported to significantly influence the liquid droplet

spreading behaviour [33,60,69]. It was reported that on dry and pre-wetted porous powder beds, the d_v imbibition rate into the powder bed has a greater degree of dependence on changes in viscosity at low impact velocity compared to the d_h spreading [33]. This means that more viscous binders will spread comparably further on the powder bed surface but require a smaller reduction in the 'remaining drop' volume for capillary induced suction to pin the contact line.

Most notable is that when the liquid droplet contacts the powder bed its structure changes due to the formation of liquid bridges as the primary powder particles i.e. soluble particles undergoes partial dissolution. The partial dissolution increases the 'effective µ' of the liquid which strengths the liquid bridge, resulting in the formation of nuclei. However, there has been no experimental evidence on the existence of the competing liquid spreading and imbibition mechanisms of single droplet impacting hydrophobic powder beds. Further understanding is required due to new classes of active ingredients used in the pharmaceutical industry being poorly wetting [3]. In this thesis, studies on competing liquid droplet spreading and imbibition mechanisms have been extended to focus on the influence of powder bed wettability which remains a critical experimental issue in the pharmaceutical field to enable effective design of the granulation process.

2.5.2   Nucleation by Immersion

Hounslow et al. [59] proposed two theories to describe primary particles being immersed into a liquid droplet to form nuclei. Both models assume that with time, the solid particles form a critical packing fraction (ϕ_{cp}) which corresponds to a capillary state of the liquid droplet inside the nuclei:

$$\phi_{cp} = \frac{V_0}{V_0 + V_S}$$

<div align="right">**Equation 2-48**</div>

where V_S is the volume of the solid particles.

The first model is the surface tension driven flow which assumes that nucleation by immersion is driven by capillary forces and resisted by viscous forces using the expression for a spherical geometry:

$$\frac{V - V_0}{V_{max} - V_0} = \sqrt{\frac{\gamma_{LV}}{18.75\mu d_0^2}\frac{1 - \phi_{cp}^{\frac{1}{3}}}{\phi_{cp}^3}t} = \sqrt{\frac{t}{t_{max}}}$$

where V_{max} maximum liquid droplet volume related to ϕ_{cp}.

The model shows that the growth of the nuclei increases with the square root of time were a maximum growth is reached at a specific time t_{max} at which no further growth occurs. Hounslow et al. [59] model simply relates V and ϕ_{cp} which is dependent on the physical properties of the liquid binder and the primary powder particles. However, the authors didn't provide a quantitative expression of which ϕ_{cp} can be calculated from physical properties of the liquid binder and primary powder particles. A major limitation of this model is that its assumption that ϕ_{cp} is uniform, neglecting the fact that the nuclei will experience consolidation and deformation inside the granulator. To account for the collisions that the nuclei will experience inside the granulator, Hounslow et al. [59] proposed a deformation driven diffusive flow model. This model assumes that due to the collisions inside the granulator, there is continuous transportation of liquid in and out of the nuclei:

$$\frac{V - V_0}{V_{max} - V_0} = 1 - \exp\left(-\frac{12D_{eff}\phi_{cp}^{\frac{2}{3}}}{d_0^2}t\right)$$

where D_{eff} is the effective diffusivity.

Similar to the first model, a maximum growth for the nuclei volume is reached, however nuclei growth should decrease exponentially with time. In practise, the deformation driven diffusive flow model describes a case which is more realistic for real immersion mechanisms taking place inside a granulator. However, no expression to calculate D_{eff} was provided to allow for its application and the dependence of the primary powder size and viscous forces was not accounted for. Perhaps what is of interest is the fact that both models do not take into account the presence of air in the nuclei on which ϕ_{cp} might be dependent. In general, Hounslow et al. [59] model uses well understood physics and its incorporation of nuclei

31

kinetics and growth allows for the 'real' picture of immersion nucleation taking place inside a granulator to be captured in theory.

2.6 Nucleation Thermodynamics: Formation of Liquid and Solid bridges

In wet granulation the ability of primary powder particles to bond with each other to form granules is controlled by the forces acting on the particles. The most fundamental forces governing the ability of particles to bond with each other are the attractive forces i.e. adhesive, cohesive and the environmental forces i.e. gravity, inertia [70]. It is the ratio between these forces that define the acting binding mechanisms (attachment forces).

The binding mechanisms in wet granulation were first described by Rumpf [71] and are divided into five sections:

Table 2-2. Binding Mechanisms

---

1. **Adhesion and cohesion forces in non-freely movable binders** e.g. viscous binders.

2. **Interfacial forces and capillary pressure at freely movable liquid surfaces** e.g. liquid bridges.

3. **Solid bridges** formed via drying, crystallisation etc.

4. **Attraction forces between solid particles** e.g. van der Waals' forces, electrostatic forces etc.

When applied to wet granulation, the binding mechanisms that need to be considered are the formation of liquid and solid bridges. In the initial wetting and nucleation stage, the liquid droplet when in contact with the powder bed surface forms mobile liquid bridges which can exist in a number of different states depending on the degree of saturation between particles

[2]. Figure 2-13 illustrates the different liquid saturation states: pendular, funicular, capillary, droplet and pseudo droplet.
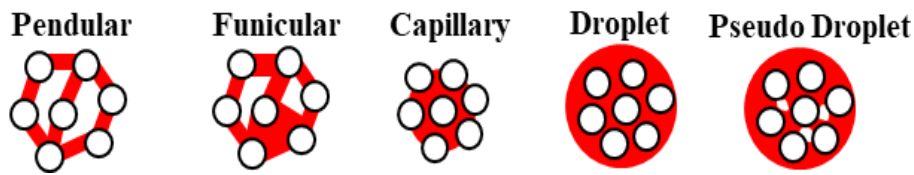
Figure 2-13. Different granule states based on liquid saturation.

The primary powder particles are held together by the liquid bridges at the point of surface contact between the particles, (see Figure 2-13). This is termed the pendular state where the liquid bridges exist at low liquid saturation state. As the liquid saturation increases, the particles will rearrange themselves into a continuous liquid-solid network, resulting in a funicular state. When all the air has been completely filled with the liquid binder, a capillary state is reached. The capillary forces will act to pull the particles closer together to form wet nuclei. However, the presence of viscous forces can cause the liquid bridges to resist rearrangement. Further saturation of a pseudo droplet state, where the unfilled voids remain trapped inside the liquid droplet is also possible, this phenomenon is likely to occur in poorly wetting powder systems.

The liquid saturation i.e. wetting state (S_w) of each state is calculated as [54]:

$$S_w = \frac{\phi_L}{\phi_S + \phi_L + \phi_V}$$

Equation 2-51

where ϕ is the volume fraction and the subscripts L, S, V represent liquid, solid and macrovoid.

The formation of liquid bridges is temporary intermediate stage in wet granulation. Permanent solid bridges between the particles is achieved by either drying or melting or crystallisation etc. There are other attractive forces that operate between the particles without the presence of solid bridges e.g. electrostatic forces, van der waals forces, chemical bonding. When the primary powder particles are irregularly shaped, mechanical interlocking of particles may occur. Mechanical interlocking is one of the key aspects that have been shown to have an impact on the final product characteristics such as table hardness, friability and dissolution.

2.7 Granulation: Twin Screw

Traditionally, in the pharmaceutical industry the granulation process has been mostly conducted in batch mode. Although this technique is well established and is commonly used in the pharmaceutical industry. The major downside to the batch process is that the equipment must be stopped for cleaning and reconfiguration between batches and that the quality of the product needs to be assessed before proceeding to the next stage to ensure that all product specifications are met. Thus, by operating in batch mode, the intra- and inter-reliability of the output is compromised by having so many steps.

Twin screw granulation (TSG) based on extrusion technology, has been considered as a much better alternative to the current batch mode granulation [5]. The main advantage of this process is that it can be run continuously for longer periods, has high flexibility and reproducibility [72]. In recent years, the pharmaceutical industry has been making efforts to transition from batch to continuous processing in order to improve production efficiency and enhance quality assurance. However, the adoption of continuous granulation has faced many obstacles due to the complex TSG machinery attributes not being well understood. Given the developing interest in continuous TSG in the pharmaceutical industry, this thesis seeks to further TSG process understanding and development in relation to granulation of hydrophobic powder which has received little attention in literature.

2.8 Twins Screw: Design

The TSG profile is shown in Figure 2-14. As can be seen, the TSG consists of (i) feeding ports for the liquid binder and primary powder (ii) two parallel screws which are coupled with a motor and enclosed in a barrel which is normally connected to a cooling jacket. The TSG is a regime separated process with the granulation mechanisms occurring one after another along the barrel [5]. It works by supplying the primary powder and liquid binder at the start of the barrel inlet. These materials are then conveyed along the screw length where they experience applied stress required to distribute the liquid binder and compact the materials to form granules which are discharged at the exit of the granulator.
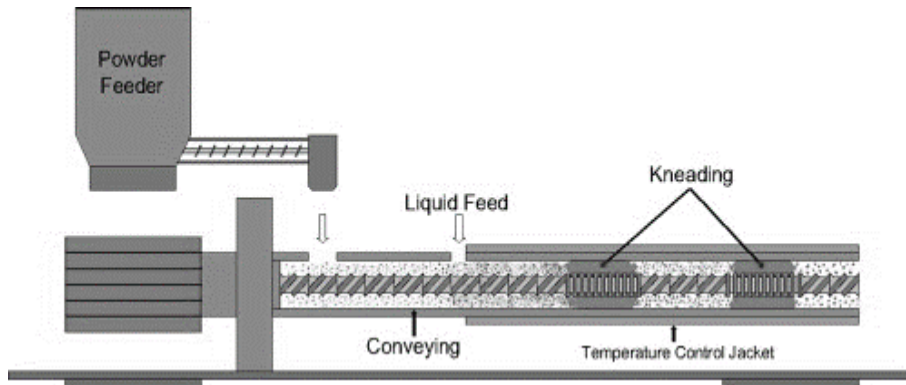
Figure 2-14. TSG design profile.

2.9 Twin Screw: Principle Components

The main geometry of the TSG consists of screws built up modularly (see Figures 2-14 and 2-15). These are ordered as either counter. or co-rotating screws and differ in the way the material flows inside the barrel. In the pharmaceutical industry, the co-rotating screws are commonly used. This is due to their innate ability to be self-cleaning which minimizes material build-up and contamination, thus allowing the process to run for longer periods [73].
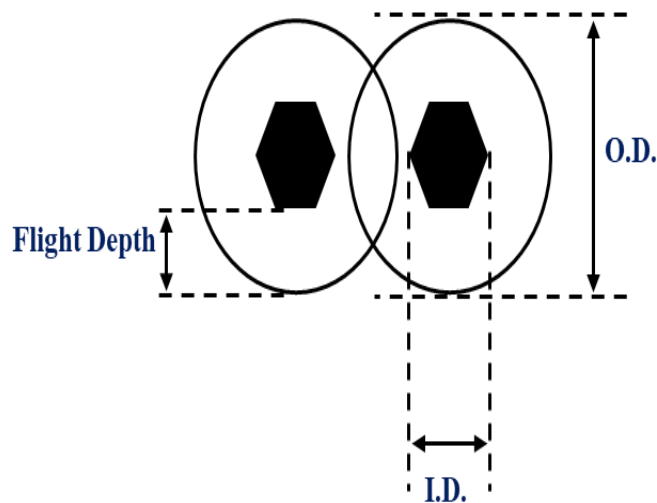
Figure 2-15. TSG screw profile.

The internal geometry of the TSG is distinguished by the ratio of the outer and inner diameter of the screws represented as O.D and I.D respectively. These parameters determine the screw flight depth and free volume available inside the barrel channel for materials, (see Figure 2.15). However, the external geometry of the TSG is distinguished by the axial length to diameter ratio of the screws which is typically expressed as L/D ratio.

Pharmaceutical operations typically use TSG's with L/D ratio ≤ 40. However, other industries e.g. polymer industry rely on twin screw extruder operations with greater L/D values which indicate longer processing section. This variability in the dimensions of the TSG design does not provide a good basis for scale up. Therefore, process optimization methods typically rely on the 'actual' geometry of the TSG.

TSG is favoured due to its flexibility and modularity of its screw configuration which is useful in manipulating targeted granular product attributes e.g. size, shape, strength and porosity etc. [5]. There are a variety of screw elements which are applicable to TSG: conveying elements (CE's), kneading elements (KE's) and mixing elements (ME's), (see Table 2-3). These differ in L/D, geometry, design and available free volume, however they typically have the same cross-sectional area as they share the same screw profile [74,75].

Table 2-3. TSG screw element type

Key	Length (diameters)	Element diagram	Ability
Feed screw (conveying element)	1D		Conveying ability (more plug flow-like)
Distributive conveying element (cut conveying element)	1D		
Kneading Element (60˚ forward)	1/4D		Minimal conveying ability (more continuous stirred tank.-like)
Distributive mixing element (narrow distributive mixing element)	1/4D		

CE's exert minimal stress and principally work by transporting material downstream [76–78]. However, the conveying properties of the CE's decrease with a reduction in the flight pitch since less volume is offered for the material. Thus, less material is conveyed with each screw revolution [77,79,80]. This decrease in conveying capacity of the CE's does not necessary mean that adequate mixing is achievable. Therefore, further research is required to establish if or whether adequate mixing can be achieved with CE's when the flight pitch is reduced.

The operating principle of the KE's is primarily determined by its staggering angle, width and length 'number' and are typically used to increase the degree of mixing of material. The greater staggering angle of 90˚ between the KE disc's was found to increase granulation with less fines (un-granulated material) produced in comparison to the 30˚ and 60˚, as the cross-sectional (radial) mixing effect was increased [80]. This increased mixing effect comes at the cost of decreased conveying capacity of the screw, hindering granular flow [81]. As a result, in order to maintain a constant flow rate inside the TSG barrel channel, more stress is required to push the granules through the 90˚ KE's.

A short KE width and length have more of a distributive effect, resulting in the materials being homogeneously distributed in the barrel channel through fragmentation of large granules from the CE zone [76]. However, the probability of material being forced into the KE disc-disc and KE disc-barrel wall gap increases as the width and length of the KE's increases [76,78,82,83]. With a longer KE width and length, the distribution of the materials is enhanced, promoting more consolidation and densification [78]. However, a longer KE width and length can cause excessive granule deformation due to increased stress acting on the material inside the TSG barrel which may increase the torque above its performance limit. This means that there is a compromise between the TSG process and experimental design constraint's which must be carefully considered during process optimization when using TSG.

In TSG, limited studies have been carried out to investigate the influence of different forms and geometries of mixing elements (ME's) on the TSG mixing performance. Unlike KE's, ME's operate in an 'almost completely' filled state which guarantees material backflow, promoting the material to spend a longer time in the barrel being fragmented, folded, stretched and consolidated [73]. Tooth mixing elements (TME's) were found to produce larger sized agglomerates through intensive mixing and homogenization [80,84,85]. However, continuous breakage and attrition exerted by these elements resulted in a higher fraction of fines for the batches produced using the TME's than those produced by the KE's [80,84]. Whilst, TSG granulation has primarily focused on easily wettable formulations, research is required to understand how adequate mixing in TSG can be achieved using various screw elements when using poorly wetting formulations.

2.10 Twin Screw: Mixing

Mixing is defined as the distribution of materials (solid, liquid) which differ in one or more physical and/ or mechanical properties in a given volume [86]. In TSG, mixing is intended to accelerate the exchange of the mass of a liquid binder and primary powder particles inside the barrel. This is to ensure homogeneous distribution of the desired granule properties i.e. chemical composition, moisture content etc. and prevent segregation of components.

There are two types of mixing behaviours which are realised in TSG by using different screw elements: distributive and dispersive mixing [87]. In distributive mixing the liquid binder and the primary powder particles are repeatedly divided, rearranged and recombined inside the TSG barrel to achieve homogeneous granules without altering the particle size. By contrast, in dispersive mixing the liquid binder and primary powder particles are agglomerated to form granules which undergo extensive shearing and elongation in the TSG. This typically leads to a reduction in particle size of the final granules.

However, TSG mixing behaviour is not only based on the interaction between the primary powder particles and the liquid binder. The mixing behaviour is also correlated to the direction in which the powder flows inside the TSG barrel, which significantly affects the resultant granule attributes (homogeneity, size, strength, shape).

The mixing behaviour based on flow direction in TSG can either be axial, referring to flow along the barrel length and/or cross-sectional which refers to flow across the barrel width [73,87]. Ideally, a combination of distributive, dispersive, axial and cross-sectional mixing is required [73]. Having a sufficient combination of the characteristic mixing behaviours can lead to superior quality of mixing. This results in improved granule uniformity in size and particle distribution, a critical quality that must be achieved.

Characterisation of the mixing quality in TSG is an important step in understanding and improving the process. In literature, residence time (RT) characteristics have been universally used to characterise the mixing behaviour in TSG [85,88–90]. However, there is no precisely defined residence time in TSG, rather there exist a residence time distribution (RTD) which depends on various parameters e.g. primary powder and liquid binder properties and TSG process parameters i.e. screw speed, powder feed rate, liquid to solid ratio (L/S), screw element

geometry and barrel fill level. The RTD is used to describe how the material flows through the TSG barrel channel.

RTD is directly correlated to axial mixing in TSG, wnere axial mixing is required in order to compensate for variations in primary powder and liquid binder feed rate [73,86]. However, it is possible to achieve uniform distribution in TSG with good cross mixing if a constant material feed rate is achieved. If variations in material feed rate occur with minimal axial mixing, in-homogeneities in the final granular product will be observed [90].

The RTD is commonly measured using a stimulus response test where tracer concentration is measured at the exit of the TSG, to give the RTD profile shown in Figure 2-16.
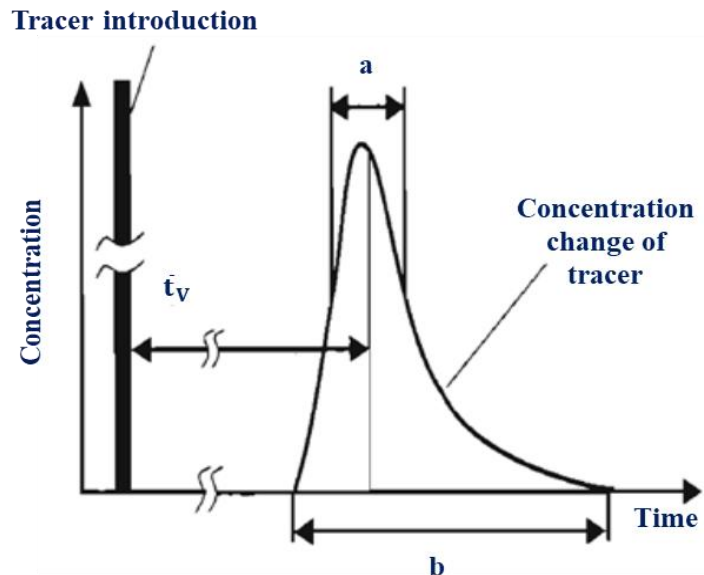
Figure 2-16. An example of RTD profile in TSG.

The $\bar{t}_V$ is the average RT calculated from the volumetric flow rate ($\dot{V}$) which represents the average time the material spends inside the TSG. The distance between the inflection points a and b represents TSG axial mixing and its self-cleaning ability, thus extent of forward and backward mixing of the screw elements [86].

In theory, the $\bar{t}_V$ can simply be expressed as:

$$\bar{t}_V = \frac{\varphi_{TSG} V_{free}}{\dot{V}}$$

where φ_{TSG} is the degree of fill, V_{free} is the free volume and $\dot{V}$ is the volumetric flow rate inside the TSG barrel.

In TSG, screw elements can operate in both partially and completely filled states depending on the material properties and process conditions used, the $\bar{t}_V$ of the states can be defined. For a partially filled screw, the degree of fill $\bar{t}_V$ is defined as:

$$\varphi_{TSG} = \frac{\dot{V}}{\dot{V}_{max}}$$

$\dot{V}_{max}$ is the maximum volumetric flow given as:

$$\dot{V}_{max} = A_1 n D_L^3$$

where A_1 is the maximum throughput, n is the screw speed and D_L is the barrel length.

Substitution gives $\bar{t}_V$ for a partially filled screw as:

$$\bar{t}_V = \frac{\dot{V}}{\dot{V}_{max}} = \frac{V_{free}}{A_1 n D_L^3}$$

However, for a completely filled screw:

$$\bar{t}_V = \frac{V_{free}}{\dot{V}}$$

<div align="right">**Equation 2-56**</div>

Equations 2-53 and 2-55 generally describe the $\bar{t}_V$ as being inversely proportional to the screw speed and material flow rate. However, in TSG the $\dot{V}$ will vary along the barrel length due to changes in bulk density of the primary powder when stress is applied. This factor makes $\dot{V}$ difficult to measure in practise. However, if the expression for $\dot{V}$ can be rewritten in terms of mass, this would allow for direct comparison with TSG experiments.

2.11 Twin Screw: Fill Level

In TSG, the fill level is an essential factor that determines the final granule properties [5]. It relies on several factors such as the screw speed, screw element geometry, powder feed-rate and barrel length. Higher fill levels lead to high compaction and densification of the primary powder which directly affects the RTD and the resultant granule properties. There are many experimental studies which detail the effect of the fill level on the resultant granule properties [81,91–93], however quantitative understanding of the fill level in TSG is still a developing area.

An attempt to predict the fill level was described by Osorio et al. [94]. They consider that the flow of powder in the TSG is related to the powder feed rate and the theoretical screw geometry using the expression for powder flow number (PFN):

$$PFN = \frac{\dot{m}_p}{\rho_S \omega D_L^3}$$

<div align="right">**Equation 2-57**</div>

where PFN is the powder flow number, $\dot{m}_p$ is the mass flow rate of the powder, ρ_S is the bulk density of the powder and ω is the angular velocity of the shaft.

However, Equation 2-52 doesn't accommodate the effect of the various TSG elements on the fill level. Osorio et al. [94] recognised this implication and corrections of the screw geometry were proposed by assuming that the PFN is proportional to the ratio of how quickly the powder is feed into TSG barrel to the screw turnover volume using:

$$\varphi_{Osorio} = \frac{1}{\dfrac{A_e 2\pi v_p}{D_L^3 \omega}} PFN$$

where A_e is the free cross-sectional area of the element and v_p is the net forward velocity of the powder.

At high φ_{Osorio} the screws will be operating at their full capacity (flooded state) and at low φ_{Osorio} the screws will be operating at low capacity (starved state). Theoretically, the φ_{Osorio} has a maximum value of 1 when the screw is operating in a flooded state and the TSG is operating at its maximum throughput for a given speed.

In practise, the flooding state is observed when $\varphi_{Osorio} < 1$ which is likely to be due to slippage of powder on the screws, the resistance of flow caused by the non-conveying elements and the actual bulk density differing form the 'real' bulk density of powder measured offline. However, the expression for φ_{Osorio} represents a complex relation between the powder feed rate and the screw geometry relying on estimation of parameters i.e. v_p which makes it difficult to be applied in TSG fill level process characterisation [94]. Thus, estimation of the parameters doesn't describe the case more realistically for the TSG process.

According to Gorringe et al. [95], the fill level of a screw elements is related to the ratio of the powder feed rate to the theoretical maximum capacity of the screw required to convey powder using the expression:

$$\varphi_{Gorringe} = \frac{\dot{m}_p}{n_v \rho_S \left(V_{Free} \dfrac{S_L}{D_L}\right) n}$$

where η_v is the volumetric efficiency of the screw to convey powder, V_{Free} conveyer free volume and S_L screw lead length.

In essence, both Equation 2-58 and 2-59 compare the TSG volumetric flowrate to the forward volumetric conveying rate of the screws when they advance in the axial direction. However, $\varphi_{Gorringe}$ considers the capacity of the screw element which provides a more

practical measure of fill level in TSG. A major drawback with the theoretical approaches used to determine the fill level is that the published experimental verification of the models is insufficient and their applicability to various screw geometries is limited. These drawbacks make it difficult to scale up the TSG process.

A parameter that could be used to describe the fill level in TSG is the specific mechanical energy (SME), however it has received less attention in literature [5]. The SME is a measure of energy input dissipated as heat inside the TSG barrel per unit mass:

$$\text{SME} = \frac{T \times n}{\dot{m}_p}$$

<div align="right">**Equation 2-60**</div>

where T is the motor torque.

The T can be monitored in a production line scenario to understand the process signature which can form part of the TSG control strategy. For any given powder feed-rate the torque will go from a maximum value when the barrel channel is in a flooded state to a minimum value where it is in a starved state as the screw speed is increased. If translating the torque into SME collapses all the individual curves into a single curve for a given combination of materials and process conditions, then it is likely that first principles correlation can be derived which relates the fill level to SME. The correlation developed can feed into the TSG scale up strategy as torque can be mapped on the smallest scale and predict performance for any scale. However, this remains a new area to be explored.

2.12 Twin Screw: Hydrophobic Powders

In the pharmaceutical industry, the granulation of hydrophobic components is challenging as the preferential wetting and de-mixing problems which occur when using these have a significant effect on the final granular properties [96]. Surfactants have been commonly used during the granulation process to improve the wetting characteristics of hydrophobic powders. However, this is not always practical due to the reduction in economical operation or the chemical interactions that may occur as a result of the limited understanding behind their science in granulation [3]. Other techniques have also been utilized to increase the powder wettability. These include but are not limited to nano-sized powder components, hydrotrophy, use of precipitation inhibitors, alteration of pH, solvent deposition, super critical fluid

43

techniques and solid dispersion [97]. However, these techniques have not been used as a component in manufacturing of pharmaceutical products due to their complexity and cost.

A number of papers have investigated the powder wetting behaviour observed when using a hydrophobic component in the formulation in a high shear mixer, a batch technique [63,98–100]. Main observations include the formation of liquid marbles when small hydrophobic particles spread over the surface of a liquid drop. The liquid marble formation approach has been applied in designing hollow granules for industrial applications however; the resultant granular products contain a porous intermolecular structure which compromises the granular strength. This has serious implications not only for storage and handling but also for the range of applications for which these products can be used i.e. tableting, capsule filling, bottle filling or blister strip filling.

Currently, in TSG there are limited studies on the granulation of formulation containing a hydrophobic component. Recently, Yu et al. [101] evaluated the influence of hydrophobicity on the resultant granule properties in TSG. In their work, the formulation hydrophobicity resulted in preferential wetting of the hydrophilic component and liquid binder heterogeneity in the granules This finding was ascribed to be due to the liquid binder drop-wise method used, which significantly increases the sensitivity of the TSG when using hydrophobic formulations [102]. However, Yu et al. [101] found that the stress applied by the kneading elements significantly improved the distribution of the liquid and formulation components.

Li et al. [96] proposed that using a foam binding agent improved granule homogeneity along the TSG barrel due to the high spread to soak ratio of the foam binder that cages the hydrophobic particles within the mass of the local hydrophilic solid. This means that the granules will either grow by consolidation or coalescence in this case compared to the layering mechanism detailed by Yu et al. [101] which was observed to cause liquid binder distribution heterogeneity in granules. Granule growth via gel bridge mechanism was observed when a hydrophobic component was included in a formulation composition containing a higher molecular weight polymer, hydroxypropyl methylcellulose in solid form at 30˚C [103]. This mechanism was ascribed to be due to the low water sorption of the hydrophobic component which increases the liquid binder content available to thicken the gel layer of the polymer. However, at higher temperatures the decrease in water sorption of all components resulted in the hydrophobic component weakening the strength of the liquid bridge.

Similar conclusions to those of Li et al. [96] and Li et al. [103] were reported with distributive mixing elements Saying et al. [104] and with liquid binder injection after passage through the kneading block El Hagrasy et al. [78,105]. However, these investigations only considered easily (immediate) wetting formulations in which the granulation behaviour can be easily controlled. From these publications, it can be concluded that the mixing time of the TSG process is too short to reach sufficient homogeneity without relying on using mechanical dispersion, foam or viscous liquid binder.

Despite progressive research in TSG in the past decade, notable limitations in the understanding of this technique currently exist particularly with regards to the effect of formulation hydrophobicity and its interplay with process parameters. These have not been investigated in sufficient detail to enable effective formulation development and adequate process design for product optimization without compromising other steps of the overall granulation process.

2.13 Thesis Comments

In the literature review section, the current literature on hydrophobic powders covering wetting and dynamic wet granulation has been reviewed. This review was to rationalize the theoretical and experimental work that was undertaken for this current thesis contribution. Key gaps have been identified in the reviewed literature of hydrophobic powders:

- *Powder Wetting Phenomena*: Competing liquid droplet spreading and imbibition mechanisms on a solid surface have been discussed. However, these have been limited to applications were the structure of the substrate doesn't change during the liquid spreading process. This makes the liquid binder selection during formulation development in the pharmaceutical industry problematic.

- *Powder Wetting Phenomena*: The importance of the initial interaction between the primary powder particles and liquid binder has been discussed. Contact angle has been described as one of the key parameters used to describe the affinity of a liquid to the primary powder particles. The theories that predict the contact angle have been highlighted. However, it was found that the commonly used Cassie-Baxter theory that predicts contact angle on two-component mixtures was invalid and the inconsistencies observed have been overlooked in literature.

- *Twin Screw Wet Granulation*: A review of the importance of continuous TSG in the pharmaceutical industry is given. Although continuous TSG is seen as key in the future of pharmaceutical production, the dependence of powder wetting properties on continuous TSG operating variables on the resultant granule properties has been overlooked. Moreover, it is not known whether a correlation between these two factors can be applied universally to allow for process scale up of granule properties.

It is therefore the aim of this thesis to attempt to add knowledge to these gaps in order to provide a scientific platform to enable effective formulation development and process design in the pharmaceutical industry.

3 EXPERIMENTAL MATERIALS AND METHODOLOGY

The materials and methodologies used for the experimental investigations presented in this thesis are described below.

3.1 Materials

3.1.1 Primary Powders

The formulation was comprised of lactose monohydrate 200 M (DFE Pharma) and magnesium stearate (Ligamed) which were used as hydrophilic and hydrophobic primary powders respectively. Lactose monohydrate is a white, regularly structured and mostly crystalline powder which is commonly used as an excipient in the pharmaceutical industry (see Figure 3-1).
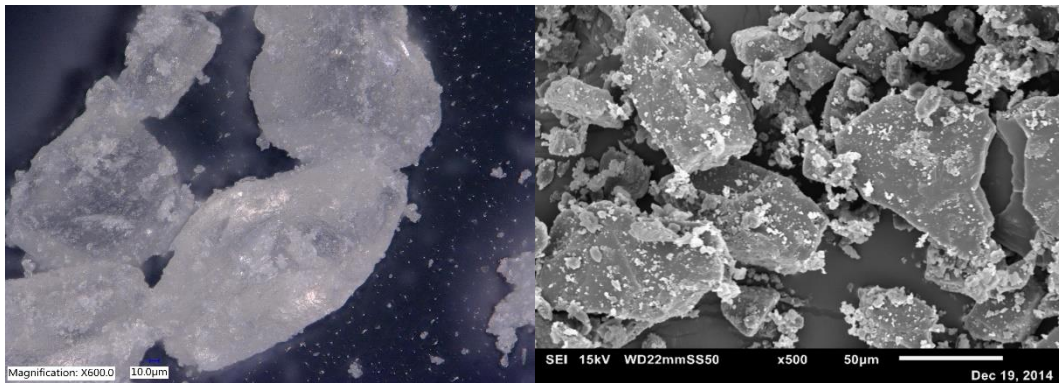
Figure 3-1. Microscope and Scanning Electron images of primary particles of Lactose Monohydrate.
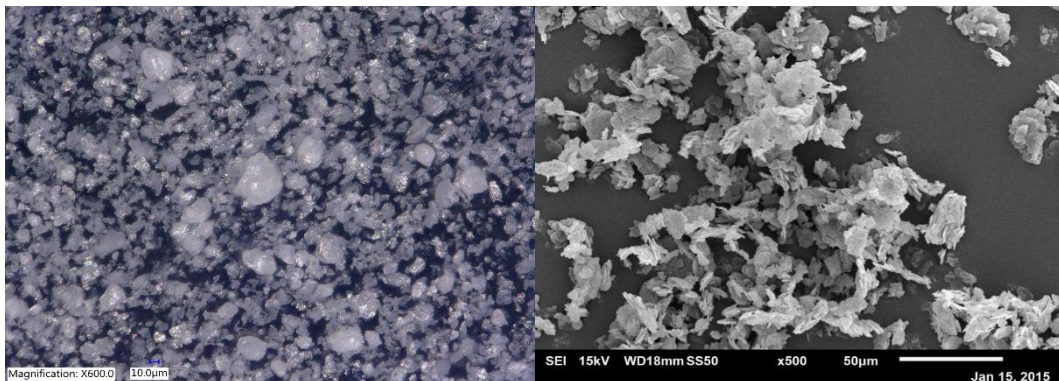
Figure 3-2. Microscope and Scanning Electron images of primary particles of Magnesium Stearate.

Magnesium stearate is a fine powder commonly used as a lubricant due to its excellent anti-adhering properties in concentrations less than 2 % during the tableting compression stage (see

Figure 3-2). However, in this work magnesium stearate is used as a model hydrophobic active ingredient.

In the pharmaceutical industry, powder systems are typically mixtures. Therefore, in order to investigate the influence of powder wetting properties, two-component mixtures have been prepared. The composition of the mixtures is given in Table 3-1. Prior to any experimental investigations, the mixtures were premixed for 5 min at 150 rpm in a mixer (Roto junior, Zanchetta). Mixing of powders was carried out by sampling (top, middle, bottom) on different parts of the granulator, until the variation in composition across was giving an error of ±0.1 % to ensure that they are adequately mixed.

Table 3-1. Two component mixtures used, where ϕ is the volume fraction

Lactose Volume Fraction (ϕ)	1.00	0.93	0.87	0.74	0.52	0.24
Magnesium Stearate Volume Fraction (1 − ϕ)	0	0.07	0.13	0.26	0.48	0.76

3.1.2 Liquid Binders

To study the wet granulation mechanism, the liquid binder properties μ and γ_{LV} were considered as these will influence how the primary powder particles and liquid binder interact. The liquid binder comprised of polymer where solutions of different concentrations were prepared by dissolving the solid polymer in water in 25 ˚C under constant agitation (200 rpm). To these solutions the hydrophilic component (lactose monohydrate type, 10 g/ 100 ml) was added to minimise the effect of dissolution of the hydrophilic component during experiments to form saturated liquid binder solutions. A dye erythrosine B (Sigma.Aldrich, UK) or quinoline yellow E104 (Fiori Colori, Italy) 1 g was added to the liquid binder to assist with the visual observations of the granules. The μ and γ_{LV} were measured using a rotational rheometer (Malvern, UK) and wilhelmy plate tensiometer (Kilbron, UK) respectively. The liquid binders used and their properties are given in Table 3-2.

Table 3-2. Properties of the liquid binders

Liquid Binder (Polymer)	Supplier	Concentration (wt.%)	Viscosity (mPa · s)	Interfacial tension (mN/m)
Water	n/a	0.0	1.00±0.02	72±3.50
Polyvinylpyrrolidone (K.29/32)	Ashland	5.0	2.30±0.10	60±1.00
Starch (1500)	Colorcon	5.0	3.20±0.10	58±1.00
Hypromellose	Shin.Etsu	1.0	1.56±0.20	47±0.80
		2.5	3.10±0.03	49±1.30
		5.0	9.40±0.20	41±0.80
Hypromellose + Lactose	Shin.Etsu/ DFE Pharma	1.0 (saturated)	3.67±0.08	44±1.40
		2.5 (saturated	6.10±0.12	46±0.70
		5.0 (saturated)	13.17±0.15	44±0.67

3.2 Methods

3.2.1 Static Powder bed

Single liquid droplet experiments were conducted to investigate the static powder wetting behaviour. To prepare for the powder bed, mixtures were compressed under slight compression using a 3300 single column universal testing system (Instron, UK) to make tablets of equal porosities ($\varepsilon \sim 0.10$), thus allowing for a comparative study.

A sessile drop method, (see Figure 3-3) was used to measure the primary powder wetting behaviour by depositing the liquid droplet, $V_0 = 15$ µl dispensed from an electronic pipette onto the powder bed surface. The liquid droplet deposition height was kept constant at 50 mm (U= 0.99 m/s). A high-speed camera (Photron, UK) was used to capture the liquid spreading behaviour on the primary powder bed.
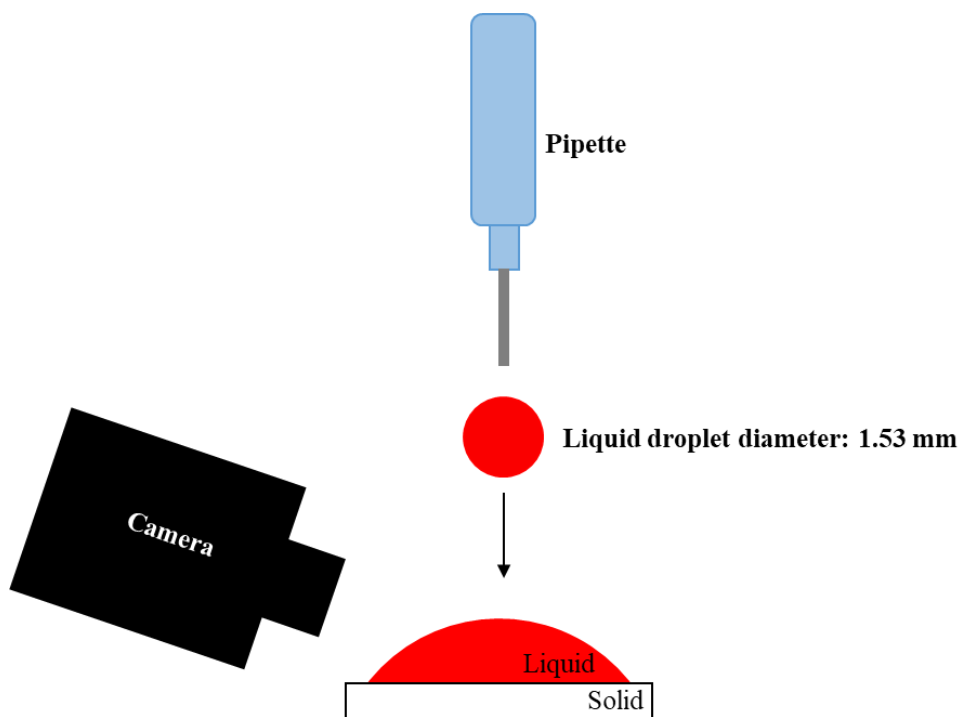
Figure 3-3. Sessile liquid droplet method.

3.2.2 Twin Screw Granulation

The TSG experiments were carried out using a co-rotating TSG Euro Lab 16 mm (Thermo Fisher Scientific, UK) with a horizontal split barrel of 25:1 L/D ratio. A gravimetric loss in weight twin screw feeder was used to feed the mixtures into the TSG at 1 kg/hr at a screw speed of 100 rpm. A peristaltic pump was used to feed the granulation liquid into the TSG using a single tube with a 2 mm inner diameter above the centre of the screw, located after the powder feeding compartment.

Table 3-3. Experimental Design

Lactose Volume Fraction (ϕ)	1.00	0.93	0.87	0.74	0.52	0.24
Magnesium Stearate Volume Fraction ($1-\phi$)	0	0.07	0.13	0.26	0.48	0.76
L/S Ratio	Low = 0.06; Opt = 0.1		Low = 0.1; Opt= 0.14		Low = 0.2; Opt= 0.24	

It was not possible to use a fixed L/S ratio for all the mixtures investigated. Therefore, the L/S ratios for each formulation were optimized (opt), (see Table 3-3) to achieve a desired granule size range between 0.20 – 0.30 mm for good flow-ability, compressibility and low segregation potential in downstream processing i.e. tabletting. When the TSG barrel temperature and torque has reached steady state, batches of granules were collected from the outlet and air dried at room temperature before further analysis.

3.3 Characterisation

3.3.1 Particle Size

Particle size measurements were performed using a Camsizer X-Jet with high pressure dispersion (Retsch, Germany). The basic measurement principle of the equipment is that the primary powder particles are feed into the sample analysis area using a vibrating feeder. The dispersed particles fall into the chute, passing in front of two LED light sources where the shadows of the particles are captured by two digital cameras (high resolution and larger field view). The high-resolution camera analyses the small particles whilst the second camera with a larger field of view detects larger particles. The optical paths of both cameras intersect in the measurement area, where the particle size is calculated in real time. The equipment can detect particles in the range of 1 – 3000 µm. The pressure dispersion module of the equipment was set to 200 kPa to minimize agglomeration of particles and to 20 kPa which is the lowest pressure to prevent granule breakage.

Table 3-4. Two component mixtures used, where ϕ is the volume fraction

Lactose Volume Fraction (ϕ)	1.00	0.93	0.87	0.74	0.52	0.24	0
Magnesium Stearate Volume Fraction ($1 - \phi$)	0	0.07	0.13	0.26	0.48	0.76	1.00
Mean Particle size (μm)	45±1.4	39±1.7	35±1.3	28±1.1	19±1.4	13±1.9	13±1.2

3.3.2 Fines (un-granulated material)

The mass of fines, defined as < 150 μm from each batch were determined using a sieve shaker (Retsch, Germany). A batch of dry granules which were collected from TSG were sieved for 3 min at an amplitude of 1.00 mm through a nest of sieves having a $\sqrt{2}$ sieve size progression (150 – 1700 μm). In the pharmaceutical industry, granule sizes of > 150 μm, typically 200 - 250 μm, are commonly required to produce product with good manufacturability and content uniformity attributes.

3.3.3 Granule Strength

The granule strength was measured by compressing a bed of 0.5 g of granules using a uniaxial confined compression testing machine (Zwick/Roell Z, Germany) with a PC for real time data logging and analysis. A stainless steel die with a 10 mm diameter was used. The granules were compressed at the rate of 5 mm/min to an upper force limit of 450N to obtain force-displacement data. This data was fitted to Equation 3-1 to obtain the granule strength according to the method described by Adams et al. (1994) [106]:

$$\text{In } P = \text{In}\left(\frac{\tau}{\alpha}\right) + \alpha\epsilon_n + \text{In}(1 - e^{-\alpha\epsilon_n})$$

Equation 3-1

where, P is the applied pressure, τ is a constant related to the granule, α is a pressure coefficient and ϵ_n is the natural strain of the bed.

3.3.4 Granule Porosity

A MicroCT X-ray tomography (Bruker, Belgium) was used to observe the internal structure of the granules and tablets. Granules in the size range of 1700 - 1800 μm were selected randomly and scanned to a resolution of 3.0 μm pixel size through 180˚ with a 0.7˚ rotation at 40 kV. The raw images were reconstructed into layers of 2D cross sectional images and the internal granule and tablet porosity (ε) was measured using the SkyScan software by selecting a threshold of the images which was maintained for all samples.

3.3.5 Visualisation of Granule Liquid Distribution and Shape

Visualisation of granule liquid binder distribution and shape was captured by taking images using a VHX 100 microscope (Keyence, UK) of the granules in their wet state immediately after collection from TSG outlet. If images were taken after the granules had fully dried, handling and dye migration would distort the results.

3.3.6 Residence Time Distribution

The residence time distribution (RTD) was measured using an Extruvis.3 (Extruvis, Germany). This equipment consists of a camera (USB-Cam-052H) with a resolution of 2593 x 1944 pixel and a ring light (VZ-001-X4). The RTD is measured by placing the Extruvis.3 at the end of the TSG exist, when the TSG has reached steady state, a tracer is added to the powder inlet port and the colour intensity of the granules is measured as they exit the TSG. The RTD is measured as a function of time using:

$$E(t) = \frac{C(t)}{\int_{t_1}^{t_{out}} C(t)dt}$$

Equation 3-2

where $E(t)$ is the RTD function, C is the concentration of tracer, t_1 is the time the tracer is first detected and t_{out} is the time the tracer is first out.

From the RTD, the mean residence time ($\bar{t}_m$), plug flow fraction (p) and back mixing (φ) were calculated to gain insight into the extent of mixing in the TSG [107]:

$$\bar{t}_m = \frac{\int_{t_1}^{t_{out}} tCdt}{\int_{t_1}^{t_{out}} Cdt}$$

Equation 3-3

$$p = \frac{t_1}{\bar{t}_m}$$

Equation 3-4

The value of p describes the conveying rate inside the TSG, where if $p = 0$ there is no plug flow whereas if $p = 1$ there is plug flow.

$$\frac{C}{C_0} = e^{-\frac{t}{\bar{t}_m}}$$

<div align="right">**Equation 3-5**</div>

For a perfectly mixed/completely backmixed system, the decay in the tail after $\bar{t}_m$ is in the form of an exponential decay (see Equation 3-6). A plot of In (C/C_0) versus t should be linear with the coefficient of determination $R^2 = 1 \rightarrow 100\%$ φ. Excellent linear fit to data indicate a perfectly mixed/completely backmixed system. However, operating the TSG at above $\Psi > 50\%$ can cause excessive stress build up, increasing the torque above its performance. Visual analysis of the screws was carried out by running the experiment until a steady state, when the system torque is constant was reached. Subsequently, TSG was halted and images of the screws were taken by opening the barrel.

3.3.7   Compositional Analysis of Granules

To measure the distribution of single components in the granules, a Helios Hyperspectral Short-Wave Infrared Imaging camera (Helios SWIR G2.32OS, Austria) was used, a Near Infra-Red Chemical Imaging Surface Technique. This is a non-contact technique which measures in the spectral range of 0.9 - 2.23 μm, at a frame rate of 120 Hz using a HgCDTe sensor with a spatial resolution of 312 effective pixels.

The samples are placed on a linear stage then moved beneath the detector at a constant velocity during measurement. This technique is based on the push broom technique were one line of a sample is detected after another. These lines are further subdivided into pixels in which spectra are generated. Figure 3-4 illustrates an example of NIR.CI spectra obtained for the primary powders used. The key absorption bands that distinguish the primary powders are also indicted. To interpret the spectra generated, inbuilt multivariate statistical methods that is principal particle analysis (PCA) and partial least square regression (PLS) were applied.

For each spectrum generated, PCA is applied to reduce the data set through optimization with respect to the significant compositional variation between the samples. These variations are projected onto latent variables which are a linear combination of wavelengths. The variations represent the different chemical compositions that are detected on the samples, (see Figure 3-4).
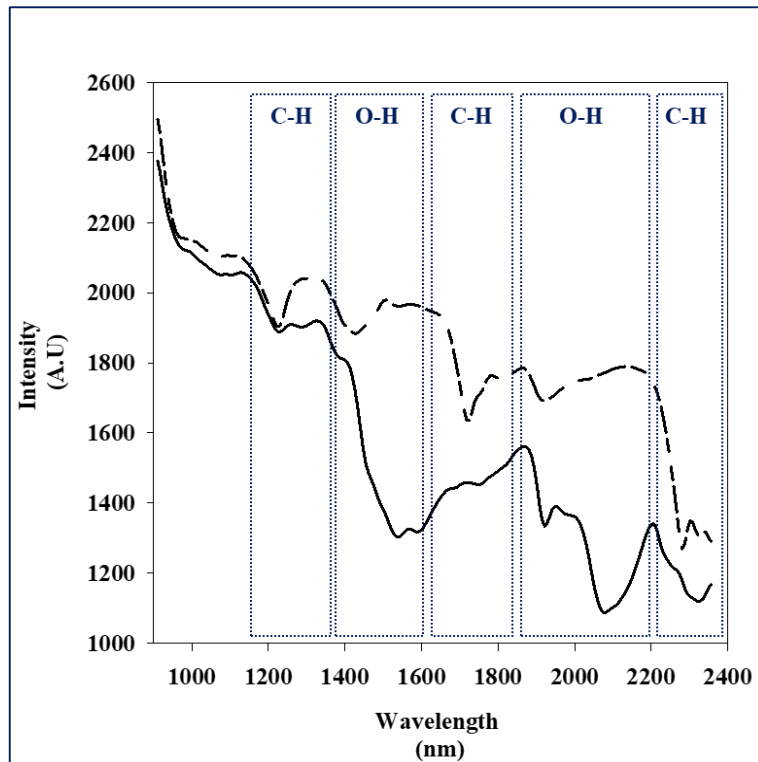
Figure 3-4. Raw NIR-CI spectra for primary powders used. Lactose 200M is represented by the solid line and Magnesium stearate is represented by the dashed line.
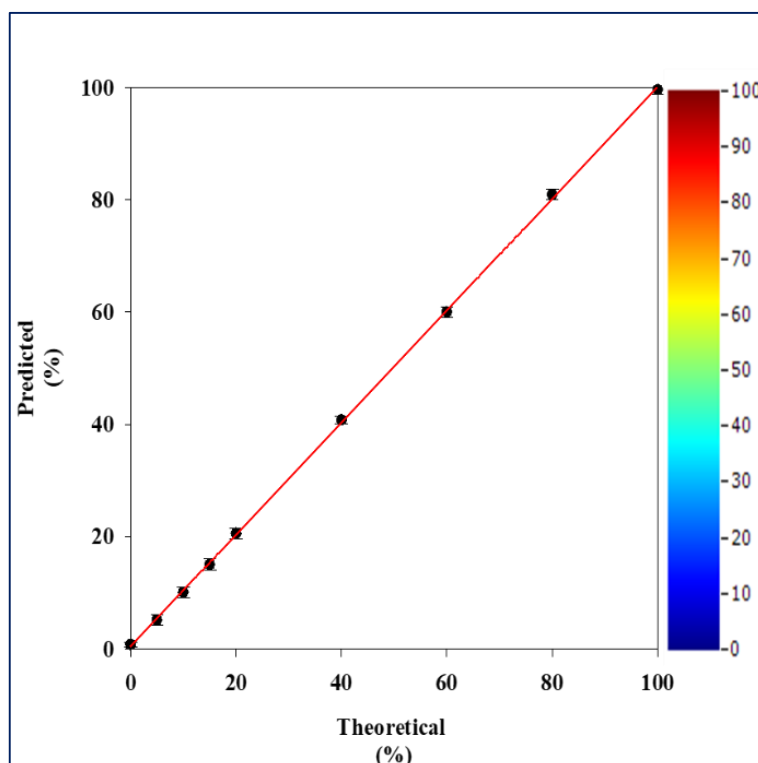
Figure 3-5. Prediction of Magnesium Stearate composition.

The principle of PCA is extended from qualitative to quantitative analysis by creating a calibration graph using pure and mixed powders (ratio) to develop a PLS model to predict

55

composition fine magnesium stearate particles in the sample, (see Figure 3-5). As the mixtures were premixed before measurement it is assumed that they are stochastically uniform. The resulting calibration graph is shown in Figure 3-5. Variations in the chemical composition of the samples are clearly distinguishable. The resulting PLS model sufficiently predicted the theoretically expected composition.

3.3.8   De-mixing Potential

The distribution of particles across different granule size classes was quantified using the coefficient of variation (cv):

$$cv = \frac{\sigma}{\bar{x}}$$

Equation 3-6

where σ is the standard deviation and $\bar{x}$ is the mean of the fine particle composition results

and de-mixing potential:

$$DP(\%) = \frac{100}{\bar{p}} \sqrt{\sum \frac{w(p_C - \bar{p})^2}{100}}$$

Equation 3-7

where $\bar{p}$ average concentration of fine particles, p_C is the actual concentration of the fine particles in each size class with weight percent (w). The de-mixing potential looks at the coefficient of variation of the fine magnesium stearate particles in each fraction and its implication is that the smaller it is, the less likely it is for materials to segregate (the de-mixing potential should be preferably less than 0.2).

4 HYDROPHOBIC/HYDROPHILIC STATIC POWDER BEDS: COMPETING HORIZONTAL SPREADING AND VERTICAL IMBIBITION MECHANISMS OF SINGLE LIQUID DROPLET

4.1 Introduction

In Chapter 2, it has been discussed that there is no experimental evidence on the existence of the competing liquid spreading and imbibition mechanisms of single droplets impacting hydrophobic powder beds. This chapter extends the studies of competing liquid spreading and imbibition mechanisms to focus on the influence of powder bed wettability, which remains a critical experimental issue in the pharmaceutical field.

There are two competing mechanisms of a single liquid droplet impacting on static powder beds, (see Figure 4-1). The d_h spreading describes the length the liquid droplet travels horizontally across the powder bed, whereas the d_v imbibition is the length the liquid droplet travels vertically into the powder bed.
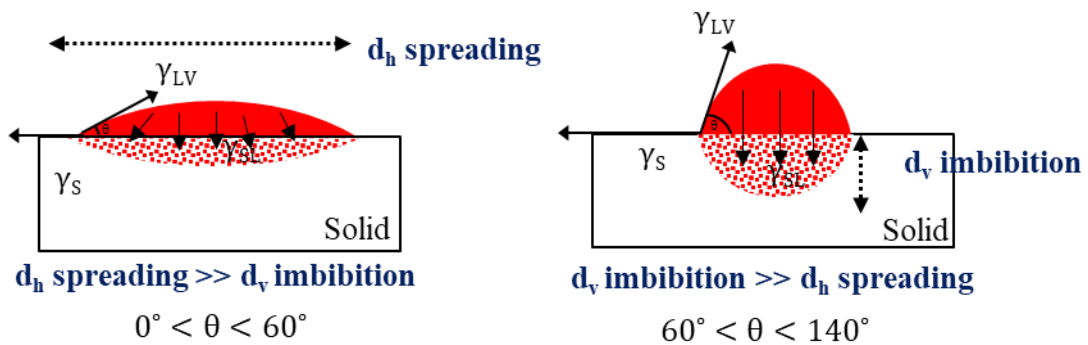
Figure 4-1. Competing spreading mechanism of a single liquid droplet.

In this work, results are presented from an experimental study of single liquid droplets of varying μ impacting static hydrophilic and hydrophobic powder beds. By using a high-speed video camera, the dynamics of the droplet spreading behaviour on static powder bed compacts was captured. The resultant nuclei were then analysed. Understanding of single droplet spreading mechanisms provides a basis to select the optimal binder for granulation to form more uniform and robust granules when using hydrophilic and hydrophobic formulations.

4.2 Experimental Design

The liquid binders and powder mixtures used in this chapter are detailed in section 3.1.1 - 3.1.2. However, $\phi = 0.52$ and , $\phi = 0.24$ were not studied as imbibition of the liquid droplet was negligible, this will be explored in later sections. The sessile liquid droplet method used is described in section 3.2.1. The liquid droplet spreading behaviour was captured using a high speed camera the images were used to extract information on the d_0, d_h, h_0, h, t_{dp} and the maximum apparent contact angle (θ^*).
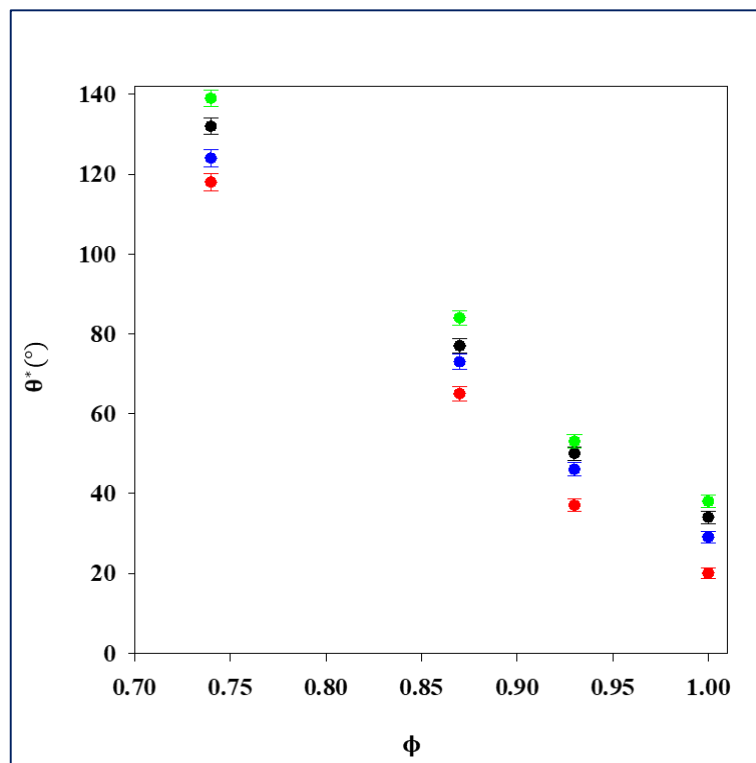
Figure 4-2. A summary of the θ^* the different powder beds and μ (m Pa s): ●1.00, ●2.30, ●3.20, ● 9.40.

A summary of the θ^* is presented in Figure 4-2 were $0° < \theta^* < 60°$ and $60° < \theta^* < 140°$ are defined as formulations that display good and poor wetting respectively. The resultant nuclei were collected after complete imbibition of the liquid droplet into the powder bed and their diameter (d_{nuclei}) and mass were measured. Furthermore, the nuclei were cut in half in the direction perpendicular to the plane of d_h spreading to measure the d_v imbibition length.

4.3 Horizontal Spreading

Tables 4-1 - 4-2 illustrates the time-based image sequence of liquid drops of different μ impacting on powder beds of different hydrophobicity characterized by θ^*, (see Figure 4-2).

Table 4-1. Images showing the time dependence of the droplet spreading behavior for μ = 1.00 m Pa s
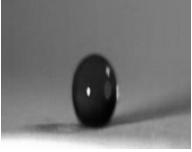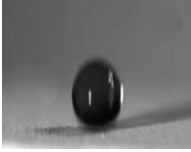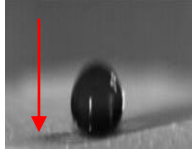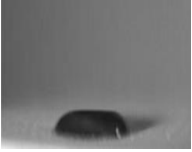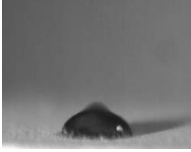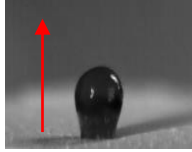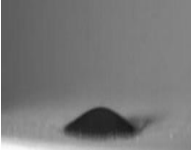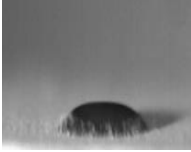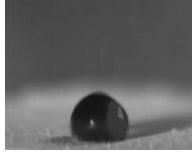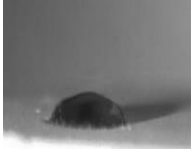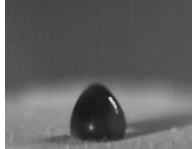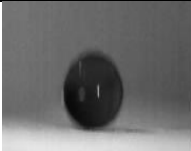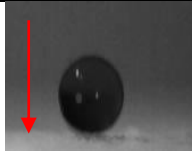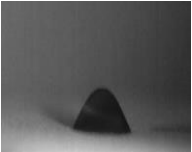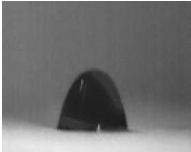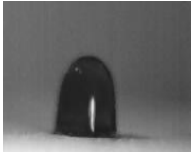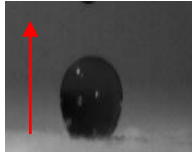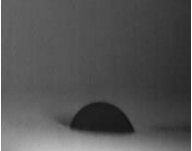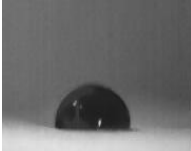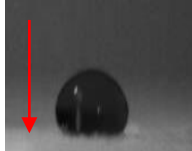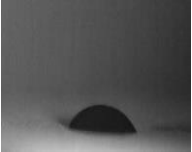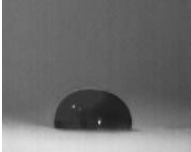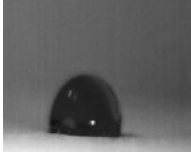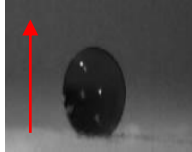
Time (s)	ϕ = 1.00	ϕ = 0.93	ϕ =0.87	ϕ = 0.74
0				
0.10				
0.20				
0.30				

Table 4-2. Images showing the time dependence of the droplet spreading behavior for μ = 9.40 m Pa s

Time (s)	ϕ = 1.00	ϕ = 0.93	ϕ =0.87	ϕ = 0.74
0				
0.10				
0.20				
0.30				

The rebound and shape distortion of the liquid droplet increases with viscosity, where in some cases retraction of the liquid droplet from the surface is observed. This suggest that the inertial effects are not dissipated rapidly with increased viscosity, therefore rebound is prolonged. Liquid droplet imbibition into the powder bed will not begin until it reaches its maximum horizontal spreading when the high interfacial energy is dissipated [65]. In all cases

the droplet remains as a semi-spherical cap, with time throughout the horizontal spreading processes. This semi-spherical cap allowed for the time-based evolution of the d_h/d_0 and h/h_0 to be measured.
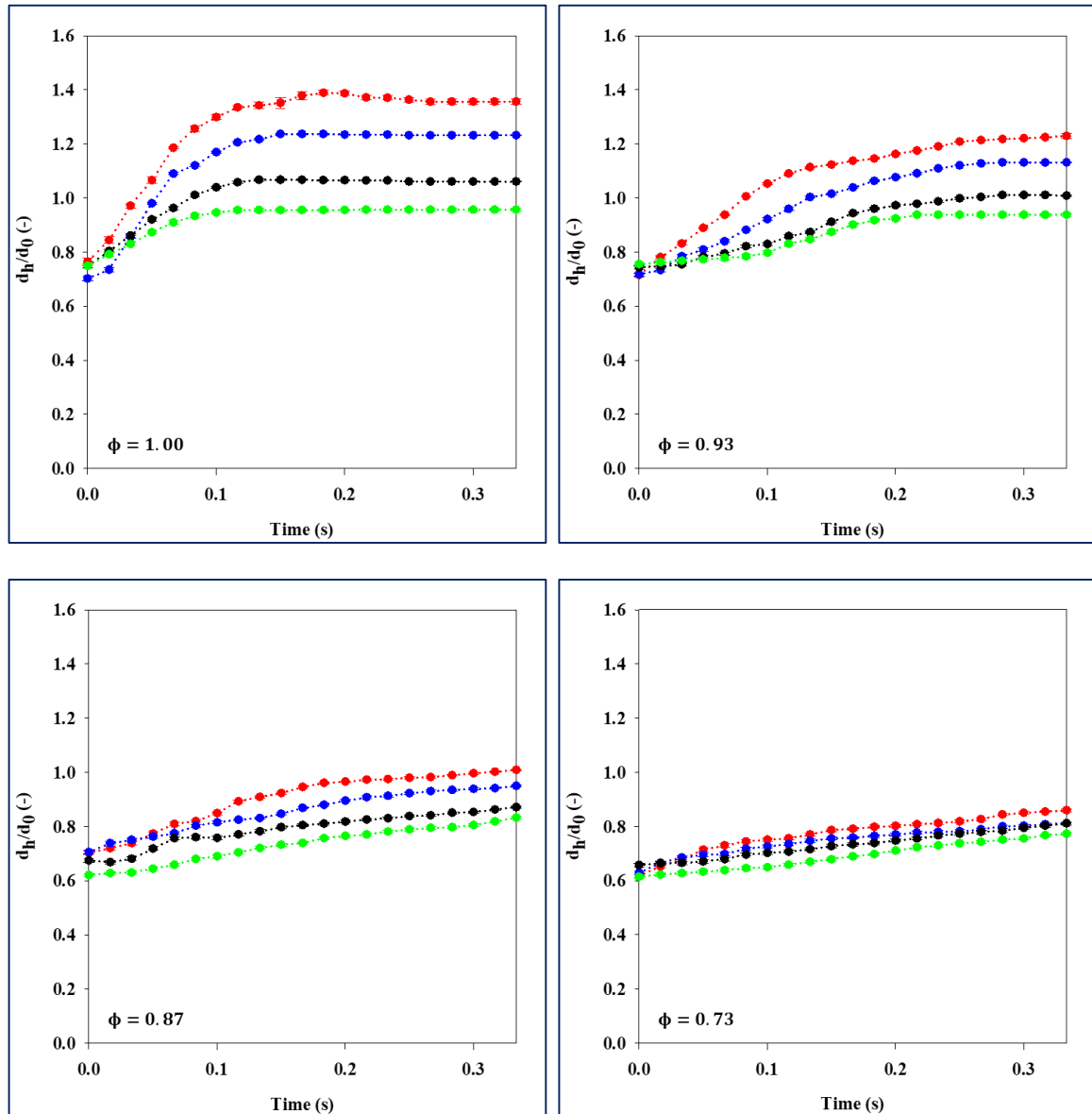
Figure 4-3. Early time-based evolution of the liquid droplet horizontal spreading presented at a d_h/d_0 for different powder beds and μ (m Pa s): ● 1.00, ● 2.30, ● 3.20, ● 9.40.

Figure 4-3 illustrates the time-based evolution of the normalized drop parameters d_h/d_0 when a liquid drop contacts the surface for different powder beds and μ. The drop parameters are characteristic of the liquid droplet horizontal spreading process. The results presented only consider the initial stage of the liquid droplet spreading process. Initially the liquid droplet horizontal spreading is driven by kinetic effects, however, the viscous drag effects retards the liquid droplet kinematics (velocity), (see Figure 4-3) [28,108]. This retardation results in the

horizontal spreading on the powder bed surface reaching a smaller maximum spread in a shorter time frame with increase in viscosity, (see Figure 4-4).
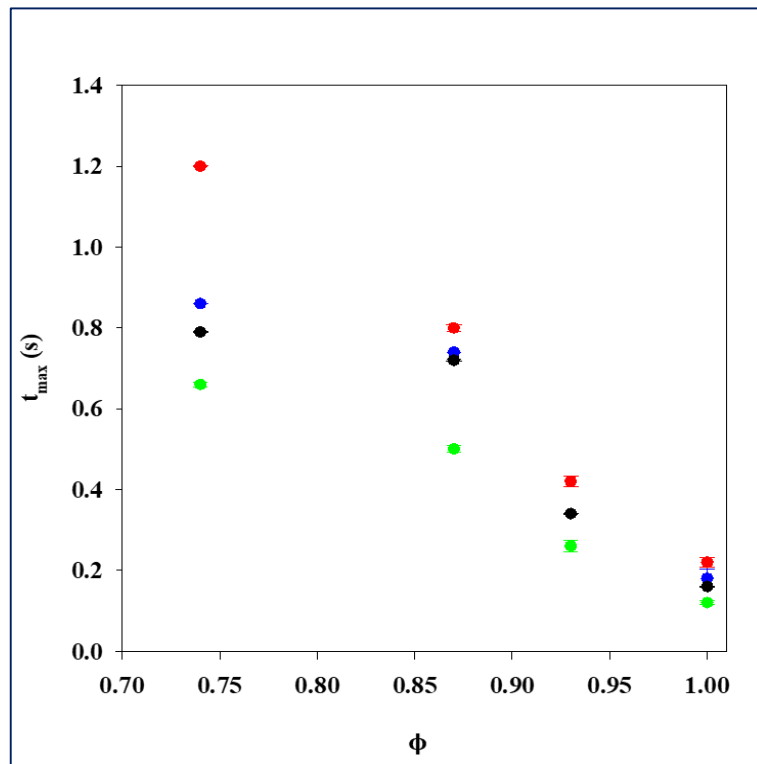
Figure 4-4. Time the liquid droplet is at its maximum horizontal spreading before imbibition into the powder bed versus ϕ for different powder beds and μ (m Pa s): ● **1.00,** ● **2.30,** ● **3.20,** ● **9.40.**

Figure 4-5 illustrates the relationship between the spreading factor (non-dimensional) defined as the maximum horizontal spreading (d_h/d_0) on the powder bed surface before liquid droplet imbibition and the nuclei diameter (d_{nuclei}/d_0) after complete imbibition into the powder bed. Here, it is clearly observed that the liquid droplet continues to spread after complete imbibition into the powder bed in a process termed late diffusive intra-spreading of a liquid droplet inside a powder bed. The late diffusive intra-spreading process is driven by capillary forces, but was also retarded by viscous forces. The correlation between viscosity and the spreading factor confirms that at increased viscosity there is competition between viscosity and the liquid droplet kinematics (velocity).

61
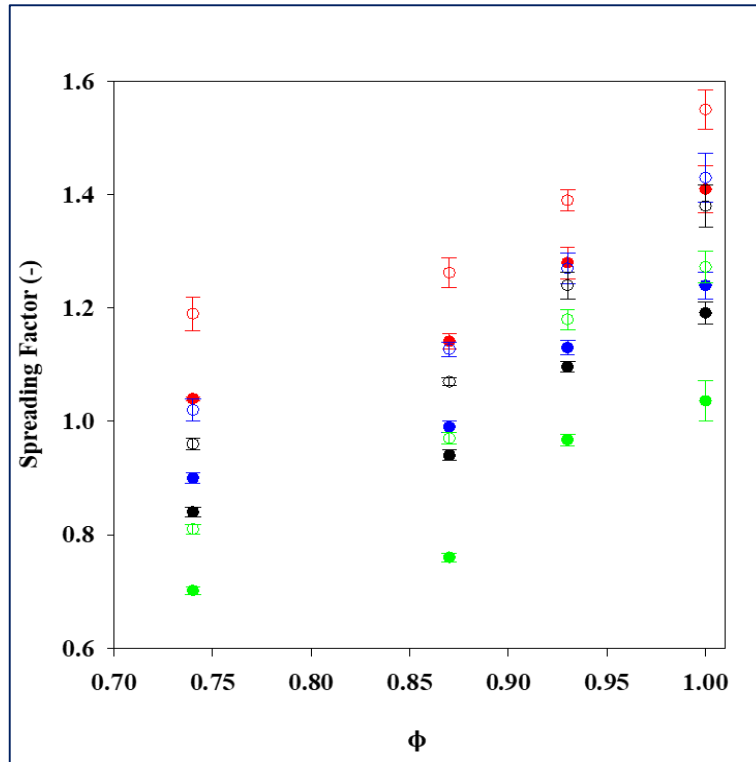
Figure 4-5. Comparison between the non-dimensional spreading factor which represents the maximum horizontal spreading diameter (d_h/d_0) before the liquid droplet imbibition into the powder bed μ (m Pa s): ●1.00, ●2.30, ●3.20, ●9.40 and non-dimensional resultant nuclei diameter (d_{nuclei}/d_0) after complete liquid droplet imbibition into the powder bed μ (m Pa s): ○1.00, ○2.30, ○3.20, ○9.40.

There is a threshold where the influence of viscosity on the dynamic horizontal spreading becomes limited. This occurs when $60° < \theta^* < 140°$ where the solid-liquid interactions are reduced within the three-phase contact line, (see Figures 4-2 - 4-3 and Tables 4-1 - 4-2). A three-phase contact line is where a solid, liquid and vapour co-exist. The reduction of the solid-liquid interactions slows down (delays) the liquid droplet horizontal spreading process as indicated by the relative constant drawing diameter (normalized), (see Figure 4-3).

For the spreading process to proceed at high θ^*, there must be enough driving force from either gravitational or diffusion forces to overcome the effects of the reduced solid-liquid interactions [63]. The work of the driving force is balanced by dissipation, primarily hydrodynamic dissipation in the vicinity of the contact line. This suggests that there is an explicit time dependence of the liquid droplet spreading process with increase in θ^* which is plausible as illustrated in Tables 4-1 - 4-2.

The time dependence of the spreading process (rate and total time), results in the maximum spreading being reached at a longer time frame with increase in θ^*, (see Figure 4-4). This observation of longer time frame was significant for powder beds where $60° < \theta^* < 140°$ than

62

$0° < θ^* < 60°$. These results show that the $θ^*$ has significant influence on the initial kinematic stage of the liquid droplet spreading process in agreement with the experimental and numerical observations [39]. From these results it is concluded that the time dependent behavior of the liquid droplet spreading process means that its rate can also be used to distinguish between the t_{CDA} vs t_{DDA} phases, two types of liquid droplet imbibition into the powder bed, (see Chapter 2.41).

When $0° < θ^* < 60°$, the liquid droplet spreading process occurs at a faster rate resulting in shorter time required to reach the maximum horizontal spreading for these powder beds, (see Figures 4-3 – 4-4). This means that the liquid droplet spreading process is not time dependent during a t_{CDA} phase. However, when $60° < θ^* < 140°$ the liquid droplet spreading rate decreases until there is enough driving force (gravitational or diffusion effects) for the spreading to proceed. This time dependent behavior means that the spreading at $60° < θ^* < 140°$ is occurring over the t_{DDA} phase. Therefore, the liquid droplet spreading rate lies within the t_{CDA} and t_{DDA} phases with increase in $θ^*$. To further confirm this transitional behavior of the liquid droplet spreading phases, the imbibition times for a liquid droplet to fully penetrate the powder bed were measured, (see Tables 4-1 - 4-2).

Table 4-3. Imbibition times (t_{dp}) of liquid drops impacting different powder beds for different μ

φ	Time (s) ($μ = 1.00$ m Pa s	Time (s) ($μ = 2.30$ m Pa s	Time (s) ($μ = 3.20$ m Pa s	Time (s) ($μ = 9.40$ m Pa s
1.00	0.4±0.04	0.8±0.22	1.4±0.05	2.2±0.09
0.93	1.8±0.14	5.3±1.0	6.4±.07	17±0.36
0.87	10±1.49	32±2.87	42±2.10	62±4.23
0.74	689±10	737±15	784±9	964±12

Table 4-3 illustrates a summary of the t_{dp} results for different powder beds characterized by $θ^*$ and viscosities. The imbibition process is driven by capillary action when the liquid droplet is at its maximum horizontal spreading. When the $θ^*$ is increased, (see Figure 4.1, Tables 4-1 - 4-2), the t_{dp} increases more than 2 orders of magnitude higher than that observed for low $θ^*$ (see Table 4-3). This demonstrates that the liquid droplet imbibition process changes from t_{CDA} to t_{DDA} behavior with increase in $θ^*$. In the t_{CDA} case, the small $θ^*$ and larger horizontal spreading means that a larger number of pores are available for imbibition and the

contact line will decrease rapidly in a shorter time frame. which is typical behavior for powder beds that display characteristic hydrophilic behavior.

In contrast, the t_{DDA} behavior is typical for liquid drops impacting hydrophobic powder beds, as when the θ^* is increased the imbibition time increases significantly. This increase is attributed to a decrease in the horizontal spreading with increase in the θ^* which results in all available pores on the powder bed surface not being filled as the area the liquid droplet is occupying decreases. The decrease in the liquid droplet horizontal spreading with increase in θ^* means that the liquid droplet will sit on the powder bed surface until it finds a hydrophilic particle pathway in the powder bed for the liquid droplet to flow through. This transition in the spreading and imbibition of the liquid droplet into a powder bed was described to be occurring through site percolation theory [63]. The longer t_{dp} can also be attributed to the decreased porosity of the tablets used in the current study which makes it difficult for the liquid droplet imbibition to be driven by capillary forces only, as the porosity does not contribute to the effective capillary volume. However, the influence of porosity on t_{dp} in this work is considered negligible in comparison to the θ^* as the tablets was compressed to very low porosities.

4.4 Vertical Imbibition

In Figure 4-6, the normalized drop heights (h/h_0) of the liquid droplet on different powder beds are compared to examine the effect of θ^* and viscosity on the vertical imbibition (d_v imbibition).The droplet height (h) corresponds to the vertical distance from the powder surface to the highest point of the drop remaining on the powder bed surface during liquid droplet imbibition.

As can be seen from Figure 4.6, the liquid droplet height reduces very rapidly from a spherical shape to a spherical cap at low viscosity and θ^* until it reaches a minimum value where a thin lamella 'pancake' is formed, (see Tables 4-1) before complete liquid droplet imbibition into the powder bed. This means that at low viscosity and for $0° < \theta^* < 60°$ the liquid droplet will spread further resulting in larger maximum horizontal spreading. However, the contact line is pinned at low droplet volume during imbibition. A larger horizontal spreading diameter means a smaller initial θ^* and larger number of pores available for capillary induced flow, therefore the contact line will recede after a shorter time, (see Table 4-3 and Figure 4-6).
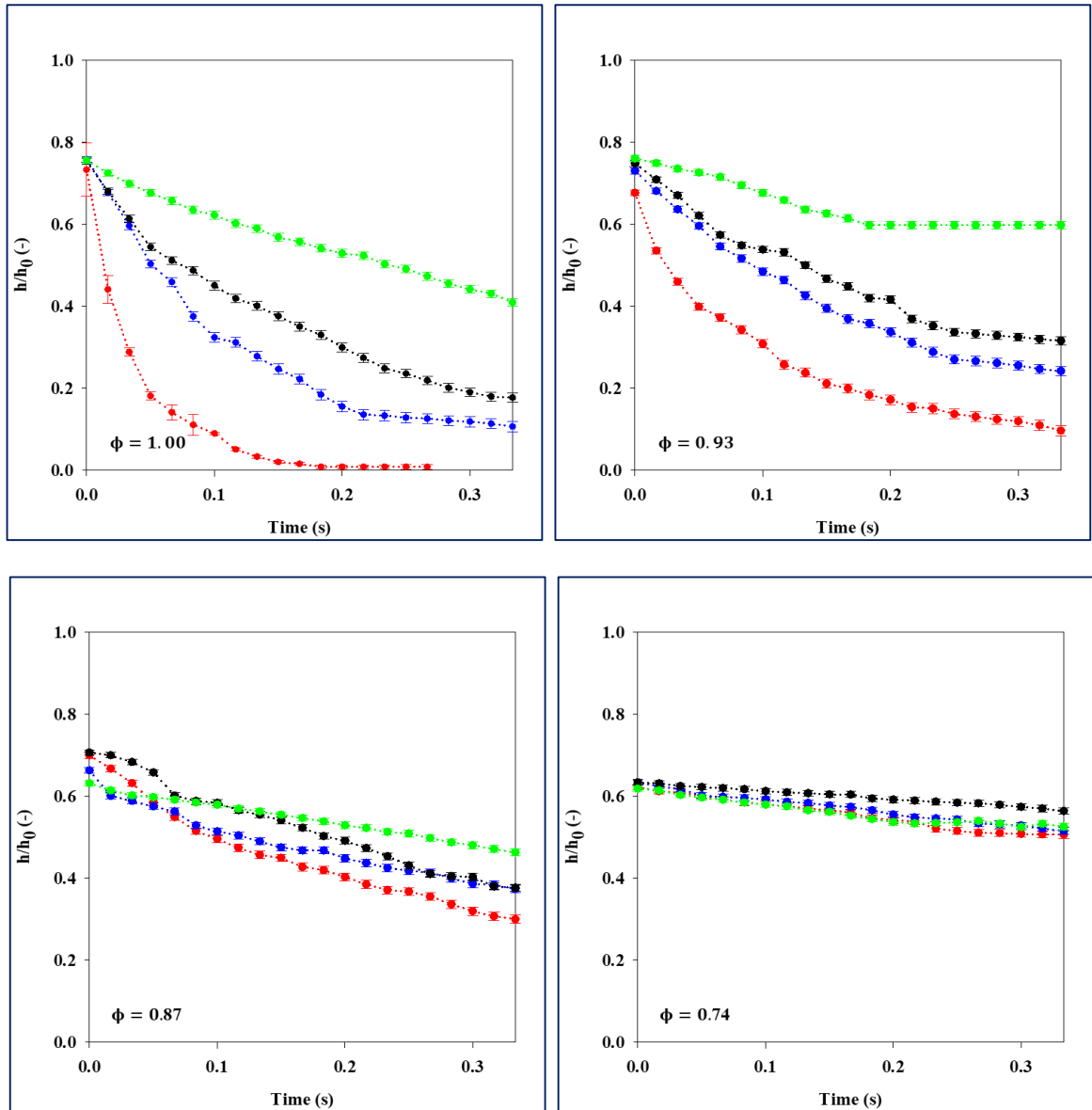
Figure 4-6. Early time-based evolution of the liquid droplet vertical spreading presented as a spreading factor h/h$_0$ for different powder beds and μ (m Pa s): ●1.00, ●2.30, ●3.20, ●9.40.

The liquid droplet height changed from receding rapidly to slowly over a greater time frame with increase in viscosity and for $60° < θ^* < 140°$, resulting in a large volume of the liquid droplet remaining on the powder bed surface as the liquid droplet imbibition was proceeding. This means that the contact line will be pinned at high droplet volume during the imbibition process, leading to higher $θ^*$, (see Tables 4-1 - 4-2). Thus, only a smaller liquid droplet volume has imbibed into the powder bed. These results contradict the experimental results of Charles-Williams et al. (2011) where it was reported that that higher viscous binders spread further horizontally but are pinned at low volume during imbibition [33].
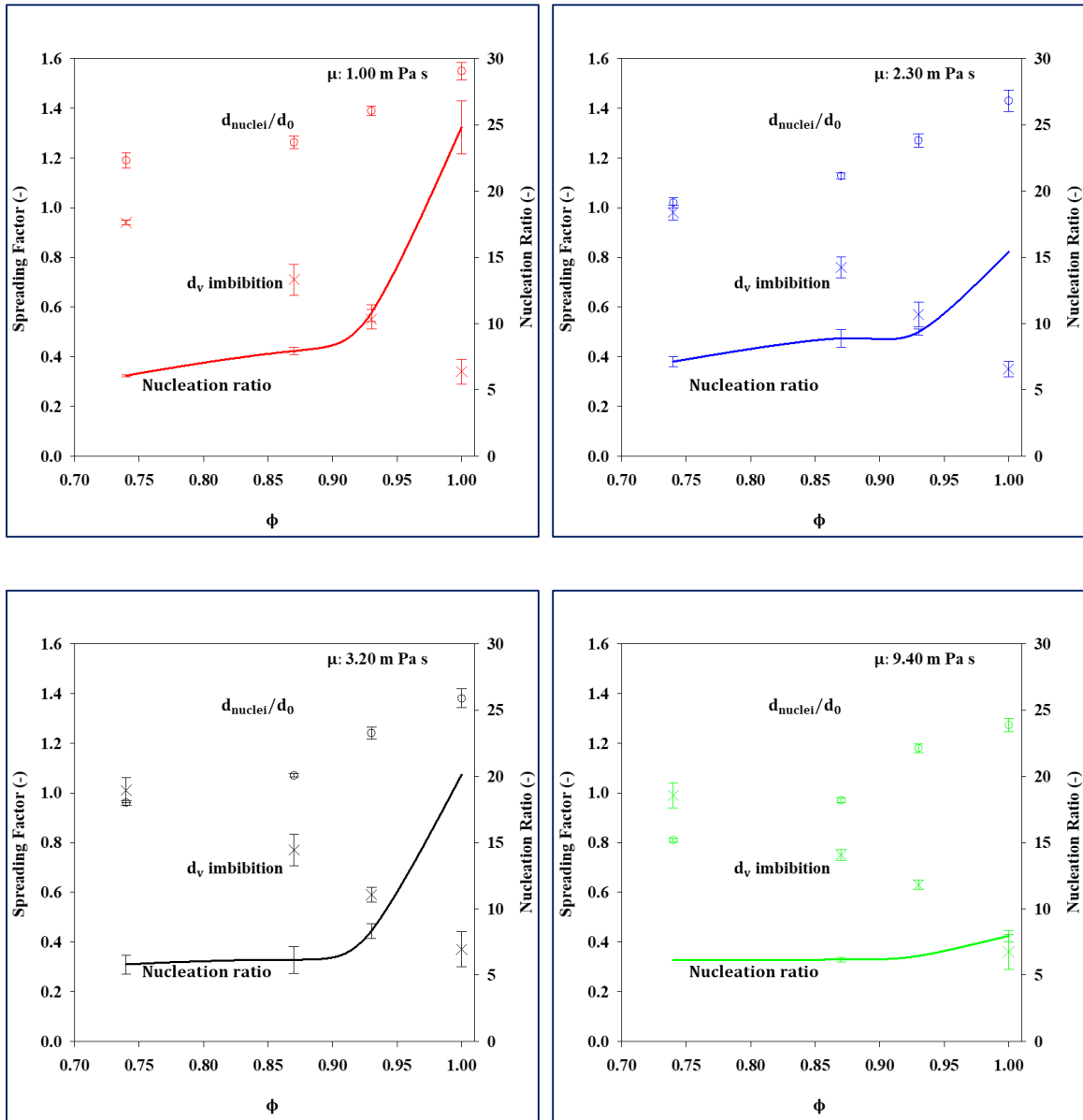
Figure 4-7. Comparison of the spreading factor which represents the maximum nuclei diameter (d_{nuclei}/d_0) after complete liquid droplet imbibition into the powder bed, the nuclei vertical imbibition length (d_v imbibition) and the nucleation ratio.

Figure 4-7, summarizes the variation in the resultant nuclei diameter (d_{nuclei}), nuclei vertical imbibition length (d_v imbibition) and nucleation ratio which were investigated to study the extent of the imbibition process. The d_v imbibition and d_{nuclei} were measured when the liquid droplet had fully imbibed into the powder bed and are normalized using d_0. The nuclei ratio is defined as the weight of the nuclei formed to that of the liquid droplet and is dependent on the liquid and powder bed properties.

Figure 4-7 shows that the d_v imbibition decreases as a function of powder bed ϕ whilst the horizontal spreading of the liquid droplet is increased. This is because with decreased powder

bed ϕ the bulk volume of the liquid droplet sits on the surface for a longer time as the interfacial energies are increased which reduces the liquid volume flow rate. The imbibition of the remaining bulk volume would be driven by gravity and/or diffusion forces which act to pull down the liquid droplet vertically into the powder bed.

As the liquid droplet is migrating vertically, the nucleation ratio will be influenced by how many particles come into contact with the liquid droplet inside the powder bed. For low viscosities and $0° < \theta^* < 60°$ powder beds, the fast imbibition of the liquid droplet dissipates any available interfacial energy rapidly which promotes more particles to be in contact with the liquid quickly resulting in large nucleation ratios (see Figure 4-7). However, for low viscosities and $60° < \theta^* < 140°$ powder beds the high interfacial energy results in weak interaction between the liquid binder and the hydrophobic particles. This will cause the liquid droplet to migrate until it finds a hydrophilic pathway where particles will be picked up due to capillary action, resulting in liquid imbibition occurring via site percolation of the hydrophilic particles. This site percolation mechanism causes less particles to come into contact with the liquid droplet, reducing the nucleation ratio (see, Figure 4-7).

The liquid binder viscosity acts to retard the rate at which the particles come into contact with the liquid droplet during its migration. This also leads to a reduction in the nucleation ratio. The differences observed in the liquid droplet d_v imbibition behavior supports the findings described above on the t_{CDA} vs t_{DDA} phases. This means that when horizontal spreading is greater, there is increased particle interconnectivity which decreases overall liquid droplet imbibition time. Thus, the liquid droplet imbibition process is occurring over a t_{CDA} phase. However, when d_v imbibition is greater, the liquid droplet spreading process is indicative of the t_{DDA} phase. From these results it is suggested that the d_v imbibition behavior explains the site percolation theory for liquid migration for higher θ^*.

4.5 Imbibition Rate

The rate of d_v imbibition into a powder bed is described using Darcy's law which accounts for one dimensional liquid flow along a Laplace capillary pressure gradient [31,65,109]:

$$v_D = \frac{k}{\mu} \frac{2\gamma_{LV} \cos \theta^*}{R_{pore} h}$$

However, the liquid droplet spreading is a three-dimensional process. By considering the liquid-solid contact area, liquid droplet spreading factor (d_h/d_0) and the volume of liquid droplet penetrating the powder bed surface at a specific time, an adimensional imbibition rate $(\bar{v}_D)$ was developed to describe the rate of d_v imbibition [109]:

$$\bar{v}_D = \frac{\left(\dfrac{(V_0 - V(t))}{V_0} \right)}{\left(\dfrac{d_h}{d_0} \right)^2 t}$$

The $\bar{v}_D$ describes the case of d_v imbibition rate more realistic for liquid flow into a substrate and assumes that the d_v imbibition mechanism is time dependent on the liquid droplet volume height (h).

Based on equation 4-1, let,

$$A = \frac{k}{\mu} \frac{2\gamma_{LV} \cos \theta^*}{R_{pore}}$$

Then Equation 4-1 becomes:

$$v_D = \frac{A}{h}$$

The rate of change for h will be:

$$\frac{dh}{dt} = \frac{A}{h}$$

Equation 4-4 is solved analytically to yield a modified Darcy rate law [31]:

$$h \times dh = A \times dt$$

$$\int_0^h h \times dh = A \int_0^t dt$$

$$\frac{h^2}{2} = At$$

$$h \propto t^{0.5}$$

To establish the relative dependency of the competitive d_h spreading and d_v imbibition mechanisms on liquid binder viscosity and powder bed θ^*, the $\bar{v}_D$ which is characteristic of the d_v imbibition rate was determined from Equation 4-2. The power law function t^n, (see Equation 4.9), where the exponent n is a fitting parameter which yields information on the d_v imbibition rate behavior for each curve, were evaluated using linear regression, (see Tables 4-4 - 4-5).

To understand the transitions of the $\bar{v}_D$, the d_v imbibition rate was characterized as a three-regime process as its general trend was observed to be transitioning from an initial increase which slows down as time progresses. The three-regime processes are dependent on capillary, viscous forces or interfacial effects driven regimes. Each regime was chosen to last for a period of 0.07 seconds for the initial regime, 0.10 seconds for the intermediate regime and 0.15 seconds for the final imbibition regime respectively in accordance to the observed trend of $\bar{v}_D$, see Figures 4-8 and 4-9.

Region 1

$$Y = -1.33x - 0.71$$
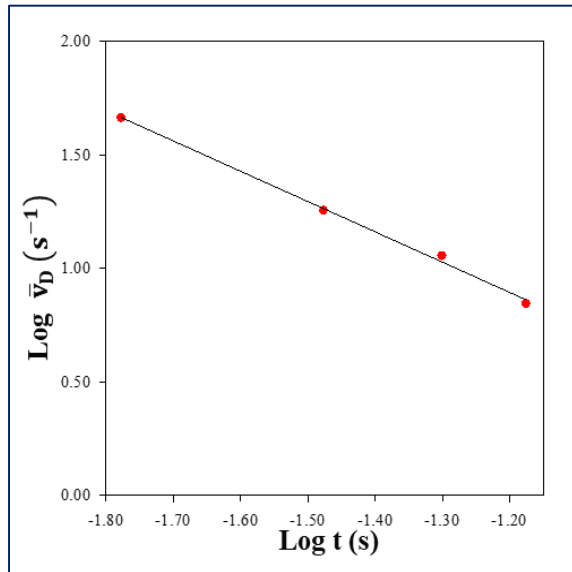
Region 2

$$Y = -0.99x - 0.36$$
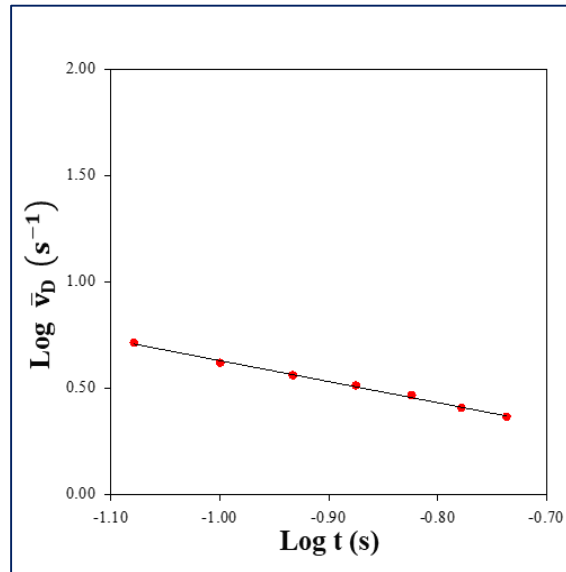
Region 3

$$Y = -0.86x - 0.27$$
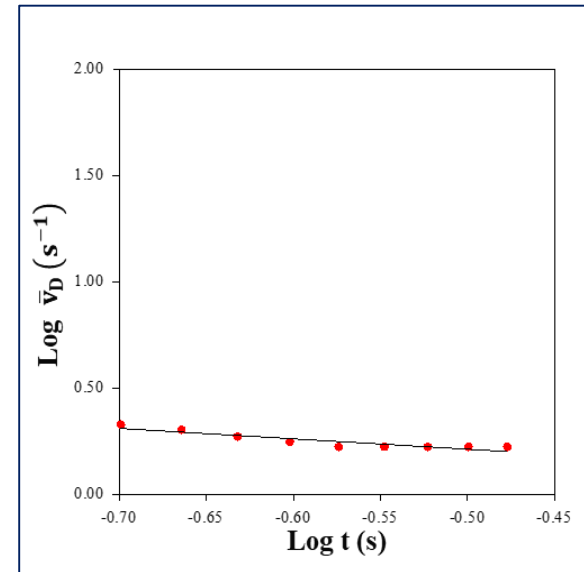
Figure 4-8. Imbibition kinetics for $0° < \theta^* < 60°$ powder bed at $\mu = 1.00$ m Pa s

70
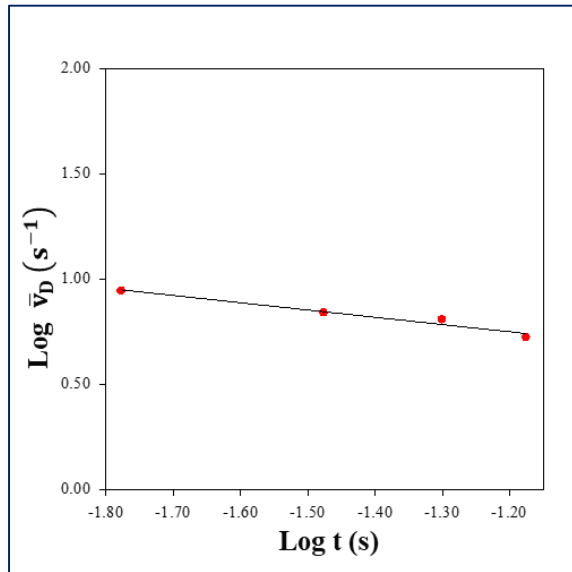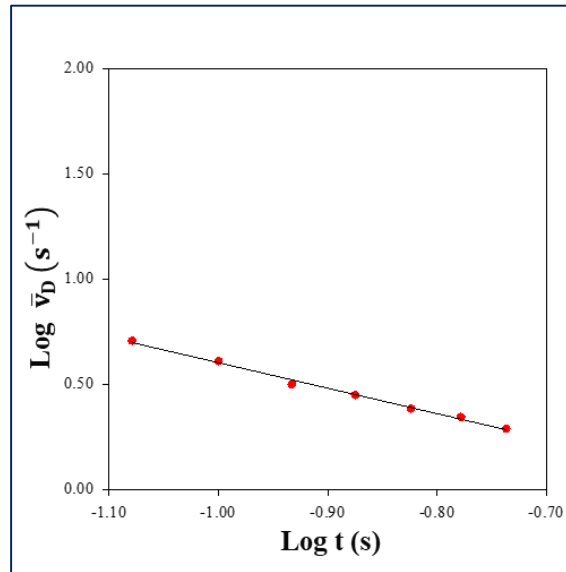
Region 1	Region 2	Region 3
$Y = -0.35x + 0.33$	$Y = -1.21x - 0.61$	$Y = -0.56x - 0.11$
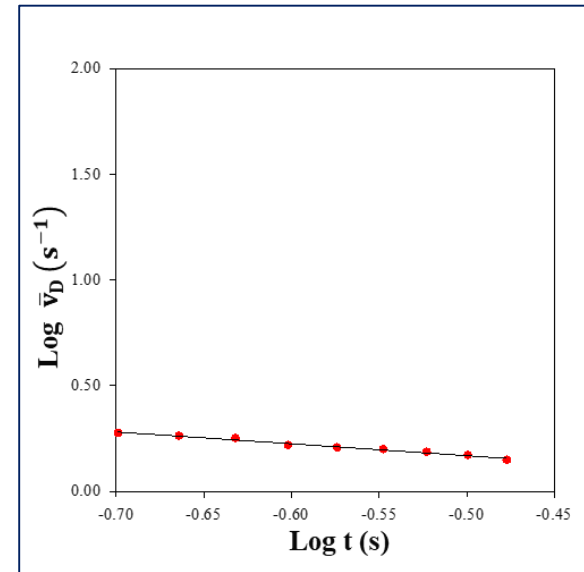
Figure 4-9. Imbibition kinetics for $60° < \theta^* < 140°$ powder bed at $\mu = 1.00$ m Pa s

Table 4-4. A summary of the characteristic power law exponents for different μ and $0° < \theta^* < 60°$ powder beds

ϕ	$\bar{v}_D$ Regimes	$\bar{v}_D$ Power Law μ: 1.00 m Pa s	$\bar{v}_D$ Power Law μ: 2.30 m Pa s	$\bar{v}_D$ Power Law μ: 3.20 m Pa s	$\bar{v}_D$ Power Law μ: 9.40 m Pa s
1.00	Regime 1	$t^{-1.173}$	$t^{-1.149}$	$t^{-0.901}$	$t^{-0.857}$
	Regime 2	$t^{-1.088}$	$t^{-0.679}$	$t^{-0.480}$	$t^{-0.121}$
	Regime 3	$t^{-0.488}$	$t^{-0.422}$	$t^{-0.459}$	$t^{-0.035}$
0.93	Regime 1	$t^{-1.098}$	$t^{-0.837}$	$t^{-0.761}$	$t^{-0.680}$
	Regime 2	$t^{-1.018}$	$t^{-0.642}$	$t^{-0.445}$	$t^{-0.138}$
	Regime 3	$t^{-0.506}$	$t^{-0.398}$	$t^{-0.408}$	$t^{-0.028}$

It was observed that for $0° < \theta^* < 60°$ and low viscosity the $\bar{v}_D$ is initially driven by capillary forces as it rapidly decreases with time in the t_{CDA} phase. In this capillarity driven regime, the high values of the power law $t^{-1.173}$ ($\phi = 1.00$) and $t^{-1.098}$ ($\phi = 0.93$) at low μ indicate that the d_v imbibition is occurring at a faster rate initially. This higher rate for low θ_m^* is attributed to the formation of small capillaries between pores which enhance the liquid droplet flow [110].

Following the initial capillary regime, the d_v imbibition rate slowed, and an intermediate regime was observed. This intermediate regime obeys the power law of $t^{-1.088}$ ($\phi = 1.00$) and $t^{-1.018}$ ($\phi = 0.93$). The reduced power laws suggest the existence of an intermediate viscous forces driven regime where the $\bar{v}_D$ slows down as d_v imbibition proceeds. In this regime, the dynamics of the d_v imbibition rate are slowed down due to liquid saturation of the pores. It is well known that when in contact with liquid, lactose particles undergo partial dissolution, increasing, the 'effective μ' of the liquid.

This phenomenon was observed to happen in < 0.15 s which means that it is important to consider dissolution of lactose during the initial regime of liquid droplet imbibition. The effective μ will increase with time at magnitudes of 0.30 - 2.0 depending on the binder type and thus act to retard the d_v imbibition rate, (see Table 4-4). The intermediate viscous forces driven regime continues to dominate the final regime 3 of the liquid drop imbibition process at low viscosity and θ^*.

Table 4-5. A summary of the characteristic power law exponents for different μ and $60° < \theta^* < 140°$ powder beds

ϕ	$\bar{v}_D$ Regimes	$\bar{v}_D$ Power Law μ: 1.00 m Pa s	$\bar{v}_D$ Power Law μ: 2.30 m Pa s	$\bar{v}_D$ Power Law μ: 3.20 m Pa s	$\bar{v}_D$ Power Law μ: 9.40 m Pa s
0.87	Regime 1	$t^{-0.853}$	$t^{-0.682}$	$t^{-0.562}$	$t^{-0.264}$
	Regime 2	$t^{-0.732}$	$t^{-0.614}$	$t^{-0.580}$	$t^{-0.280}$
	Regime 3	$t^{-0.662}$	$t^{-0.568}$	$t^{-0.413}$	$t^{-0.232}$
0.74	Regime 1	$t^{-0.612}$	$t^{-0.537}$	$t^{-0.561}$	$t^{-0.180}$
	Regime 2	$t^{-0.558}$	$t^{-0.442}$	$t^{-0.445}$	$t^{-0.138}$
	Regime 3	$t^{-0.406}$	$t^{-0.398}$	$t^{-0.508}$	$t^{-0.088}$

For liquid droplet imbibition into $60° < \theta^* < 140°$ powder beds at low viscosity, the initial $\bar{v}_D$ is occurring at a slower rate due to imbibition of liquid movement through site percolation, increasing the d_v imbibition. The slower rate is indicated by the lower values of the power laws $t^{-0.853}$ ($\phi = 0.87$) and $t^{-0.612}$ ($\phi = 0.74$) at low viscosity and high θ^*. These results suggest that $\bar{v}_D$ is initially in a regime where the interfacial effects play a dominant role. Thus, imbibition for low μ and high θ_m^*, is preceded by an interfacial driven regime rather than the conventional capillary forces driven regime when θ^* is increased.

This means that the liquid droplet will remain on the powder bed surface until there are enough driving forces for the d_v imbibition to proceed via site percolation, confirming the results reported previously. The $\bar{v}_D$ decreases further in the subsequent regimes, revealing, a coupling between the interfacial effects and capillary forces, which compete for dominance until the d_v imbibition process of the liquid droplet comes to completion at low viscosity. However, in all cases the extent of the increase in $\bar{v}_D$ was retarded by viscous drag in accordance with Darcy law relationship μ^{-1}, (see Tables 4-4 - 4.5) resulting in a decrease in liquid droplet horizontal spreading.

It is observed that the power-law scaling does not follow the $t^{0.5}$ growth as expected by the modified Darcy rate law due to a competition between viscous and capillary forces and interfacial effects during d_v imbibition rate process. Thus, there will be a transition from Darcy

law to t^n, where n is < 0.5. This in fact seems to be a crossover to a slower exponential d_v imbibition law because of unbalanced competition between liquid droplet hydrodynamics.

In contrast, Grzelakowski et al. [109], found the $\bar{v}_D$ to increase as a function of time with slight deviations from the expected $t^{0.5}$ growth . This increase in $\bar{v}_D$ was attributed to the porous structure of the membranes (pore diameter > 90 nm) which were either small interconnected pores or straight large pores. The high porosity channels make the increase of the ratio d_h/d_0 to be much smaller than the increase in $(V_0 - V(t))/V_0$ which causes the liquid droplet to spread less. However, the high porosity promotes capillary suction which drives the $\bar{v}_D$ to increase with time. In powder beds, the bed porosity is much smaller compared to the membrane porosity which causes the ratio of d_h/d_0 to increase significantly in comparison to the $(V_0 - V(t))/V_0$ resulting in a decrease of $\bar{v}_D$ with time. Since Darcy's law is not obeyed with hydrophilic/hydrophobic powder beds, it is concluded that further investigations are needed to propose suitable d_v imbibition rate laws for these powder beds.

4.6 Horizontal Spreading Dynamics Model

A physical description of the d_h spreading process is essential for the determination of the wetting behavior of the liquid droplet, to allow a predictive approach to the spreading kinetics. In Chapter 2, theoretical models that describe the d_h spreading process and their limitations of applicability were discussed.

Here, the applicability of the Harth & Schubert [37] d_h spreading model is reviewed as it has not yet been validated for powder beds. The model predicts the behavior of the liquid droplet radius (r) as a function of time on partially wetting solids. This model considers the balance of forces (gravitational, capillary, viscous) at the γ_{SL} interface based on spherical cap approximation. The model also assumes that the liquid droplet does not penetrate into the surface and thus the liquid droplet volume is constant at a specific time:

Partial wetting case $(\gamma_{SV} = \gamma_{SL} (\cos \theta^* = 0))$

$$r(t) = r_e \left[1 - \exp\left(-\left(\frac{2\gamma_{LV}}{r_e^{12}} + \frac{pg}{9r_e^{10}} \right) \frac{24\text{\O}V_0^4(t + t_0)}{\pi^2\mu} \right) \right]^{\frac{1}{6}}$$

Equation 4-10

Equation 4-10 is simplified, assuming that gravity is negligible as the work considers liquid droplet sizes smaller than the capillary length (Equation 2-17) [12]:

$$r(t) = r_e \left[1 - \exp\left(-\left(\frac{2\gamma_{LV}}{r_e^{12}} \right) \frac{24\text{\O}V_0^4(t + t_0)}{\pi^2\mu} \right) \right]^{1/6}$$

Equation 4-11

Let,

$$x = \left(\frac{2\gamma_{LV}}{r_e^{12}} \right) \frac{24\text{\O}V_0^4(t + t_0)}{\pi^2\mu}$$

Equation 4-12

Thus, Equation 4-11 becomes:

$$r(t) = r_e[1 - \exp(-x)]^{1/6}$$

Equation 4-13

Maclaurin series expansion of $\exp(-x)$ gives:

$$\exp(-x) = 1 - x + \frac{x^2}{2!} - \frac{x^3}{3!} + \cdots$$

Equation 4-14

Substituting Equation 4-14 into Equation 4-13 gives:

$$r(t) = r_e \left[1 - \left(1 - x + \frac{x^2}{2!} - \frac{x^3}{3!} + \cdots \right) \right]^{1/6}$$

If x is very small, higher order terms of the series expansion can be neglected, so that Equation 4-15 becomes:

$$r(t) \simeq r_e [1 - (1 - x)]^{1/6}$$

Substituting Equation 4-12 back into Equation 4-16 gives:

$$r^6(t) \simeq r_e{}^6 \left(\frac{2\gamma_{LV}}{r_e^{12}} \frac{24 \emptyset V_0^4 (t + t_0)}{\pi^2 \mu} \right)$$

In Equation. 4-17, we can take $r_e{}^3$ to be proportional to the volume of a sphere, such that:

$$r^6(t) \propto \left(\frac{2\gamma_{LV}}{V^2} \frac{24 \emptyset V_0^4 (t + t_0)}{\pi^2 \mu} \right)$$

Since $\emptyset$ and π are known constants, Equation 4-18 can be simplified as follows:

$$r^6(t) \propto \left(\frac{2\gamma_{LV}}{\mu} \right) V_0^2 (t + t_0)$$

Equation 4-19 implies that r^6 is linear with change in $t + t_0$. Assume B to be the constant of proportionality, then Equation 4-19 becomes:

$$r^6(t) = B\left(\frac{2\gamma_{LV}}{\mu}\right)V_0^2(t + t_0)$$

When this is the case, then slope is $B\frac{2\gamma_{LV}}{\mu}V_0^2$.

Equation 4-20 implies that r^6 scales linearly with change in $t + t_0$. When this is the case, then the slope $\propto \left(\frac{2\gamma_{LV}}{\mu}\right)V_0^2$. The slope of the line represents approximately constant d_h spreading characteristics.

Figures 4-10 - 4-12 show the relationship between the experimentally determined r^6 vs $\left(\frac{2\gamma_{LV}}{\mu}\right)V_0^2(t + t_0)$. In these figures, each symbol and colour represents different liquid droplet volumes and μ respectively. The solid lines represent linear regression (black solid lines), 95 % confidence interval bands (long blue dashed lines) and 95 % prediction bands (solid red lines) obtained by fitting the experimental data. Table 4-6 shows the linear regression results for the r^6 vs $\left(\frac{2\gamma_{LV}}{\mu}\right)V_0^2(t + t_0)$ relationship where the intercept was constrained to the origin.
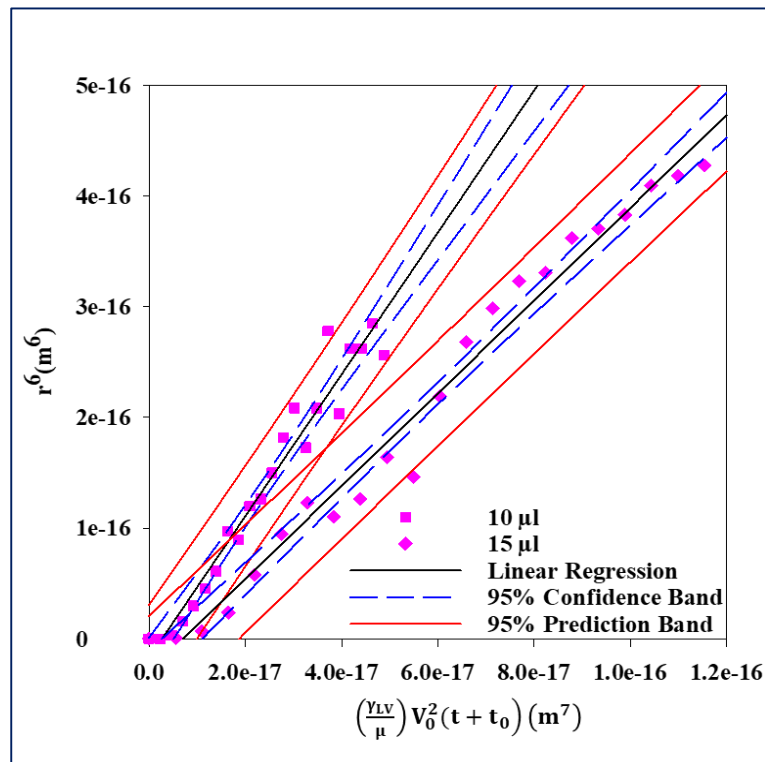
Figure 4-10. The initial d_h spreading behavior for $\phi = 1.00$, $\mu = 3.67$ m Pa s fitted to Equation 4-20.
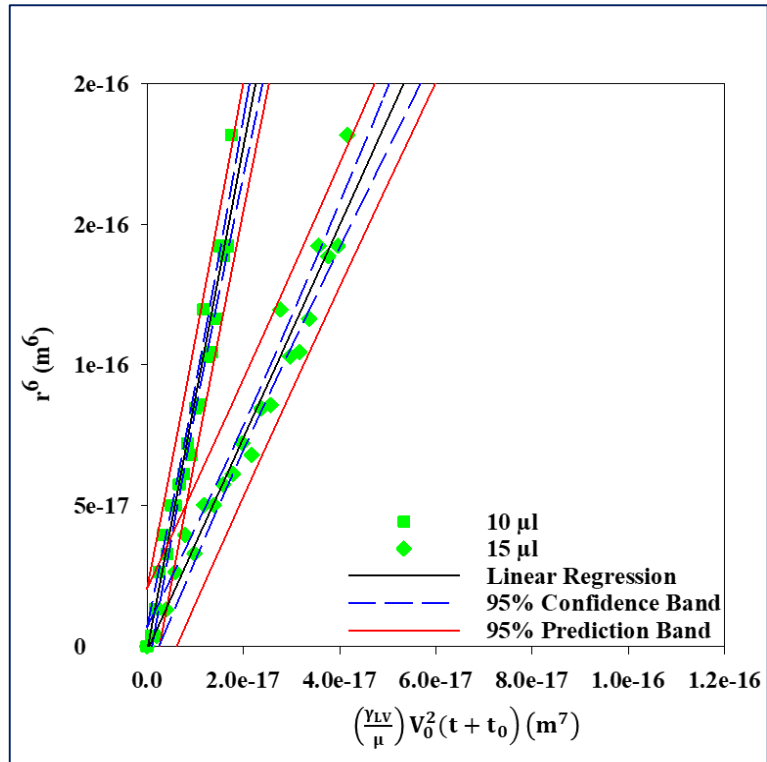
Figure 4-11. The initial d_h spreading behavior for $\phi = 1.00$, $\mu = 9.40$ m Pa s fitted to Equation 4-20.
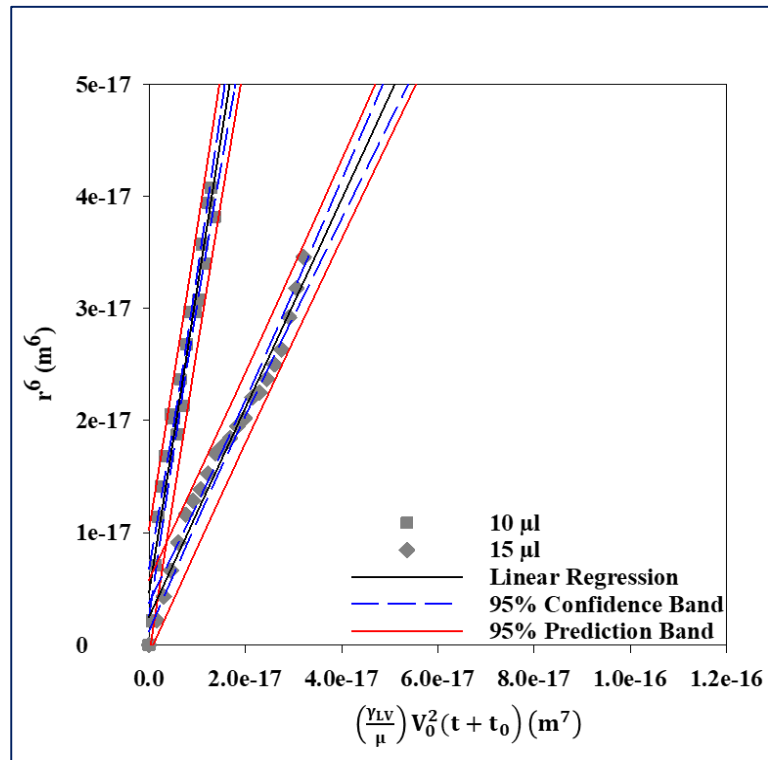
Figure 4-12. The initial d_h spreading behavior for $\phi = 1.00$, $\mu = 13.17$ m Pa s fitted to Equation 4-20.

Table 4-6. Linear regression results for the effect of μ and V_0 on the d_h spreading behavior of $\phi = 1.00$

μ (m Pa s)	Volume (μl)	Slope	Std. Error on slope	Regression coefficient R^2
3.67	10	6.41	2.13e^{-17}	1.00
	15	4.19	2.23e^{-17}	1.00
9.40	10	8.95	9.81e^{-18}	1.00
	15	3.79	9.81e^{-18}	1.00
13.17	10	2.71	2.48e^{-18}	1.00
	15	0.93	1.47e^{-18}	1.00

There is a linear relationship between r^6 vs $\left(\frac{2\gamma_{LV}}{\mu}\right) V_0^2 (t + t_0)$, (see Figures 4-10 - 4-12). However, the experimental data do not coincide to a constant slope when the liquid droplet volume increases (see Table 4-6). This discrepancy is because Equation 4-20 assumes that the liquid droplet volume is constant at a specific time during the d_h spreading process.

The implication of Equation 4-20 is that r^6 is expected to decrease as μ increases, as increasing viscous forces reduces the capillary driving force for liquid flow into the capillaries and slows the liquid velocity. This behavior is reflected in Figures 4-10 - 4-12. Thus, the model is very good at predicting the effects of μ, however results presented illustrate that Equation 4-20 doesn't describe the effects of changing the liquid droplet volume on the liquid droplet horizontal spreading behavior very well.

In practice on powder beds, when a liquid droplet comes into contact the powder bed it may spread and penetrate to some extent as shown in Tables 4-1 and 4-2. This suggests that the liquid droplet remaining on the powder bed decreases with time. According to Hapgood et al. [63], based on the key assumption that the liquid droplet will advance into the powder bed with time i.e. volume changes with time, the liquid droplet volume on a powder bed scales as:

$$t \propto V_0^{\frac{2}{3}}$$

Equation 4-21

Substituting of Equation 4-21 into 4-20 gives:

$$r^6(t) \propto \left(\frac{2\gamma_{LV}}{\mu}\right) V_0^{\frac{2}{3}}(t + t_0)$$

Figures 4-13 - 4-15 compares the predictions of Equation 4-22. The linear regression results for the r^6 vs $\left(\frac{2\gamma_{LV}}{\mu}\right) V_0^{\frac{2}{3}}$ relationship are shown in Table 4-7. The implication of Equation 4-22 is that the experimental data should coincide to a constant slope independent of μ and V_0.
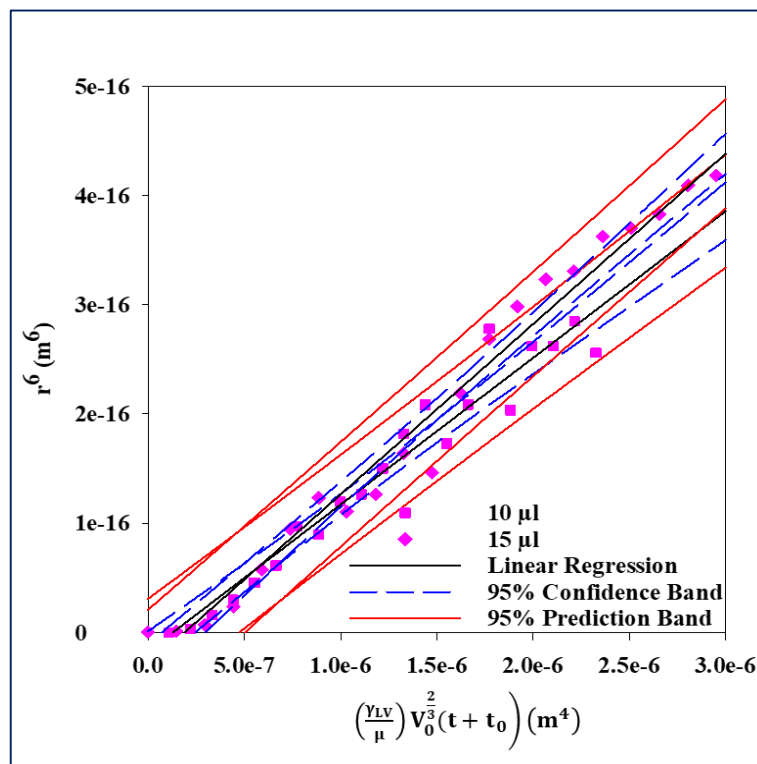
Figure 4-13. The initial d_h spreading behavior for $\phi = 1.00$, $\mu = 3.67$ m Pa s fitted to Equation 4-22.

80
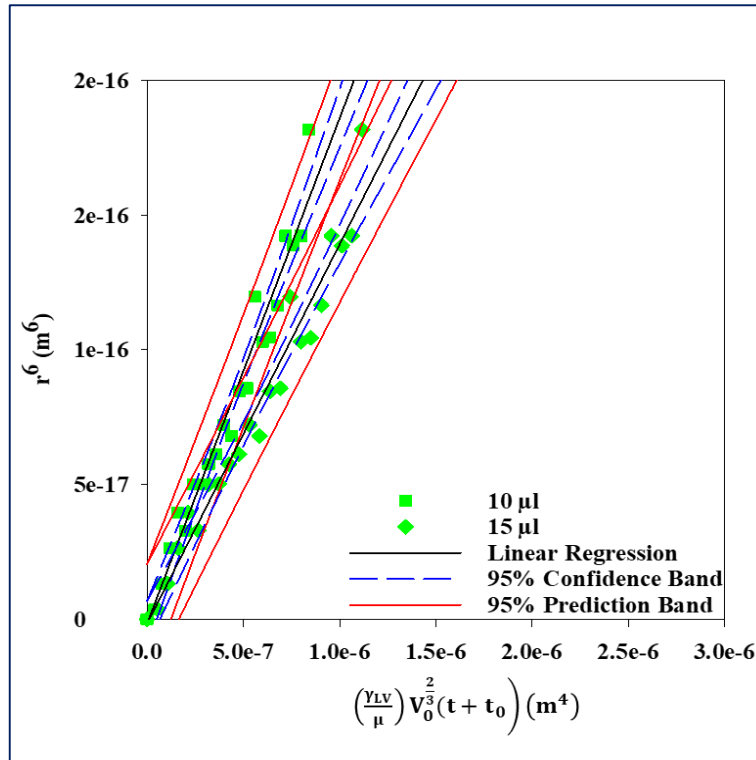
Figure 4-14. The initial d_h spreading behavior for $\phi = 1.00$, $\mu = 9.40$ m Pa s fitted to Equation 4-22.
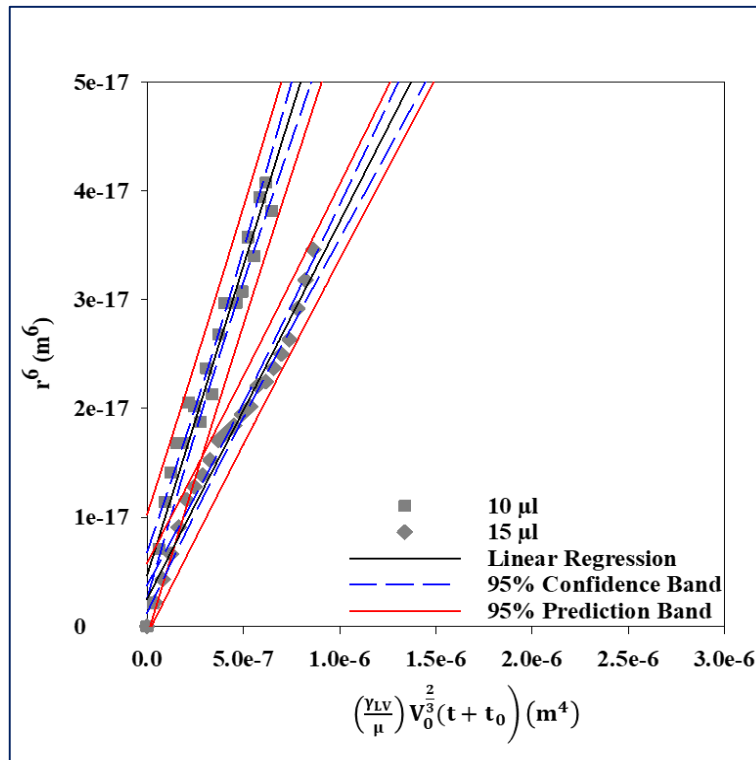
Figure 4-15. Partial wetting case: The initial d_h spreading behavior for $\phi = 1.00$, $\mu = 3.67$ m Pa s fitted to Equation 4-22.

81

Table 4-7. Linear regression results for the effect of μ and V_0 on the d_h spreading behavior of $\phi =$ 1.00

μ (m Pa s)	Volume (μl)	Slope	Std. Error on slope	Regression coefficient R^2
3.67	10	$1.34e^{-10}$	$2.13e^{-17}$	1.00
	15	$1.56e^{-10}$	$2.23e^{-17}$	1.00
9.40	10	$1.88e^{-10}$	$9.81e^{-18}$	1.00
	15	$1.41e^{-10}$	$9.81e^{-18}$	1.00
13.17	10	$5.69e^{-11}$	$2.48e^{-18}$	1.00
	15	$3.47e^{-11}$	$1.47e^{-18}$	1.00

As can be seen, changing the liquid droplet volume scaling law had a significant effect on the model predictions for the d_h spreading. This effect is shown in Figures 4-13 – 4-15 where the 95 % confidence interval bands and 95 % prediction bands overlap especially at low μ were complete overlapping is observed. This resulted in most of the experimental data having similar slope independent of μ and V_0. These results show that improved model Equation 4-22 is successful in predicting d_h spreading behavior on powder beds. However, further research on the implication of Equation 4-22 on hydrophobic powder beds is required.

4.7 Conclusions

An experimental study has been undertaken into the dynamics of competing d_h spreading vs d_v imbibition mechanisms of a single liquid droplet into powder beds. The competing spreading mechanisms complex interplay with θ^* and μ has been investigated and linked to existing theories on these mechanisms.

The main observations and conclusions from Chapter 4 are highlighted below:

- Results show that the measured maximum d_h spreading diameter is less than the diameter of the resultant nuclei. This indicates that the d_h spreading of the liquid droplet continues to spread after complete imbibition in a late-diffusive intra-spreading process. This process refers to liquid movement driven by capillary forces in the powder beds and showed a higher degree of dependency on the liquid binder viscosity.

- The d_v imbibition length was found to be dependent on the interfacial tension between the solid and the liquid droplet. This transition in the liquid spreading and imbibition behaviour is explained based on the transportation of a liquid droplet occurring increasingly via site percolation theory with increase in powder bed hydrophobicity.

- The rate of d_v imbibition was determined from the modified Darcy law in which spreading of a liquid droplet on a powder bed was found to follow a power law as a function of time. The exponent of this law was found to deviate from the expected Darcy law $t^{0.5}$ due to a competition between capillary and viscous forces and interfacial effects.

- Experimental validation of Harth & Schubert [37] model on predicting the d_h spreading, found the model to account well for the changes in μ and was not successful in predicting changes of liquid droplet volume as it assumes that the liquid droplet volume on the powder bed remains constant during spreading. However, when Harth & Schubert model's was modified with the Hapgood et al. [60] scaling for liquid droplet volume ($t \propto V_0^{\frac{2}{3}}$), the improved model was much more successful in describing the d_h spreading behavior.

These results, translated into real granulation behavior, imply that viscous binders will imbibe slowly into the powder bed leaving a layer of liquid available on the surface. It was speculated that the layer of liquid on the surface will result in coalescence being the dominant granulation rate process for granule growth [33]. However, it is argued that a layer of liquid remaining on the surface due to slow imbibition kinetics will lead to layering mechanism resulting in particle segregation, impacting content, uniformity and appearance of final product. This means that further agitation will be required to redistribute the liquid binder to enable successful particle adhesion and improve homogeneity. This will be examined in later in this thesis.

5 THE SIGNIFICANCE OF WETTABILITY BEHAVIOUR OF MIXTURES IN RELATION TO SURFACE COVERAGE

5.1 Introduction

The wetting process involved when a liquid droplet comes into contact with a mixture of particles is a complex phenomenon which is often understood by reference to Cassie-Baxter theory [10]. However, various authors have applied the Cassie-Baxter theory for the prediction of contact angles on two-component mixtures without success [3,14–17]. It is hypothesised that the main difficulty in applying the Cassie-Baxter theory to mixtures is that if the particles differ in size, it is possible for the small particles to coat the large particles, so reducing the available surface fraction of the large particles. This leads to the view that bulk volume fractions are not good estimates of surface fractions of the components within the mixture. As a consequence it is argued that Cassie-Baxter theory does not reflect the presence of large particles until their concentration represent a critical surface coverage volume fraction.

Aa simple geometrical model that relates the critical surface coverage volume fraction to the sauter mean particle size of the components is presented. In turn, this means that the wetting behaviour can be determined from the bulk volume fractions and calculated critical surface coverage volume fraction, by means of a simple arithmetic model. It is shown that the simple model describes the five two-components systems reported here and a further four systems reported in literature, irrespective of whether the larger or small particles are hydrophobic/hydrophilic. With this model, it is possible to predict the wetting behaviour of mixtures of particles that coat each other using very simple characterisation methods, so reducing the development time in the creation of formulations in the pharmaceutical industry.

5.2 The debate on Cassie-Baxter Theory

the applicability of the Cassie-Baxter theory in the prediction of liquid contact angles on two-component mixtures consisting of hydrophilic/hydrophobic particles is reviewed [11]. Cassie-Baxter theory was derived on the basis that contact angles are determined by the interactions within the interfacial contact area of the liquid and solid surface. To validate their theory, Cassie-Baxter studied systems in which the components were not free to rearrange and so the surface fraction of each component was fixed and simple to determine. However, several

authors have questioned the validity of the Cassie-Baxter theory and suggested that the three-phase contact line alone and not the interfacial contact area is important in determining the contact angle behavior [18,19]. This result was explained to be due to the different behavior of solid molecules in comparison to liquid molecules. At the three-phase contact line, solid molecules are not mobile and cannot contact to obey area minimization when a liquid droplet is placed on them. Put simply, the laws of liquids cannot be directly applied to solids. The aim of our paper is to highlight the misconceptions and restrictions of Cassie-Baxter theory in predicting contact angles on two-component particulate mixtures. Consequentially, a new theory is put forward which is supported by detailed experimental investigations that allows the prediction of contact angles on two-component particulate mixtures.

5.3 Existing Theories

When a liquid droplet comes into contact with the powder bed surface, the liquid droplet wets the powder bed surface. This wetting phenomenon is determined by the interactions between the molecules of the two phases coming into contact, forming a three-phase contact line, where the liquid, powder bed surface and vapour co-exist. The three-phase contact line will continue to advance to an equilibrium contact angle (θ_E) in which the liquid droplet takes the shape that minimizes the total free energy of the system, (see Figure 2-1).
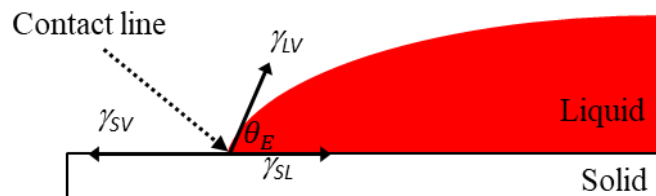
Figure 5-1. Cross sectional contact angle profile of a liquid droplet on a solid surface at a three phase contact line.

where γ_{SL}, γ_{SV} and γ_{LV} are the three-interfacial tensions: solid-liquid, solid-vapour and liquid-vapour respectively.

A well-known relation for θ_E was developed by Young [8] assuming an idealized smooth and homogeneous solid surface and that the liquid droplet does not spread further after reaching its equilibrium contact line radius. A liquid is said to wet a surface $\gamma_{SV} - \gamma_{SL} \geq \gamma_{LV}$ ($\cos\theta \leq 1, \theta = 0$) and non-wetting if $\gamma_{SV} < \gamma_{SL}$ ($\cos\theta$ is negative). However, in reality solid surfaces are not ideal, particularly pharmaceutical powders where there are several factors that affect the measured apparent contact angle (θ^*) such as contact line surface

heterogeneities, chemical composition of the liquid and solid surface [9–12].

Wenzel [9] first related the θ^* to solid surface heterogeneities (roughness) assuming that the liquid droplet fills the grooves of a rough solid surface completely. Wenzel's theory suggests that on a hydrophilic solid surface, surface roughness enhances its wetting behaviour since there is a greater net energy decrease to induce spreading. In hydrophobic powder beds, the non-wetting behaviour of a solid surface is exaggerated with surface roughness. However, Wenzel's theory is valid for one-component solid systems.

In the pharmaceutical industry, solid systems are however frequently mixtures. For two-component mixtures Cassie-Baxter related the θ^* with the wetted fraction of surface area of a solid based on the assumption that the solid surface is smooth and consists of a grid of cylinders using the following expression [10]:

$$\cos \theta^* = f_1 \cos \theta_1^* + f_2 \cos \theta_2^*$$

$$f_1 + f_2 = 1$$

Equation 5-1

where θ^* is the apparent equilibrium contact angle, f_1 and f_2 are the area fractions of component 1 and 2 with apparent contact angles of θ_1^* and θ_2^* respectively.

There are a number of limitations with the Cassie-Baxter approach: a) in practise real solid surfaces do not consist of cylindrical particles and have complex pore structures in which the liquid droplet is able to spread on the solid surface and fill the pores in any direction and b) Cassie and Baxter studied systems in which the components were not free to rearrange and so the surface fraction of each component was fixed and simple to determine. In seeking to apply their result to mixtures of particles it has to be assumed that the surface fraction of each component is equal to the known volume fraction; a situation that arises naturally if particles can rearrange in the surface of the mixture i.e. in 2D, but not vertically i.e. in 3D. Then Equation 3 is rewritten as:

$$\cos \theta^* = (\phi) \cos \theta_1^* + (1 - \phi) \cos \theta_2^*$$

$$1 - \phi = \frac{\cos \theta^* - \cos \theta_1^*}{\cos \theta_2^* - \cos \theta_1^*} = \overline{\cos \theta^*}$$

where ϕ is the volume fraction of particles and $\overline{\cos \theta^*}$ is the normalised contact angle.
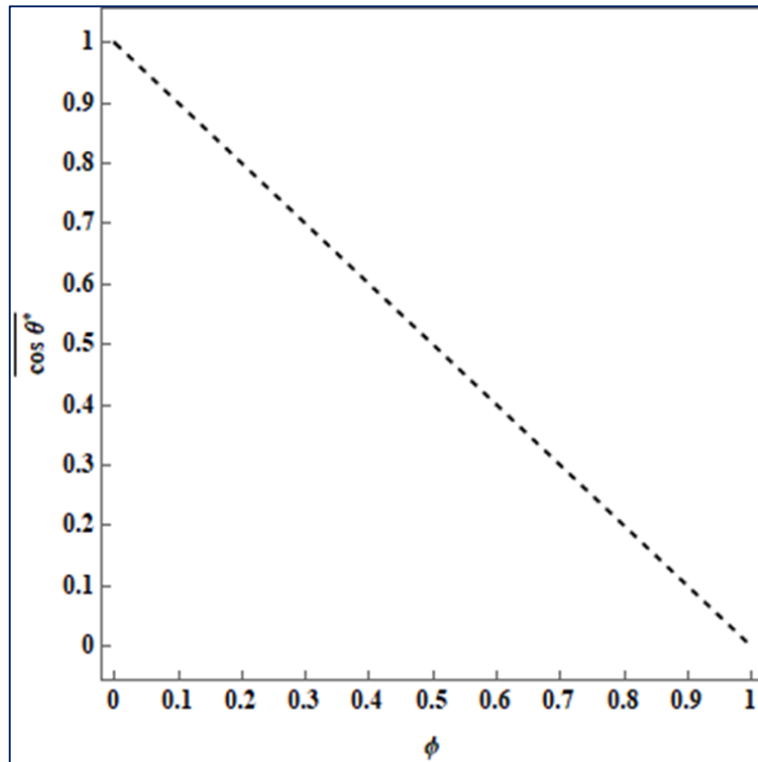
Figure 5-2. Relationship between the normalized contact angle and the volume fraction of particles of type 1 according to Cassie-Baxter, from Equation 5-3

Figure 5-2 shows a typical representation of the normalized contact angle $(\overline{\cos \theta^*})$ behaviour which is predicted using Equation 5-3. The implication of Equation 3 is that a plot of $\overline{\cos \theta^*}$ versus the volume fraction (ϕ) of the particles in the powder mixture, gives an inverse linear relationship (see Figure 5-2). This shows that as ϕ increases there is a corresponding reduction in the value of $\overline{\cos \theta^*}$. However, it is hypothesised that there will be a non-linear relationship between $\overline{\cos \theta^*}$ versus ϕ if the particles differ in size, as it is possible for the small particles to coat the large particles sufficiently, such that there is a critical surface coverage volume fraction at which full coverage of larger particle by the small is achieved. Thus, it is envisaged that the contact angle behaviour varies unpredictably until a marked change at the

critical surface coverage volume fraction is reached (ϕ_c). In what follows, a simple surface coverage wetting model is proposed that predicts a non-linear relationship between $\overline{\cos \theta^*}$ and ϕ of the components within a particulate mixture.

5.4 Revised Theory

A model is propoped that considers a two-component powder system consisting of uniformly distributed particles of differing chemical composition, using the following assumptions to complete the derivation:

1. Particles are treated as spheres.
2. There is no air present.
3. The solid surface is smooth.
4. The surface fraction of each component is equal to a known volume fraction.

A unit volume of a mixture in which the volume fraction of large particles is ϕ is considered. Assuming that the total volume of the mixture $1 \ cm^3$, it then follows then that:

Volume of Lactose

$$v_1 = \phi_1 = \ \phi$$

Equation 5-4

Volume of Magnesium Stearate

$$v_2 = \phi_2 = 1 - \ \phi$$

Equation 5-5

where v_1 is the volume of large particles and v_2 is the volume of small particles.

From this, the surface area, s_1 of the large particles is defined as:

$$s_1 = \frac{6\phi}{d_1}$$

Equation 5-6

The projected area of small particles, p_2 is given by:

$$p_2 = \frac{3(1 - \phi)}{2d_2}$$

If small particles cover the large ones surface coverage of larger particles by small particles is related to the s_1 and p_2 by:

$$f_{sc} = \frac{\text{projected area}}{\text{surface area}}$$

where f_{SC} is fractional surface coverage of larger particles by the small

Substituting Equation 8 and 9 gives:

$$f_{SC} = \frac{1}{4} \frac{(1 - \phi)}{\phi} \frac{d_1}{d_2}$$

If Equation 5-9 is equated to $f_{SC} = 1$, $\phi = \phi_C$ then solving for ϕ_C, yields the critical value fraction at which larger particles are completely covered by the small particles :

Rearrangement gives:

$$\phi_C = \frac{1}{\frac{4d_2}{d_1} + 1}$$

The value of d_1 and d_2 can be easily determined allowing ϕ_C to be predicted without conducting extensive analysis.

$$f_{SC} = \frac{1 - \phi}{1 - \phi_C} \frac{\phi_C}{\phi} \qquad \text{if } \phi \geq \phi_C$$

In the style of Cassie-Baxter the following is expected:

$$\cos \theta^* = (1-f)\cos \theta_1^* + f\cos \theta_2^*$$

$$\overline{\cos \theta^*} = f = \min(f_{SC},1)$$

$$\overline{\cos \theta^*} = f = \min(\frac{1-\phi}{1-\phi_C}\frac{\phi_C}{\phi},1)$$

If $\phi > \phi_C$ then $f_2 = f_{SC}, f_1 = 1 - f_{SC}$

If $\phi \leq \phi_C$ then $f_2 = 0, f_1 = 1$

Figure 5-3 shows a typical representation of the $\overline{\cos \theta^*}$ behaviour of mixtures which is predicted using Equation 13. As seen from Figure 5-3 that Equation 5-11 predicts a non-linear relationship between the $\overline{\cos \theta^*}$ and ϕ. It is argued that this non-linear relationship in $\overline{\cos \theta^*}$ behavior arises because of small particles coating the large particles sufficiently at a critical-volume fraction (ϕ_c) at which complete surface coverage of the larger particles by the small is achieved.
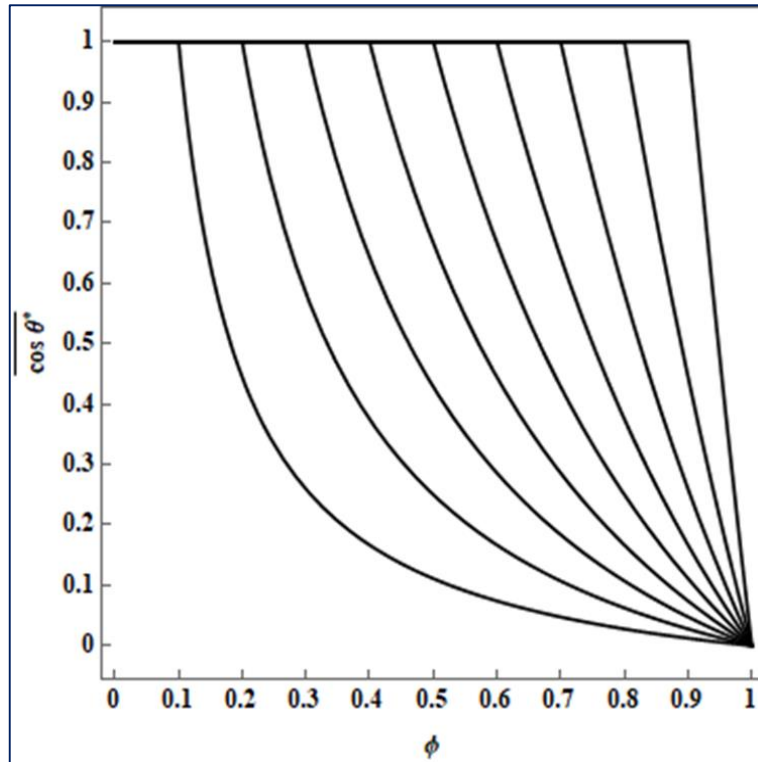
Figure 5-3. The normalized contact angle profiles of mixtures predicted from Equation 5- 11 with the critical surface coverage volume fraction in the range of 0.1 to 0.9, in increments of 0.1.

For a given mixture, if ϕ of large particles is greater than ϕ_c, the contact angle behavior changes unpredictably as there is no complete surface coverage of larger particles by the small (see Figure 5-3). However, if ϕ of large particles is less than or equal to ϕ_c then complete surface coverage of the larger particles by the small is achieved, so reducing the available surface fraction of the large particles. This changes the relationship between $\overline{\cos \theta^*}$ and ϕ to non-linear.

Conceptually, Equation 5-11 describes a simple geometrical model that relates the available surface fraction to the underlying bulk volume fractions of the components. This geometrical model depends only on the ratio of particle sizes, which in turn can be described by a ϕ_C at which complete surface coverage of the larger particles by the small is achieved. This approach allows that particles rearrange in 3D, because upon mixing small particles coat larger particles which is in contrast to Cassie-Baxter theory that assumes that particles rearrange in 2D i.e. on the surface. Here a series of experiments to test existing Cassie-Baxter theory and proposed surface coverage wetting theory for predicting contact angle behaviour of particulate mixtures,

with the objective of introducing a new contention relating surface coverage to wetting behaviour is discussed.

5.5 Experimental Design

Single liquid droplet experiments were conducted to measure the θ^* on the powder bed surface. The powder bed surface was comprised of a wide range of hydrophilic and hydrophobic particles given in Table 5-1. Information on the particle size analysis and preparation of the two-component hydrophilic and hydrophobic mixtures is described in Chapter 3.1. The liquid binder was comprised of Hypromellose (Pharmacoat) (Shin-Etsu) were three saturated solutions were prepared: 1.0 wt.% (3.67 m Pa s), 2.5 wt.% (6.10 m Pa s), 5.0 wt.% (13.17 m Pa s). Additional liquid binder properties are given in Chapter 3.1.2. Contact angle measurements were made using a sessile drop method described in Chapter 3.2.1. The contact angle values reported here are average of 10 measurements which were taken from different areas of the powder bed surface. Analysis is further extended to experimental data reported in the literature which focuses on two-component hydrophilic and hydrophobic mixtures.

Table 5-1. Properties of hydrophilic and hydrophobic particles

Primary Particles	True Density[1] (kg/m^3)	Sauter mean diameter, $d_{3,2}$ (µm)	Measured θ^* (°)
Micronized Lactose	1530	1.18	45
Lactose 100M	1150	4.5	20
Lactose 200M	1540	22	22
Lactose 350M	1390	6.0	35
Calcium Carbonate	2700-2900	6.5	98
Ethyl cellulose (sieved)	1130	6.2	90
Magnesium Stearate	1140	2.5	120
Stearic Acid (sieved)	980	2.7	105

[1] True density values were obtained from the suppliers

Table 5-2. Two-component mixtures used

Primary Particles	Particle Description	Mixture	Reference
Lactose 200M	Large Hydrophilic/	M-1	
Magnesium Stearate	Small Hydrophobic		
Lactose 200M	Large Hydrophilic/	M-2	
Stearic Acid	Small Hydrophobic		
Micronized Lactose	Small Hydrophilic/	M-3	
Ethyl cellulose	Large Hydrophobic		
Lactose 350M	Small Hydrophilic/	M-4	
Calcium Carbonate	Large Hydrophobic		
Lactose 100M	Small Hydrophilic/	M-5	
Ethyl cellulose	Large Hydrophobic		
Microcrystalline	Large Hydrophilic/	M-6	[15]
Cellulose	Small Hydrophobic		
Phenacetin			
Limestone	Small Hydrophilic/	M-7	[111]
Tea	Large Hydrophobic		
Di-calcium phosphate	Similar size Hydrophilic/	M-8	[14]
dihydrate	Hydrophobic		
Jet milled Aspirin			
Glass Beads	Similar size	M-9	[17]
Glass Beads	Hydrophilic/Hydrophobic		
Salicylic acid			

5.6 Results and Discussion

The results presented here are not analogous to those reported in literature and serve to emphasize the points made in the proposed surface coverage wetting theory. However, the results complement those of other authors who have found the Cassie-Baxter theory to be invalid in predicting contact angle behavior of particulate mixtures.

Initial experiments were conducted to assess the dependence of binder concentration on the contact angle behavior. Figure 5-4 shows the effect of binder concentration on the $\overline{\cos \theta^*}$ vs ϕ profiles for the particulate mixture M1. Here, Cassie-Baxter Equation 3 and surface coverage

wetting model Equation 5-11 are fitted to the $\overline{\cos \theta^*}$ vs ϕ profiles and the fitted parameters are given in Table 5-3. The surface coverage wetting theory provides for an abrupt transition in $\overline{\cos \theta^*}$.
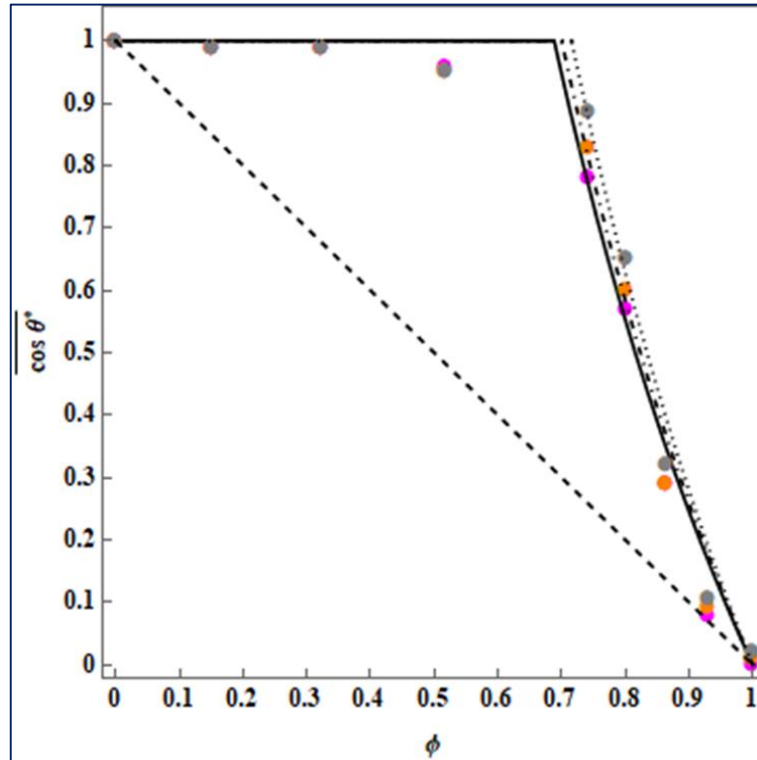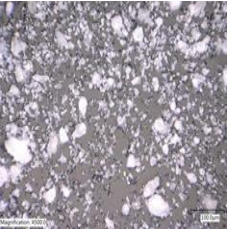
Figure 5-4. Effect of liquid binder concentration on the relationship between $\overline{\cos \theta^*}$ and ϕ for mixture M-1. The symbols correspond to the measured $\overline{\cos \theta^*}$ for ● 1.0 wt.%, ● 2.0 wt.% and ● 5.0 wt.%. The solid, dot-dashed and dashed (tiny) line correspond to the fitted data of Equation 5-11. The dashed line corresponds to the expected Cassie-Baxter relationship.

Table 5-3. The fitted parameters for two-component mixture M-1.

Liquid binder concentration (wt.%)	1.0	2.5	5.0	Global Fitting
ϕ_c	0.688	0.699	0.715	0.702
Standard Error	0.0082	0.0085	0.0077	0.005
t-statistic	83.44	82.92	93.22	140
P-value	4.75×10^{-13}	4.99×10^{-13}	1.96×10^{-13}	5.72×10^{-39}

Table 5-4. Microscopic images of particles

Lactose 200M particles	Magnesium Stearate	Binary Mixture	

It is seen from Figure 5-4 and Table 5-4 that as the ϕ decreases, there is a corresponding increase in the values of $\overline{\cos\theta^*}$ until the ϕ_c is reached were the contact angle behaviour is observed to remain fairly constant. Essentially identical characteristics in $\overline{\cos\theta^*}$ behaviour when the liquid binder concentration is changed were observed, see Figure 4 and Table 4. That is, changing the liquid binder concentration has little effect on the $\overline{\cos\theta^*}$ profile, despite substantial changes in viscosity.

The $\overline{\cos\theta^*}$ behaviour observed is in agreement with the implications from the surface coverage wetting model Equation 5-11, where $\overline{\cos\theta^*}$ behaviour is expected to increase non-linearly as ϕ decreases, as small particles coat the large particles. The non-linear relationship observed between $\overline{\cos\theta^*}$ versus ϕ does not follow the trend expected from the Cassie-Baxter Equation 3. In each case, Equation 14 gives an excellent prediction of $\overline{\cos\theta^*}$ behaviour.

Figure 5-5 shows the effect of primary particle size on the $\overline{\cos\theta^*}$ vs ϕ profiles for the different mixtures. The effect of primary particle size on the $\overline{\cos\theta^*}$ vs ϕ profiles was also investigated on a further four particulate mixture systems reported in literature, (see Figure 5-6). Here, Cassie-Baxter Equation 5-3 and surface coverage wetting model Equation 5-11 are fitted to the $\overline{\cos\theta^*}$ vs ϕ profiles and the fitted parameters are given in Table 5-4.
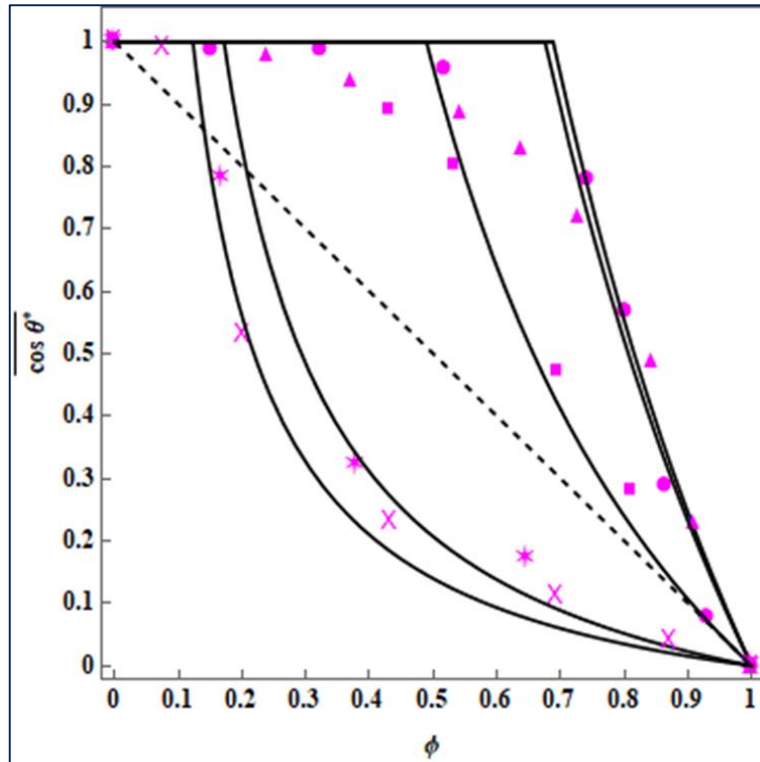
Figure 5-5. Effect of particle size on the relationship between $\overline{\cos \theta^*}$ and ϕ for mixture M-1 (●), M-2 (▲), M-3 (■), M-4 (✶), and M-5 (×) . The solid lines correspond to the fitted data of Equation 13 and the dashed line correspond to the expected Cassie-Baxter relationship.
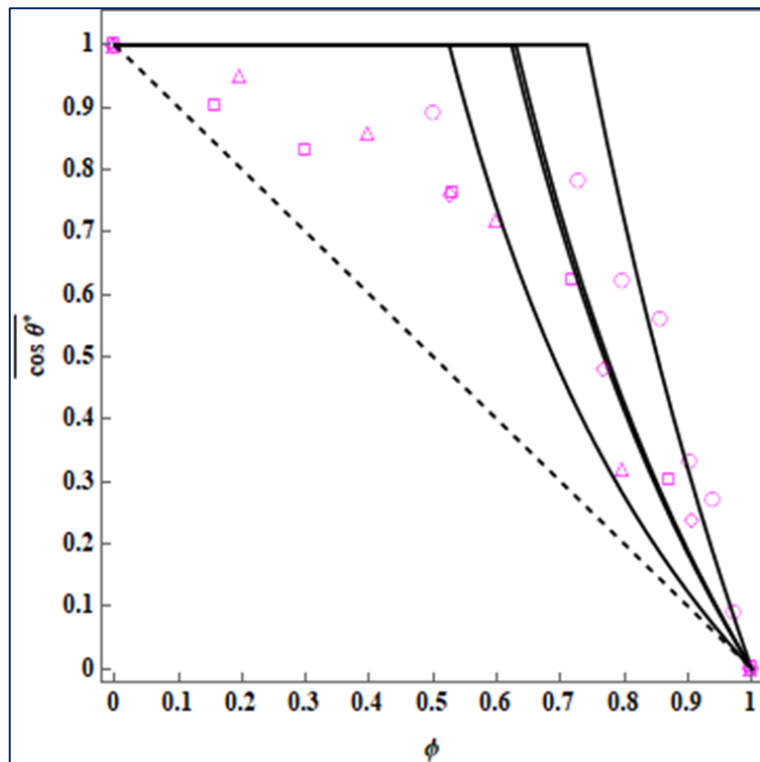
Figure 5-6. Analysis of experimental data reported in literature for mixtures M-6 (○), M-7 (□), M-8 (△), M-9 (◇). The solid lines correspond to the fitted data of Equation 13 and the dashed line correspond to the expected Cassie-Baxter relationship.

Table 5-5. The fitted parameters for various two-component mixtures.

Mixture	ϕ_c	Standard Error	t-statistic	P-value
M-2	0.675	0.02	31.98	9.95×10^{-10}
M-3	0.489	0.02	30.24	7.42×10^{-7}
M-4	0.171	0.05	3.81	$1.89 \times 10\text{-}2$
M-5	0.123	0.006	22.11	5.59×10^{-7}
M-6	0.742	0.02	34.77	5.12×10^{-10}
M-7	0.630	0.06	11.40	3.38×10^{-4}
M-8	0.623	0.044	14.05	8.11×10^{-6}
M-9	0.525	0.022	23.749	2.47×10^{-6}
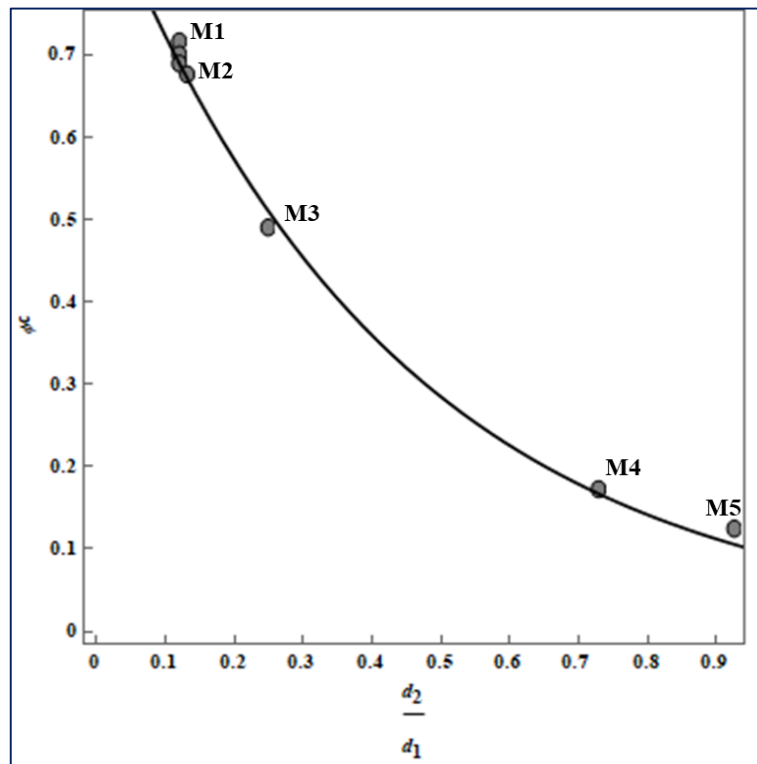
Figure 5-7. Effect of particle size ratio of different mixtures on ϕ_c.

The $\overline{\cos \theta^*}$ behaviours shown in Figure 5-5 - 5-7 are consistent with the predictions from the surface coverage wetting model Equation 13 and inconsistent with the work of Cassie-Baxter Equation 5-3. This convincingly supports the argument that the Cassie-Baxter theory does not reflect the presence of large particles until their concentration represent a critical surface coverage volume fraction. However, the proposed surface coverage wetting model is shown to be very capable in accurately predicting $\overline{\cos \theta^*}$ behaviours for a wide range of

materials. In the pharmaceutical industry, mixtures consist of components with different particle sizes making surface coverage of one constituent over another inevitable, validating the applicability of the surface coverage wetting model to real particulate systems.

In fact, it is believed that this theory is necessary as the Cassie-Baxter equation generally represents a standard mixing equation of the physical chemistry when using two-component powder systems. Our goal is that the proposed relationship based on surface coverage of particles would be useful in describing wetting of powder systems and in understanding the significant deviations from the Cassie-Baxter relationship reported in many publications. Pragmatically, the surface coverage wetting model presented here can of course be further enhanced by unifying it with the works of Cassie-Baxter.

5.7 <u>Conclusions</u>

This chapter considers the dependence of wetting behaviour on the chemical composition of two-component mixtures. Cassie and Baxter studied systems in which the components were not free to rearrange and so the surface fraction of each component was fixed and simple to determine. In seeking to apply their result to mixtures of particles it has to be assumed that the surface fraction of each component is equal to the known volume fraction; a situation that arises naturally if particles can rearrange in the surface of the mixture i.e. in 2D, but not vertically i.e. in 3D. By contrast we propose that if the particles differ in size it is possible for the small particles to coat the large particles, so reducing the available surface fraction of the large particles. In this chapter a simple geometrical model is proposed that relates the available surface fraction to the underlying bulk volume fractions of the components. This geometrical model depends only on the ratio of particle sizes, which in turn can be described by a critical component volume fraction at which full coverage of the larger particles, by the small is achieved. It is observed that with this correction we are able to describe the wetting of two-component hydrophobic/hydrophilic systems using a range of binder solutions.

The main observations and conclusions from the proposed model described in Chapter 5 are highlighted below:

- It was found that changing the binder concentration has little effect, despite substantial changes in viscosity, because the surface energies associated with the liquid change little.

- By contrast, changing the size of the solid phase particles, and particularly the ratio of sizes of the two components, has a marked effect since it is this ratio that determines the extent to which surface coverage of small by large is possible.

Although, many models that predict contact angle behaviour have been presented in literature, the surface coverage wetting model to the author's knowledge represents the first quantitative model that predicts wetting based on surface coverage. The intention in developing this model is to enable a simple approach to theoretical prediction which is expected to be valuable to particle wetting applications pertaining to various industries especially in the pharmaceutical industry where wetting knowledge of solid surfaces is important in formulation development to enable effective design of product that achieves the designed properties.

6 DEVELOPMENT OF A MAPPING APPROACH FOR TSG POWDER FLOW REGIMES

6.1 Introduction

Fundamental challenges in wet granulation have been to conquer the preferential wetting and segregation problems which are notable when using hydrophobic components in the formulation composition due to the powder's poor wetting properties. These problems have a significant effect on the final granular properties. This factor is particularly important in TSG were it is necessary to have a full understanding of the process in order to improve granule properties i.e. size and strength.

In this chapter, the influence of kneading element length and placement on the resultant granule properties i.e. size, strength, morphology is investigated. A mapping approach is developed to describe the granulation behavior based on powder wetting characteristics and TSG process variables. The mapping approach allows for the granulation behavior to be linked to TSG powder flow regimes, thus identifying TSG mixing constraints. Such a mapping approach provides a basis of scale up strategy for the TSG process.

6.2 Experimental Design

The powder mixtures used in this chapter are detailed in Chapter 3.1.1. Water was used as liquid binder at room temperature (25 °C) for its low viscosity (1.00 m Pa s). This was to ensure that the differences in the granulation behaviour observed were primarily caused by formulation properties and process variables. The granulation experiments were carried out using the TSG equipment detailed in section 3.2.2. Optimum L/S ratios given in Chapter 3.2.2 were used for all formulations investigated. The KE length i.e. 0 m, 0.0159 m (4KE), 0.0320 m (8KE), 0.0479 m (12KE), 0.0639 m (16KE) and placement i.e. 0.00795 m (2KE), 0.0159 m (4KE), 0.0320 m (8KE) were varied to obtain a fundamental understanding on the effect of processing variables on the resultant granule properties. The KE's were placed immediately after the liquid binder injection point to facilitate liquid binder distribution to occur simultaneously with the wetting and nucleation process. The experimental design was replicated for all formulations and resultant granules were characterised for size, strength, morphology.

6.3   Granule Mass Hold-Up

Figures 6-1 - 6-2. shows the effect of formulation hydrophobicity and KE length on the SME and mass hold-up. The SME was calculated in accordance with Equation 2-60.
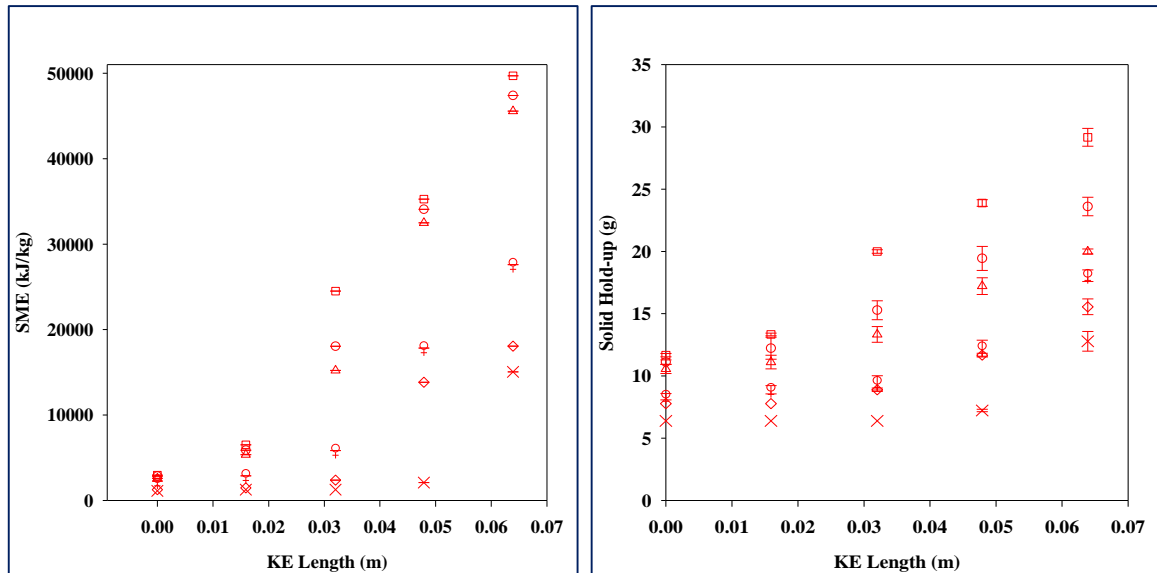
Figure 6-1. Effect of KE length on SME and TSG mass hold up for ϕ: × 0.24, ◇ 0.52, ♀ 0.74, △ 0.87, ○ 0.93, □ 1.00.
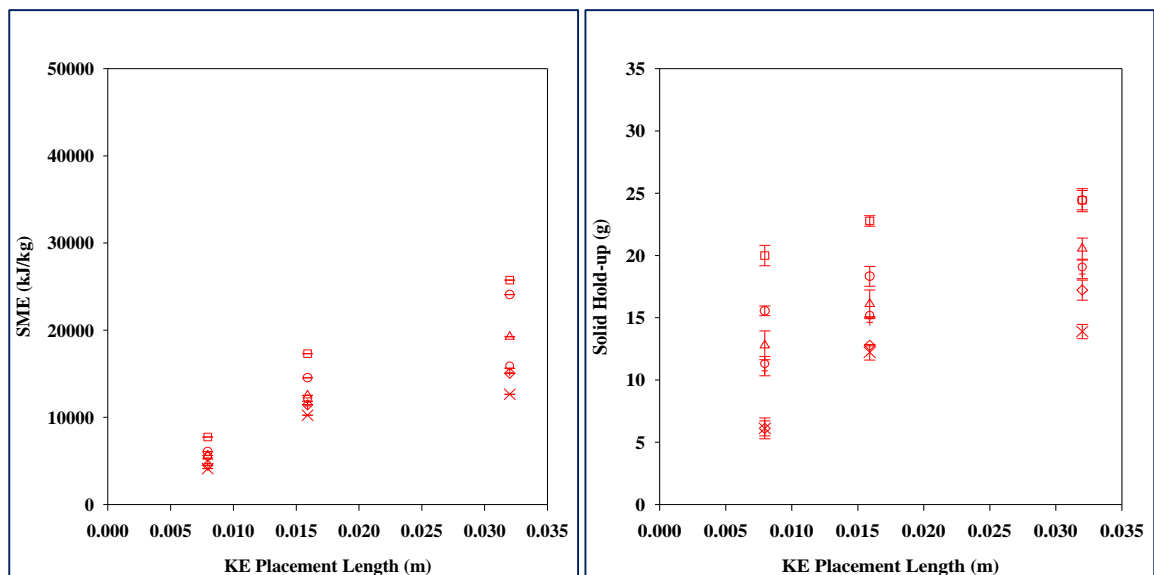
Figure 6-2. Effect of KE placement on SME and TSG mass hold up for ϕ: × 0.24, ◇ 0.52, ♀ 0.74, △ 0.87, ○ 0.93, □ 1.00.

Mass hold-up i.e. solid hold-up is defined as the amount of material remaining in the TSG barrel. It was measured by allowing the TSG to reach steady state, then the process is halted. The granules remaining inside the barrel channel are then collected to determine the quantity

of granule mass remaining (mass hold-up) in the TSG. Looking at the results shown in Figures 6-1 - 6-2, it is clear that the SME correlates linearly with mass hold-up. This correlation shows a stronger dependency to KE configuration, were an increase in KE length and placement is shown to increase SME and mass hold-up. However, the correlation between SME and mass hold-up is found to lessen with formulation hydrophobicity. This trend is due to torque reduction caused by a decrease in mass hold-up. When mass hold-up is reduced, the material residence time becomes shorter, reducing the extent of mixing of material in TSG. The relationship between mass hold-up and material residence time is given by the following expression:

$$\bar{t}_m = \frac{m_h}{\dot{m}_p}$$

where $\bar{t}_m$ is the average residence time calculated from the mass flow rate $\dot{m}_p$ and mass hold- up, m_h.

Equation 6-1 implies that longer residence times lead to increased SME values, which is expected from higher mass hold-up. According to Vercruysse et al. (2015) higher residence times are associated with increased back mixing inside the barrel [84]. However, in TSG back mixing is very difficult to control and greater control is required to be able to scale up the process. This means that there are process limits that need to be considered for TSG process optimisation and scale up strategy.

This direct dependency of SME on mass hold-up can be linked to TSG powder flow regimes. Two distinct powder flow regimes are observed, (see Figures 6-1 and 6-2). At low SME's, the TSG barrel was observed to be under filled i.e. low mass hold-up thus, operating in starved conditions. However, the SME goes from a minimum to a maximum value where the barrel was observed to be operating in a flooded state i.e. high mass hold-up as the KE length and placement were increased. The maximum SME values are limited by the equipment design therefore flooded states might not be achievable. Since the SME is shown to significantly vary with KE length and placement, it is necessary to investigate the effects of SME on granule attributes (size, strength and morphology).

6.4 Extent of Granule Formation

The effect of SME changes on the mean granule size for the different mixtures and KE configurations is shown in Figures 6-3 and 6-4. Here, the granule size is presented as a normalised ratio to describe the extent of granule formation:

$$\text{Extent of granule formation} = \frac{d_{50}\text{granule}}{d_{50}\text{particle}}$$

<div align="right">**Equation 6-2**</div>

where, $\frac{d_{50}\text{granule}}{d_{50}\text{particle}} \leq 1$ no granule formation is possible and $\frac{d_{50}\text{granule}}{d_{50}\text{particle}} > 1$ granule formation is possible.

Figure 6-3. Effect of KE length on SME and the extent of granule formation for ϕ: × 0.24, ◇ 0.52, ♀ 0.74, △ 0.87, ○ 0.93, □ 1.00.

The extent of granule formation is observed to show high sensitivity to changes in SME levels in TSG. For low SME levels, corresponding to the TSG operating under starved conditions, the extent of granule formation is reduced. This is attributed to poor liquid distribution related to powder wetting behaviour and TSG mixing conditions i.e. low shear mixing enviroment. Liquid distribution plays an important role in facilitating granule formation

i.e. when there is greater degree of contact between the powder bed and the liquid binder, the liquid will be better distributed and thus the powder will be in the best position to be granulated. The heterogeneity of the liquid binder distribution resulted in a large number of fines being produced, (see Tables 6-1 - 6-2).
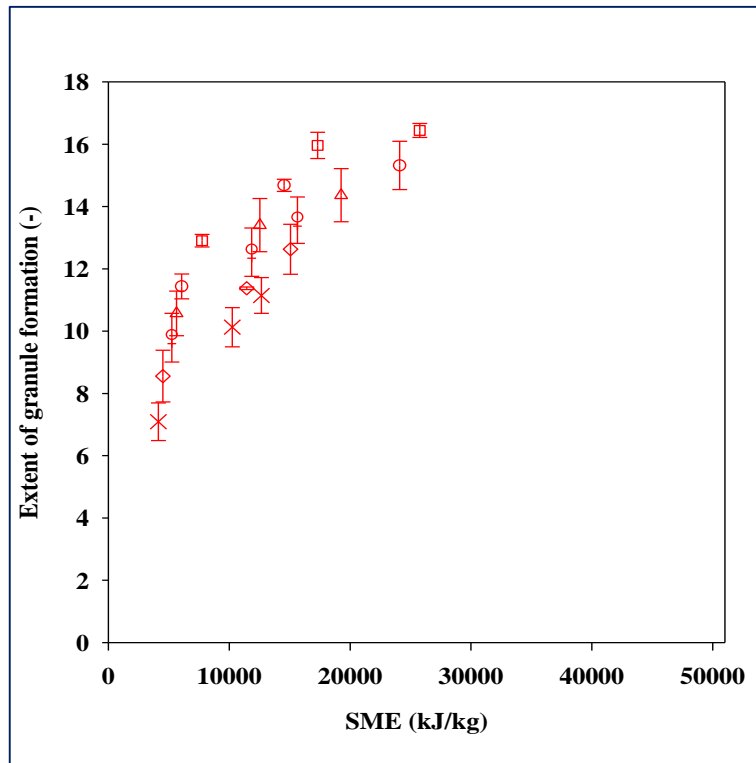
Figure 6-4. Effect of KE placement on SME and the extent of granule formation for ϕ: × 0.24, ◇ 0.52, ♀ 0.74, △ 0.87, ○ 0.93, □ 1.00.

Although the granules have space to grow when the TSG barrel is operating under "starved" conditions, the low SME's do not provide sufficient energy to redistribute the liquid binder for more hydrophobic mixtures. Thus, hydrophobic mixtures require greater amount of energy for liquid distribution in order to facilitate granule growth.

By contrast, higher SME levels i.e. longer KE length and placement resulted in increased granule formation. This is because at high SME levels, the barrel channel experiences a high degree of fill and the residence time is longer. The increased barrel fill promotes liquid binder distribution and granule compaction, aiding granule growth. The increased compaction reduced the number of fines and produced more intermediate/large granules for all formulations, (see Tables 6-1 - 6-2).

Table 6-1. Effect of KE length on the resultant granule morphology

φ	0 m	0.0159 m	0.0320 m	0.0479 m	0.0639 m
		Increase in SME level in TSG →			
1.00					
0.93					
0.87					
0.74					
0.52					
0.24					

Spherical Granules

Elongated Granules
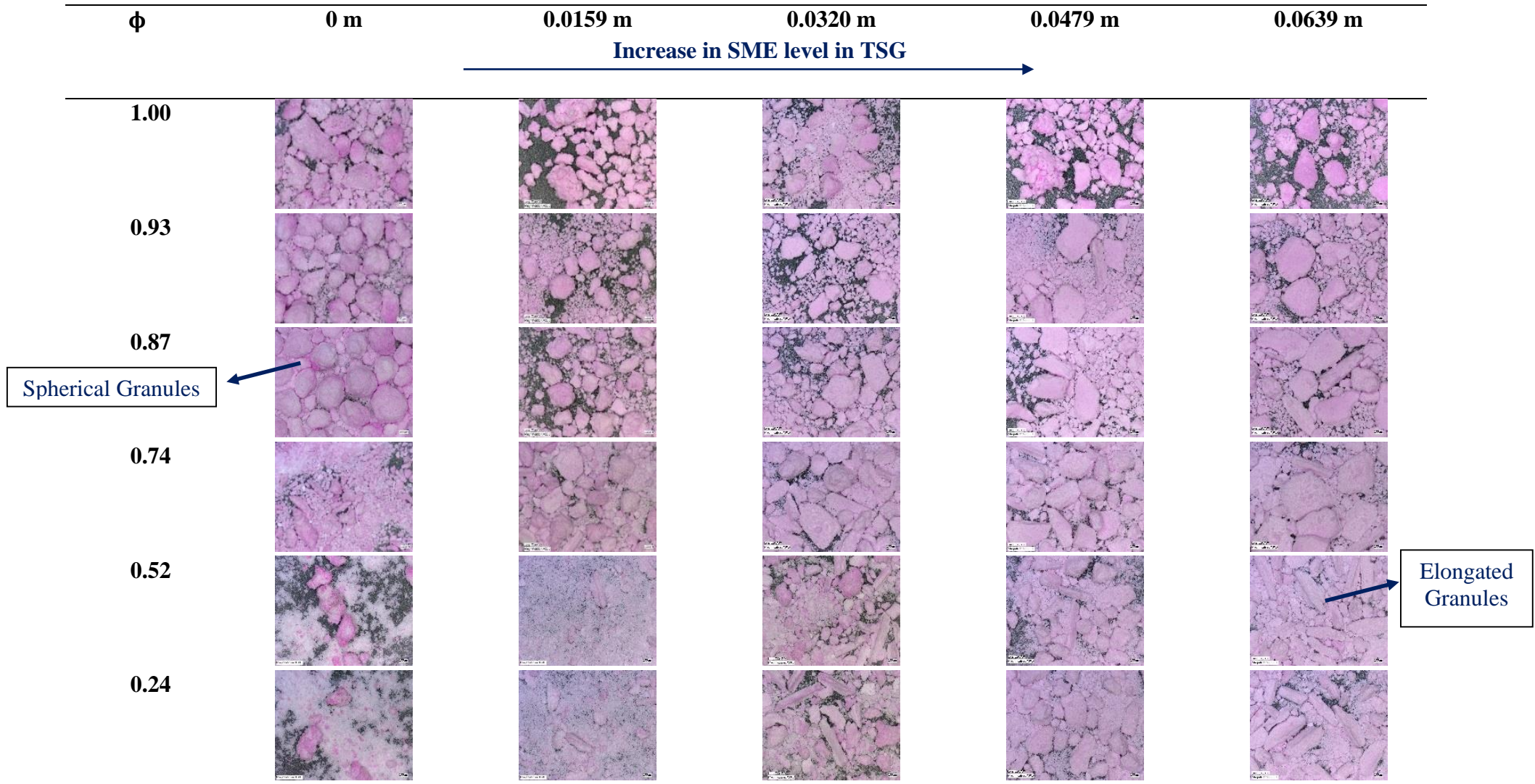
able 6-2. Effect of KE placement on the resultant granule morphology

φ	0.00795 m		0.0159 m		0.0320 m	
	Porous Granule		Increase in SME level in TSG →			
1.00						
0.93						
0.87						
0.74						
0.52						Compact Granule
0.24						
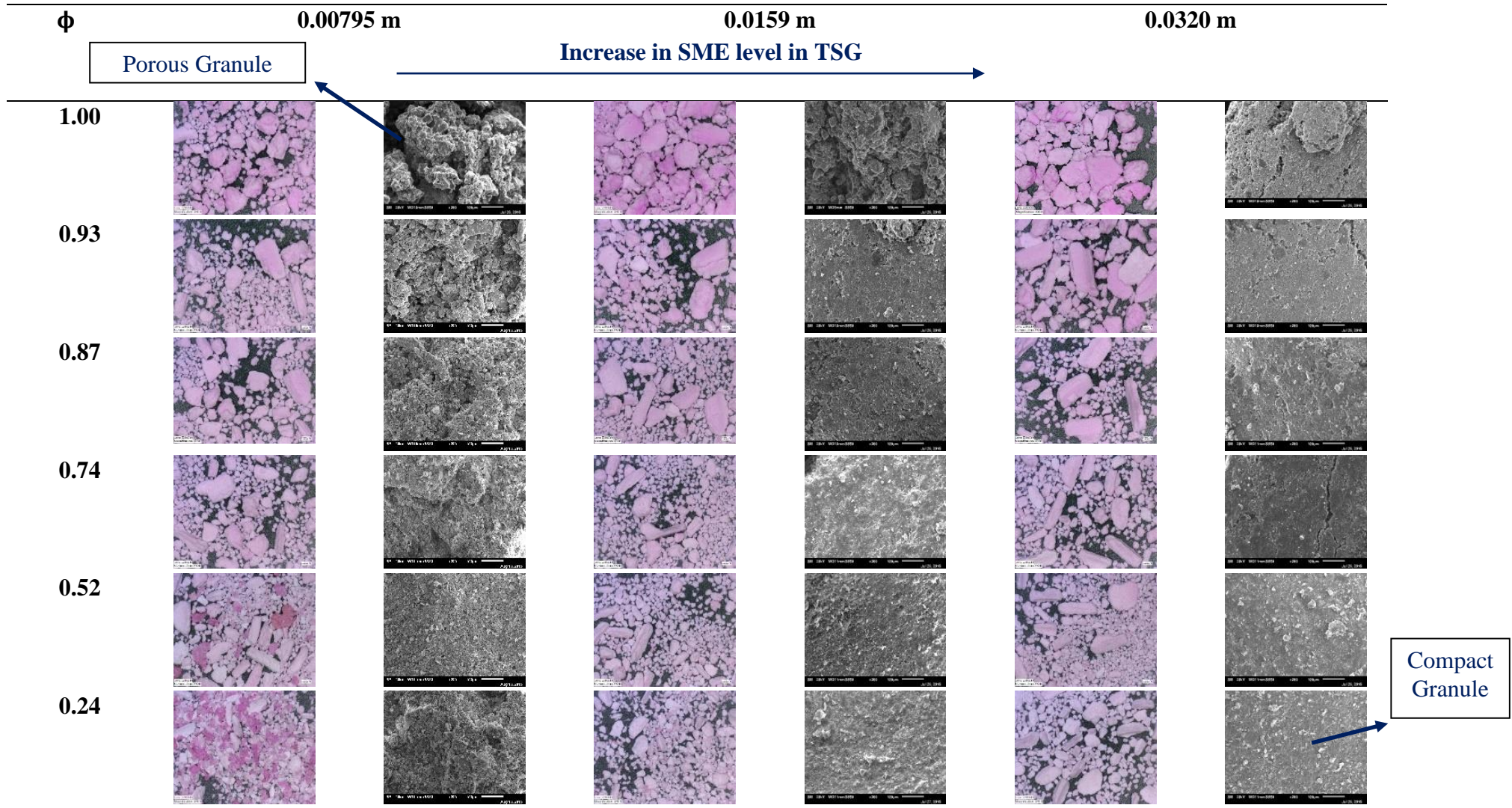
This effect was pronounced for mixtures that display hydrophilic behaviour consisting of mostly brittle material (lactose) which are observed to require shorter mixing times, to easily break through shear to form higher yield of suitable granules. However, granule growth for more hydrophobic mixtures was observed to improve with longer mixing times. The small volume and clearance between screw elements and barrel in a TSG is also dictating the maximum granule size/growth which can be achieved.

The results observed here, contradict with the findings of Yu et al. [101] were it was reported that the compressive forces from the extra KE's caused granule breakage thereby decreasing the average granule size i.e. decrease in extent of granule formation. This finding is ascribed to the length and placement of the KE's in the screw configuration. Yu et al. [101] used shorter KE length and the KE's were placed at end of the TSG barrel. Here, longer mixing section is used with KE's placed after the liquid injection point. This approach was taken to facilitate liquid binder distribution to occur simultaneously with the wetting and nucleation process in order to promote granule growth whilst minimizing breakage downstream the TSG barrel channel.

The significance of the improved mixing characteristics with higher SME levels can become a major issue when the KE mixing zone is too long i.e. above 0.00320 m, resulting in undesirable oversized granules. However, if higher SME levels are desirable, the placement of the KE screw configuration should be kept at minimal 0.0320 m length consecutively. This should be followed by CE's to relieve the stress build up and to ensure that the material is constantly flowing in TSG.

6.5 Granule Strength and Morphology

The effect of SME changes on the granule strength and morphology for the different mixtures and KE configurations is shown in Figures 6-5 - 6-6. Granules from more hydrophobic mixtures were found to be weaker in strength than mixtures which display hydrophilic behaviour. This is expected due to the hydrophobic mixtures poor powder wetting properties which limits the extent at which the liquid binder is distributed. The liquid distribution heterogeneity results in a weaker granular structure, making the granule more susceptible to breakage under stress, hence decrease in granule strength.
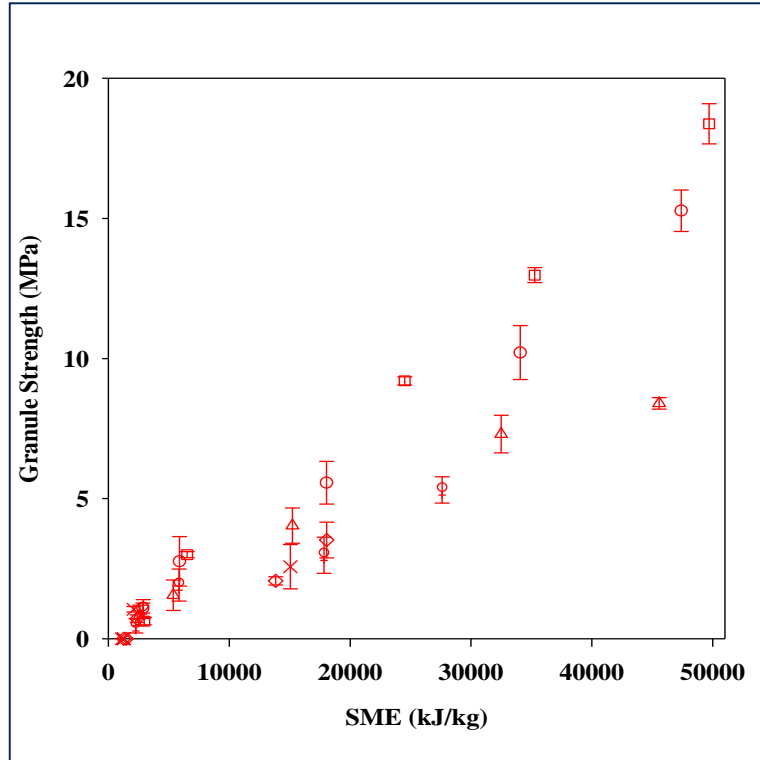
Figure 6-5. Effect of KE length on SME and granule strength for φ: × 0.24, ◇ 0.52, ♀ 0.74, △ 0.87, ○ 0.93, □ 1.00.
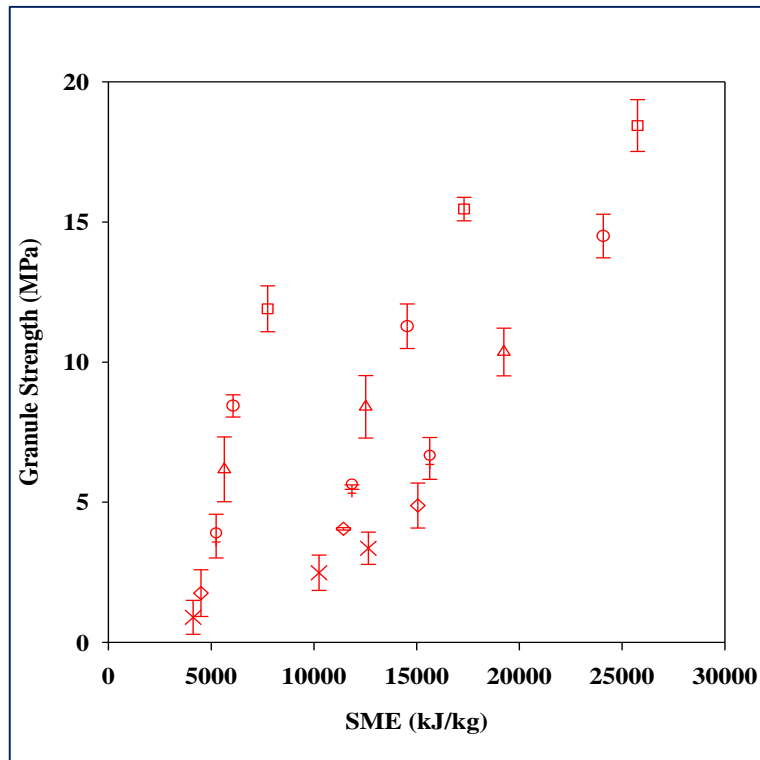
Figure 6-6. Effect of KE placement on SME and granule strength for φ: × 0.24, ◇ 0.52, ♀ 0.74, △ 0.87, ○ 0.93, □ 1.00.

The granules generated at low SME levels i.e. starved barrel fill, were generally weaker in strength, (see Figures 6-5 - 6-6). This is due to reduced compaction associated with shorter residence times at low fill levels. Images from Tables 6-5 - 6-6 show that low SME levels make granules which are more spherical in shape with smoother surface. This is suggested to be due to granule growth by layering, which minimizes granule surface irregularities resulting in weakly adhered particles on the outer granule surface, hence weaker granular strength.

However, when the SME is increased i.e. increase in barrel fill level, granule strength increased significantly. This is due to increased granule compaction promoted when the length and placement of KE's was increased. With higher barrel fill, the material residence time is increased, thereby exposing the granules to more consolidation and shear elongation. This resulted in dense granules which are irregular and elongated in structure, (see Tables 6-1 - 6-2).

6.6 Mapping Approach: Linking Wetting and Granulation behavior

The results show that there is a strong correlation between the SME and the resultant granule size, strength and morphology. Moreover, the trends observed with SME and granule properties show strong dependency on powder wetting properties. As such, a mapping approach is proposed to link powder wetting and the granulation behavior in TSG.

A comparison between the powder wetting properties and SME is shown in Figures 6-7 - 6-9. Here, the nucleation ratio and $\overline{\cos \theta^*}$ detailed in Chapter 4 and 5 are used to link the powder wetting and granulation behavior. When a liquid binder comes into contact with the powder bed, the size of the nuclei formed is dependent on the nucleation ratio defined as the weight of the nuclei formed to that of the liquid droplet and is dependent on the liquid and powder bed properties. The nucleation ratio will be influenced by how many particles come into contact with the liquid droplet inside the powder bed during spreading and imbibition. The $\overline{\cos \theta^*}$ defines the powder wetting behaviour.
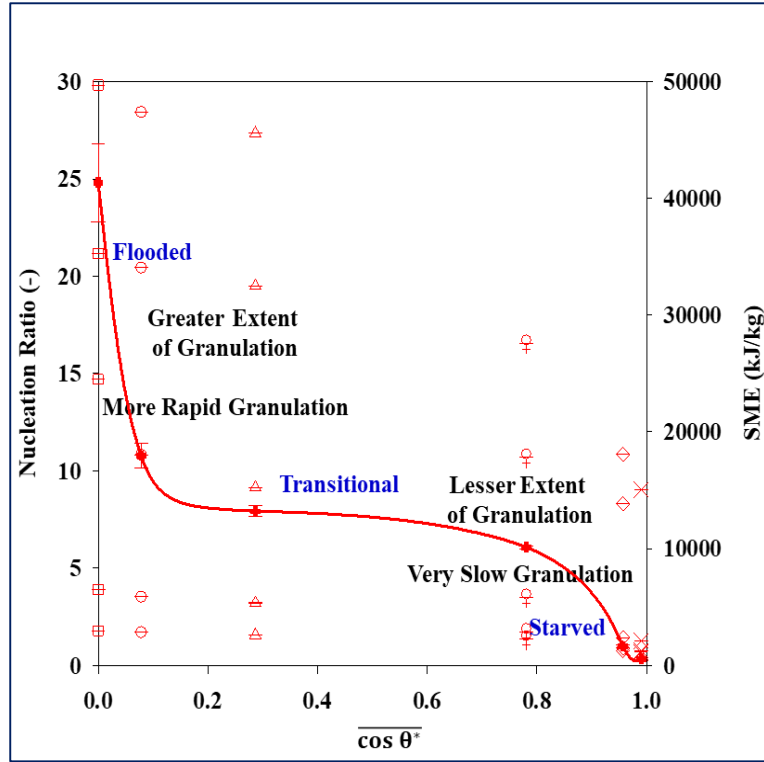
Figure 6-7. Relating powder wetting behavior to SME when varying KE length for ϕ: × 0.24, ◇ 0.52, ♀ 0.74, △ 0.87, ○ 0.93, □ 1.00. The solid line corresponds to the nucleation ratio.
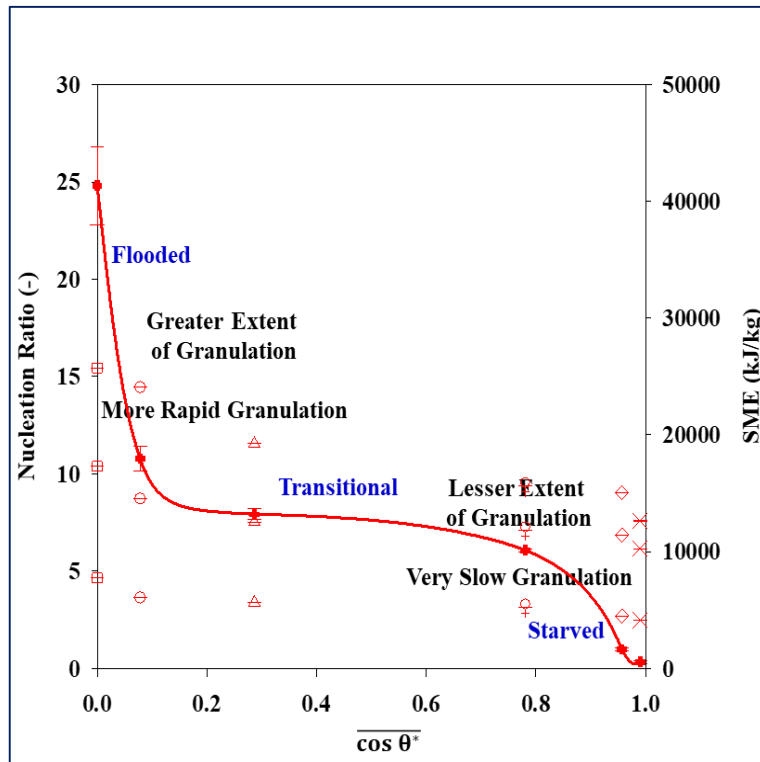
Figure 6-8. Relating powder wetting behavior to SME when varying KE placement for ϕ: × 0.24, ◇ 0.52, ♀ 0.74, △ 0.87, ○ 0.93, □ 1.00. The solid line corresponds to the nucleation ratio.
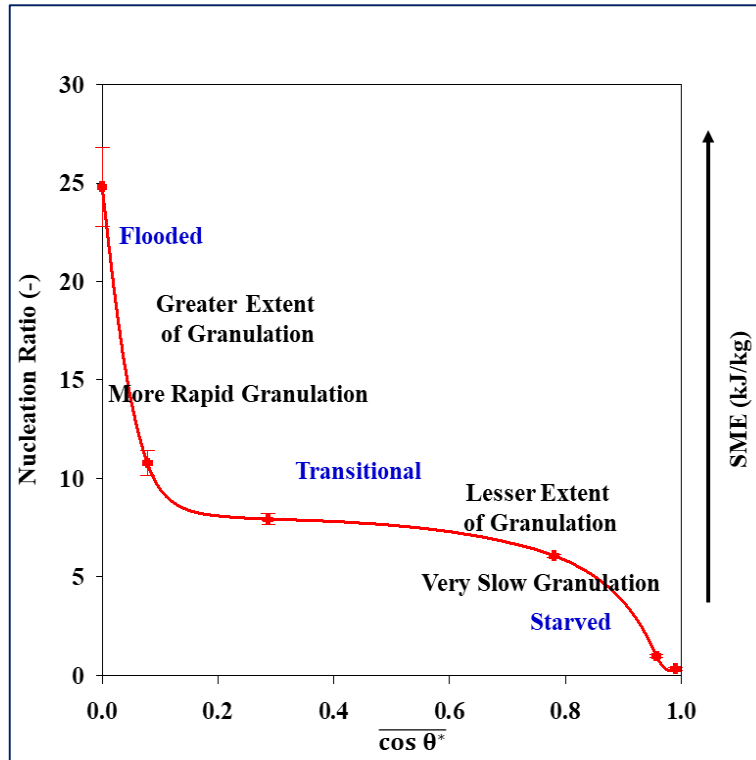
Figure 6-9. Mapping approach: linking formulation wetting properties and SME.

As can be seen, there are two distinct TSG powder flow regimes which can be identified: starved state i.e. under filled and flooded state i.e. over filled. There is also a transitional powder flow regime were the TSG barrel is filled. The powder flow regimes demonstrate the conditions under which these regimes limit granulation behavior i.e. when greater extent of granule formation and stronger granules will likely form. This approach can be used to detect the powder flow regime for a given combination of mixtures and screw configuration in TSG. By observing the mapping approach conclusions about influence of powder wetting properties and SME on granulation behavior can be drawn.

Evidently, high SME values i.e. flooded state correspond to powders which display good wetting properties i.e. the fast imbibition of the liquid droplet dissipates any available interfacial energy rapidly which promotes more particles to be in contact with the liquid quickly resulting in large nucleation ratios (see Figure 6-7 -6-9). When the TSG is operating in a flooded state, material residence times are longer, allowing for more time for consolidation and densification of granules, thereby increasing granule formation and strength. However, low SME values i.e. starved state correspond to powders with display poor wetting properties i.e. longer imbibition times as the liquid binder migrates until it finds a hydrophilic pathway where particles will be picked up due to capillary action, resulting in liquid imbibition occurring via

site percolation of the hydrophilic particles. This site percolation mechanism causes less particles to come into contact with the liquid droplet, reducing the nucleation ratio (see Figure 6-7 -6-9). These results suggest that the compressive forces exerted by the KE's were not sufficient to dissipate the high interfacial energy from the solid-liquid interactions. This is evident from the larger number of fines produced even with increased KE mixing section, hence decrease in mixing extent i.e. low SME values.

As explained by Hapgood et al. [112] liquid binder flow into poorly wetting powder beds is slow, therefore mechanical dispersion is key to controlling the granulation behavior and resultant granule properties. That is, to be able to form granules with desirable properties when using powders with poor wetting properties stronger mechanical dispersion than that provided by the screw configuration used in the current study are required.

However, operating above the current screw configuration might not be achievable due to TSG energy input limitations. For the regime map to be beneficial, dimensional analysis should be performed to decide what should be plotted to reduce the number of experiments and to make it more universally applicable in tailoring production processes. However, at this stage, understanding the influence of the process parameters has been useful to show that this concept should be further pursued for product development purposes.

6.7 Conclusions

The results reported in this chapter show that the influence of powder wetting properties and TSG process variables on the granulation behavior can be described by a single parameter, specific mechanical energy (SME). This behaviour was assessed using TSG mass hold-up, extent of granule formation and granule strength.

The main observations and conclusions described in Chapter 6 are highlighted below:

- At low SME levels, the TSG is observed to be operating in starved conditions i.e. low mass hold-up resulting in granules with reduced extent of granule formation and strength.
- However, the extent of granule formation and strength improved with increase in SME levels due to increase in TSG mass hold-up encouraging the material to spend more time in the barrel channel being mixed.

- These results suggest that longer material residence time and greater amount of energy are required to distribute the liquid binder to produce granules with improved size and strength.

- As the SME showed stronger dependency on screw configuration and formulation properties, a mapping approach is presented which links the powder wetting behaviour to the SME and revealed to be crucial in describing the powder flow regimes in TSG.

It is felt that the observations and conclusions from Chapter 6 indicate the need for a further detailed investigation into the effect of RTD, screw configuration types and powder flow regime (starved versus flooded) in TSG on the resultant granular properties as little work has been reported on the subject in TSG granulation of hydrophobic powders.

7 PRACTICAL IMPLICATIONS OF SCREW ELEMENT TYPE ON THE REDUCTION OF FINES IN TSG

7.1 Introduction

The wetting and nucleation stage in wet granulation involves the addition, interaction and distribution of the liquid binder in the powder bed to form primary granules. Powder wetting and liquid distribution uniformity is significant at this stage in producing uniform granules with a narrow granule size distribution, a key factor which is essential for improved product quality [2]. However, good wetting and nucleation behaviour becomes challenging when a hydrophobic component is incorporated in the formulation as this leads to poor liquid binder distribution in the granulation process [113].

Insufficient liquid distribution hinders granule growth, leading to generation of excessive fines (un-granulated powder) and granule size with a wider distribution [96,101]. In the pharmaceutical industry, excessive fine generation impacts product critical quality attributes such as appearance, content and uniformity and results in low product yield, reduced productivity, increased down time and costs. Typically, high liquid to solid (L/S) ratios are used to reduce the excessive fines [105]. However, this results in either very large agglomerates and/or over wetted sticky non-agglomerates which are not usable in downstream processes such as tableting and encapsulation.

In the pharmaceutical industry, TSG is favoured over batch granulation in controlling the excessive generation of fines, mainly due to its flexibility and the modularity of its screw configuration which is useful in manipulating the targeted product attributes e.g. size, strength and porosity [5,84]. In the literature, most studies on understanding the screw configuration mixing performance of TSG have focused on conveying and kneading elements, CE's and KE's respectively particularly on easily wettable formulations. However, limited studies have been carried out to investigate the influence of different forms and geometries of mixing elements (ME's) on the TSG mixing performance.

This study focuses on the role that various screw elements play in the reduction of fines in TSG when using increasing amounts of hydrophobic component in the formulation. The elements used are conveying-type elements (CE-type), kneading elements (KE-type) and tooth

mixing-type elements (TME-type). Fines are defined as < 150 µm granules which is based on the primary powder particle size. Further, this work attempts to rationalize the positioning of the various screw elements along the barrel by studying the granule size, granule porosity, liquid binder and residence time distribution results. The length of the screw elements was kept constant to ensure constant and comparable mixing quality.

7.2 Experimental Design

The powder mixtures used in this chapter are detailed in Chapter 3.1.1. The liquid binder was comprised of 5 wt% HPC (µ = 9.40 m Pa s). The granulation experiments were carried out using the granulation equipment detailed in Chapter 3.2.2. However, only a small length of the barrel was used as the study was focused on the wetting and nucleation stage of TSG (see Figure 7-1). Both the low and optimum L/S ratios given in Chapter 3.2.2 were used for all formulations investigated.
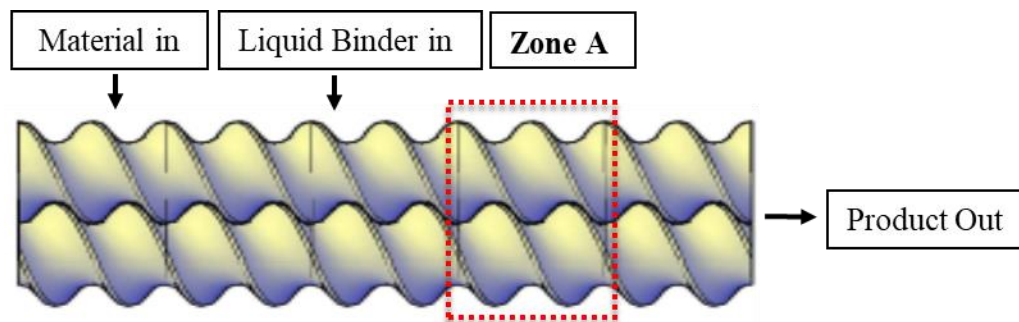
Figure 7-1. Schematic of the TSG screw configuration.

Table 7-1. Various types of screw elements

CE = 1 L/D	lCE = 1 L/D	fCE = 1 L/D
V_{free} = 5.50 cm³	V_{free} = 5.50 cm³	V_{free} = 5.50 cm³
KE = 1/4 L/D	nTME = 1/4 L/D	wTME = 1/2 L/D
V_{free} = 1.38 cm³	V_{free} = 1.38 cm³	V_{free} = 2.75 cm³

Table 7-1 illustrates the various screw configurations used to investigate TSG performance when using the formulations selected for this study. A total of six different screw configurations (Thermo Fisher Scientific, UK), were investigated which consisted of various elements such as CE's, fine cut conveying elements (fCE's), large cut conveying elements (lCE's), KE's, narrow tooth mixing elements (nTME's) and wide tooth mixing elements (wTME's). These differ in screw pitch defined by the length and diameter ratio (L/D), geometry design and V_{free} determined by water displacement (see Table 7-1 and Appendix A, section 11.1). The fCE's and lCE's are directly made from the CE by cutting through the screw flights in the axial direction. As a result, these are grouped as conveying-type elements, whilst the KE's, nTME's and wTME's are referred to as mixing type elements. The screw elements were placed 16 mm from the end of the TSG barrel at a fixed location in Zone A (see Figure 7-1). Although Figure 7-1 shows CE in Zone A, in this location the screw elements were varied to include other types of screw elements investigated in this study. The length of the screw elements was kept constant (16 mm) to eliminate the effects of their length on the TSG mixing performance. Full description of characterisation techniques is given in Chapter 3.

7.3 **Work of Adhesion**

To understand the transitions in the granulation behaviour when varying the screw element type, the powder wetting behaviour was characterized using the W_A (see Equation 2-8 and Figure 7-2). As the powder wetting behaviour was found to change significantly based on the W_A, the results of the liquid binder distribution, RTD and granule porosity are presented for ϕ = 1.00 which displays characteristic hydrophilic behaviour and high W_A and ϕ = 0.74 which displays hydrophobic behaviour and low W_A. Thus, in this study the granulation behaviour is discussed in terms of region I and II, which are characteristic of hydrophilic and hydrophobic behaviour respectively.
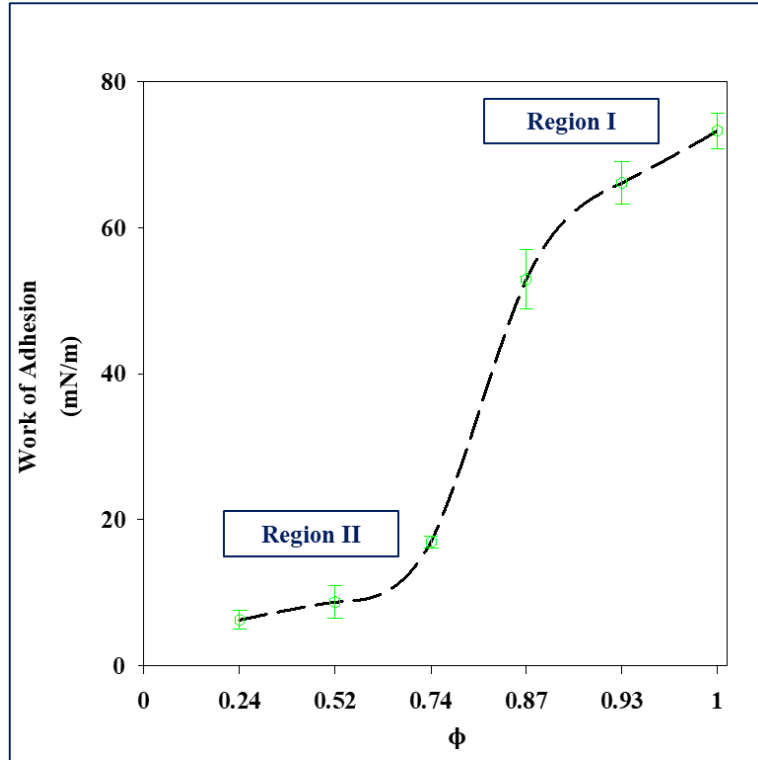
Figure 7-2. Powder wetting behavior of different formulations.

7.4 Conveying-Type Elements (CE, ICE, FCE)

Figures 7-3 - 7-4 illustrate the effect of CE, lCE and fCE on the percentage of < 150 μm granules and the mean granule size (d_{50}) for formulations in region I and II. There were between $\approx$ 52-62 % (low L/S), $\approx$ 31-53 % (opt L/S) of < 150 μm granules produced in region I and $\approx$ 83-95 % (low L/S), $\approx$ 81-95 % (opt L/S) of < 150 μm granules produced in region II when using CE's in the screw configuration. Although, there were excessive formation of < 150 μm granules when using CE, in region I there is evidence of some granules being formed for powders that display characteristic hydrophilic behaviour, (see Figure 7-4).

The granules formed in region I are oversized and resemble more of a spherical shape of the liquid binder, with an inherent intragranular porosity of $\varepsilon \approx$ 44 %, (see Table 7-2). These results demonstrate that CE's transport material without deforming it (changing its shape) as less energy is dissipated by the CE's. The granules produced contain liquid binder, which is concentrated in the central core of the granules, with < 150 μm granules coating the outer layer of the granule, (see Table 7-2).

117
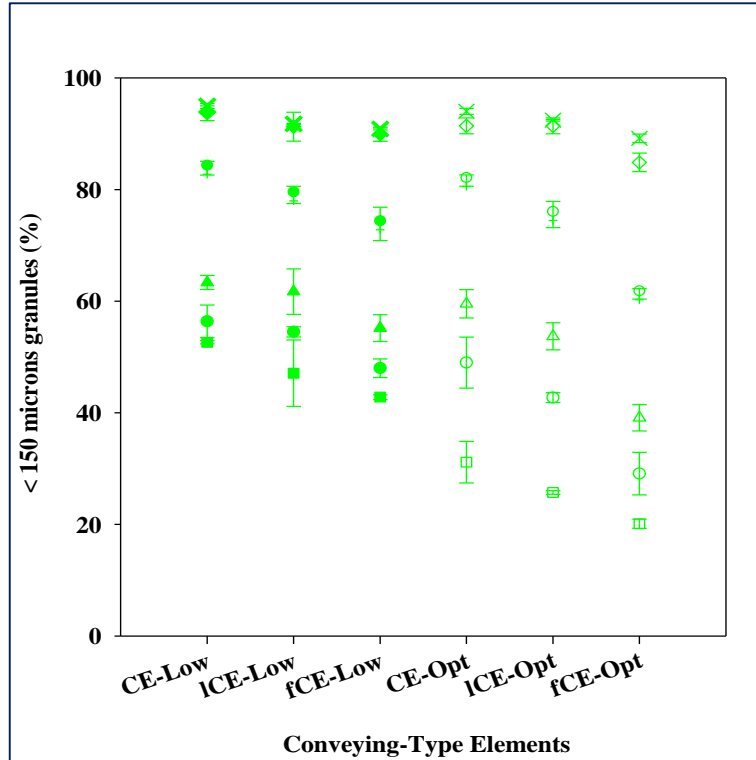
Figure 7-3. Percentage of < 150 μm granules for different formulations which are represented using the symbols ϕ: × 0.24, ◇ 0.52, ⚲ 0.74, △ 0.87, ○ 0.93 , □ 1.00. The filled and non-filled symbols represent low and optimum L/S ratios respectively.
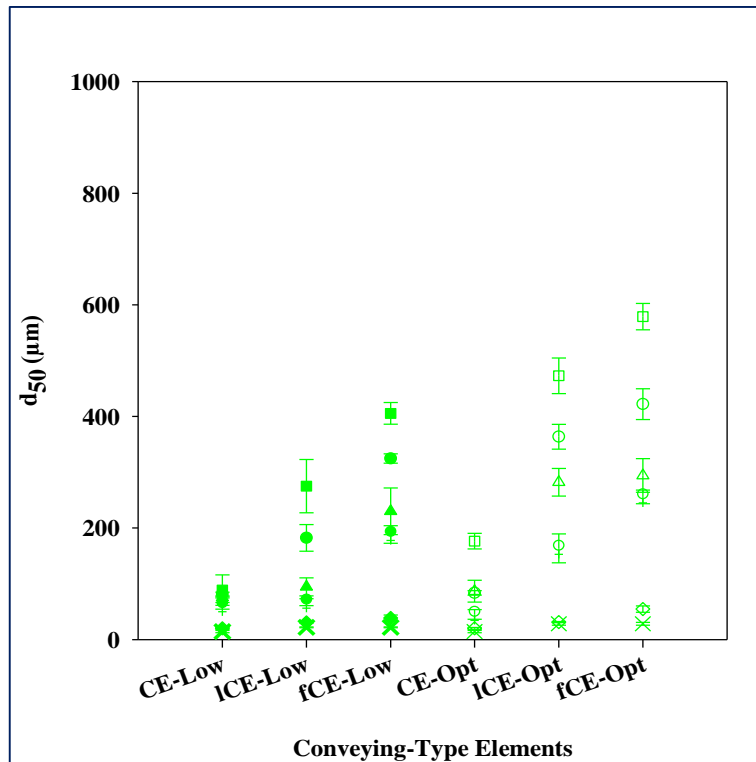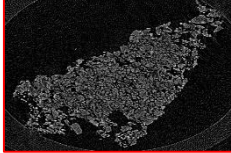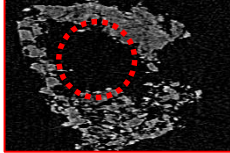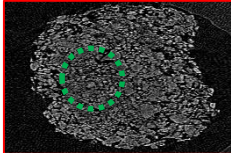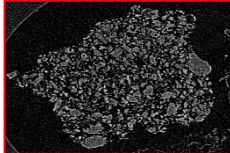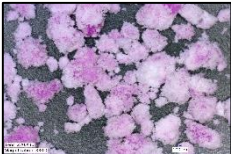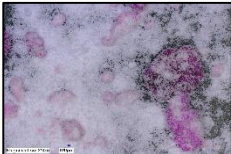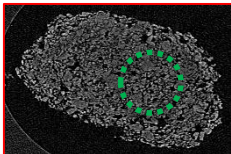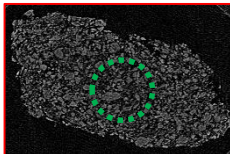
Figure 7-4. d_{50} granule size for different formulations which are represented using the symbols ϕ: × 0.24, ◇ 0.52, ⚲ 0.74, △ 0.87, ○ 0.93 , □ 1.00. The filled and non-filled symbols represent low and optimum L/S ratios respectively.

118

Table 7-2. Visual observations of the TSG barrel and resultant wet granules images for conveying-type elements at optimal L/S

	Region I		Region II	
* Screw-CE				
Granule-CE		$\varepsilon = 44\pm4.6\ \%$ $p = 0.739\pm0.02$ $\Psi = 7.2\pm1.02\ \%$ $\bar{t}_m = 8.5\pm0.5\ s$		$\varepsilon = 65\pm5.5\ \%$ $p = 0.701\pm0.01$ $\Psi = 6.3\pm0.1\ \%$ $\bar{t}_m = 9.9\pm0.2\ s$
# Screw-lCE				
Granule-lCE		$\varepsilon = 28\pm1.9\ \%$ $p = 0.651\pm0.03$ $\Psi = 8.0\pm0.53\ \%$ $\bar{t}_m = 9.9\pm1.0\ s$		$\varepsilon = 35\pm0.3\ \%$ $p = 0.695\pm0.01$ $\Psi = 7.5\pm0.63\ \%$ $\bar{t}_m = 9.0\pm0.1s$
# Screw-fCE				
Granule-fCE		$\varepsilon = 24\pm2.7\ \%$ $p = 0.584\pm0.09$ $\Psi = 24\pm2.5\ \%$ $\bar{t}_m = 10\pm1.3\ s$		$\varepsilon = 25\pm0.7\ \%$ $p = 0.515\pm0.03$ $\Psi = 15\pm0.57\ \%$ $\bar{t}_m = 10\pm0.4\ s$
* Starved screw states with non-mixed regions	**# Partially filled screw channel**	**Hollow granule (liquid marble)**	**Inherent intragranular (particle-particle) porosity**	

Figure 7-5. Binder distribution curve across different granule size classes for the conveying-type elements at optimal L/S ratio for φ: ♀ 0.74 and □ 1.00 which represent region I and II respectively.

Figure 7-6. RTD distribution for the conveying-type elements at optimal L/S ratio for φ: ♀ 0.74 and □ 1.00 which represent region I and II respectively.

Furthermore, in region II there was progressive increase in the percentage of < 150 μm granules and decrease in the granules formed with decrease in W_A, leading to the formation of liquid marbles (hollow granules) with high inherent intragranular porosities of $\varepsilon \approx 65$ %, (see, Table 7-2). These results indicate that when using CE's, the granules are formed by drop granulation which is when the liquid binder comes into contact with the powder bed [105] and growth by layering of < 150 μm granules on the outer granular surface and liquid droplet in region I and II respectively. The growth by layering led to liquid binder heterogeneity across different size classes with larger sized granules containing higher liquid binder dye ratio, (see Figure 7-5).

Figure 7-6 illustrates the effect of conveying-type elements on the RTD profile. The liquid heterogeneity observed with CE's is attributed to the low stresses exhibited by these elements upstream and downstream of the TSG barrel which decrease their mixing capability [77]. The low stresses cause minimal backflow were $\Psi \approx 7.2$ % in region I and $\Psi \approx 6.3$ % in region II and, make it easier for material to be quickly conveyed out of the TSG. This reduced the $\bar{t}_m$ which was found to be ≈ 8.5 s and ≈ 9.9 s for region I and II respectively, (see Figure 7-6 and Table 7-2). The poor mixing displayed by the CE's is further evident from the values of p obtained which ranged from 0.7 - 0.75. These p values indicate a plug flow regime, which is unfavorable for mixing in TSG [114].

The CE's operate in a starved 'less filled' screw state as indicated by the presence of non-mixed regions, (see Table 7-2), due to their large screw pitch which determines the fill level of the screw channel [74]. This resulted in the larger screw pitch of the CE's having greater free volume in the screw channel as observed in Table 7-1 - 7-2, leaving space for granules to grow by layering, resulting in some oversized agglomerates especially for formulations within region I, (see Figure 7-4). This growth means that the CE's are not capable of achieving a higher degree of fill, which invalidates their placement before and after the mixing zone to achieve a higher degree of fill to promote mixing.

Inclusion of lCE's in the screw configuration resulted in the oversized granules from the CE's being fragmented into medium granules in region I (see Table 7-2), leaving a layer of liquid on the granule surface to be available for further agglomeration of < 150 μm granules, thus increasing the granule size in this region, (see Figure 7-4). Further reduction of < 150 μm granules and increase in the granule size, (see Figure 7-3 - 7-4) was observed when fCE were

used in the screw configuration in this region. In region II, the lCE's and fCE function to break up the liquid marble, however only minimal granule growth was achievable, (see Figure 7-4 and Table 7-2).

The observed trend of the reduction in < 150 μm granules with introduction of lCE's and fCE's is due to their cuttings through the screw flights in the axial direction, which provides less chamber volume for material passing through. When the screw flight gap is reduced by the increased axial openings of the conveying-type elements (CE< lCE< fCE), the number of channels available for material to pass through increases, which helps the elements to resist material flow due to a decrease in the conveying transport efficiency from its optimum level as indicated by the reduction in p (see Table 7-2).

As a result, the higher number of axial opening elements lCE's and fCE's operate in a partially filled screw level, (see Table 7-2). This screw fill level state encourages the material to spend more time in the granulator being fragmented and compacted to some extent which resulted in a decrease in the inherent intragranular porosity when the axial openings of the screw were increased, (see Table 7-2).

When operating at a partially filled screw level, the increased axial opening elements promote back mixing where the material flows in the opposite direction of the positive material flow, increasing φ. This observation is illustrated in Table 7-2 were $\Psi \approx 8.0$ % (ICE) for region I and $\Psi \approx 7.5$ % (ICE) for region II and $\Psi \approx 24$ % (fCE) for region I and $\Psi \approx 15$ % (fCE) for region II.

This material flow mechanism promoted granule fragmentation which redistributed the liquid binder to some extent, (see Figure 7-5 and Table 7-2). However, the "simple" granule fragmentation process was not enough to sufficiently mix the solid and liquid due to the minimal back mixing and small $\bar{t}_m$ which were ICE ≈ 9.9 s, fCE ≈ 10 s for region I and ICE ≈ 9.0 s, fCE ≈ 10 s for region II and, resulting in liquid binder heterogeneity across the granule size range, (see Figure 7-5 and Table 7-2).

These results indicate that the CE-type elements have relatively poor cross-sectional mixing and their mixing is concentrated mainly in the intermeshing region of the TSG, even at increased barrel fill level. Thus, the flow of the CE-type elements does not bifurcate forward

and backward enough, which reduces their cross-sectional mixing capability, especially when powders are not easily wettable in region II.

The role of increased axial openings of the screw elements is to reduce the internal V_{free} (which is different from the bulk V_{free} presented in Table 7-1) of the intermeshing gap and cross-sectional area,. These are necessary to compress the material and achieve higher degree of fill before the mixing zone in TSG, factors required to increase stress in the system to promote better mixing. The reduced internal free volume is defined as the smallest space the material must go through per screw rotation. Therefore, it is suggested that the higher axial opening elements (lCE's and fCE) should be placed before the first mixing zone, instead of the CE's.

7.5 Kneading Elements (KE's)

Figures 7-7 - 7-8 illustrate the percentage of < 150 µm granules and mean granule size (d_{50}) produced when using KE, nTME's and wTME's in the screw configuration. In contrast to the conveying-type elements, the inclusion of KE's in the screw configuration reduced the percentage of < 150 µm granules in region I, where between $\approx$ 30-47 % (low L/S) and $\approx$ 7-25 % (opt L/S) of < 150 µm granules are obtained, (see Figure 7-7). Consequently, the size of granules in this region increased, (see Figure 7-8).

The increase in the granule size in region I is because in the KE zone, the oversized granules from the CE zone are fragmented into smaller sizes as it was impossible to transport the granules without deformation through the small internal free volume of the KE zone, (see Table 7-3). These smaller sized granules are forced into the KE intermeshing disc-disc gap by the kneading action, resulting in the liquid binder inside the granules being squeezed to the outer granule layer and barrel surface. The liquid binder re-penetrates the powder bed and the KE re-mixes it to encourage better liquid binder distribution, (see Figure 7-9) and further agglomeration increasing the granule size, (see Figure 7-8). Thus, material does not pass the KE zone without being agglomerated to some extent in region I.
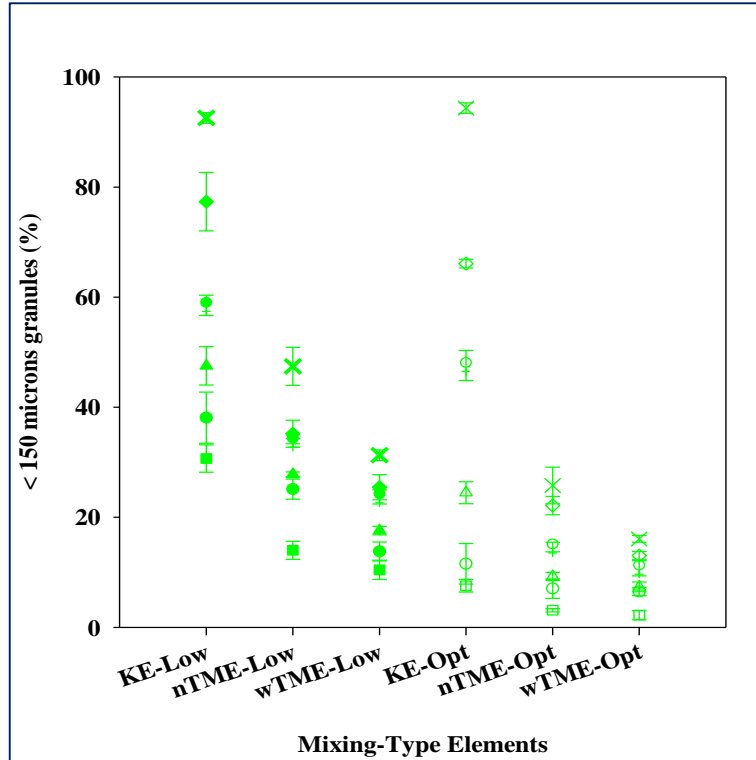
Figure 7-7. Percentage of < 150 μm granules for different formulations which are represented using the symbols φ: × 0.24, ◇ 0.52, ♀ 0.74, △ 0.87, ○ 0.93 , □ 1.00 . The filled and non-filled symbols represent low and optimum L/S ratios respectively.
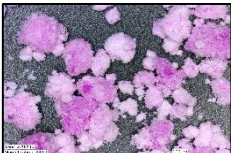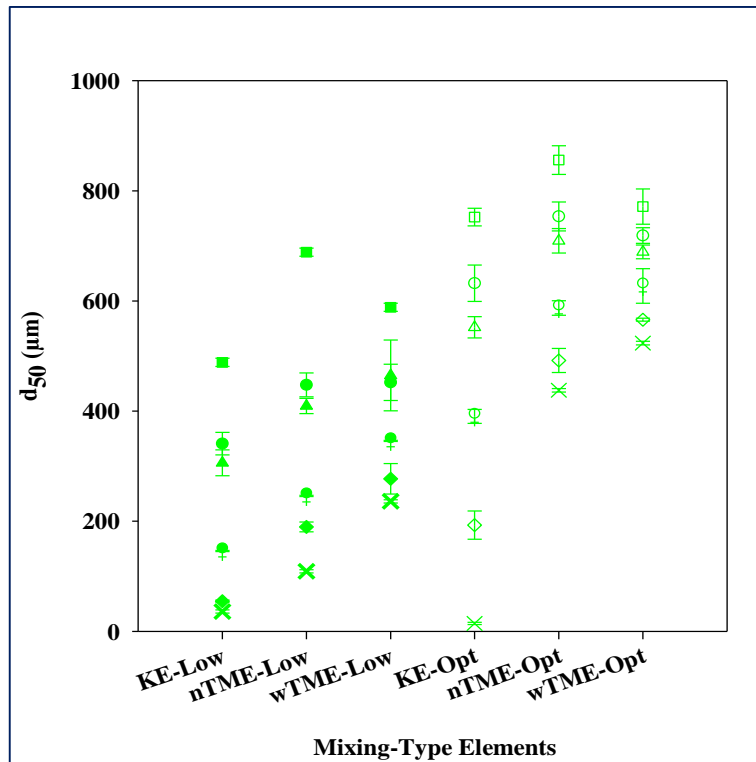

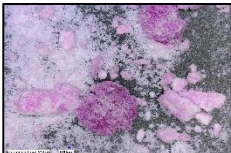**Figure 7-8. d_{50} granule size for different formulations which are represented using the symbols φ: × 0.24, ◇ 0.52, ♀ 0.74, △ 0.87, ○ 0.93 , □ 1.00 . The filled and non-filled symbols represent low and optimum L/S ratios respectively.**

125

Table 7-3. Visual observations of the TSG barrel and resultant wet granules images for mixing-type elements at optimal L/S

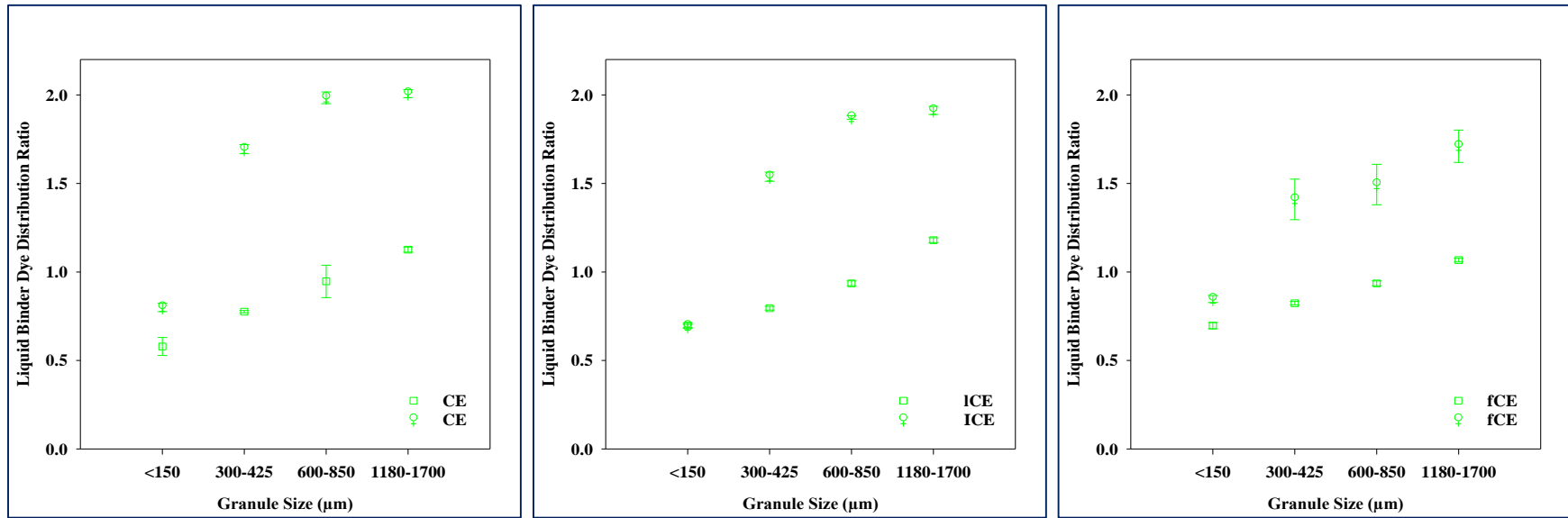|	Region I		Region II	
# Screw-KE				
Granule-KE		$\varepsilon = 12\pm0.9$ % $p = 0.180\pm0.003$ $\Psi = 39\pm0.23$ % $\bar{t}_m = 22\pm0.9$ s		$\varepsilon = 27\pm5.3$ % $p = 0.590\pm0.005$ $\Psi = 31\pm0.13$ % $\bar{t}_m = 13.7\pm0.3$ s
ℒ Screw-nTME				
Granule-nTME		$\varepsilon = 30\pm1.2$ % $p = 0.132\pm0.003$ $\Psi = 56\pm2.1$ % $\bar{t}_m = 39\pm0.9$ s		$\varepsilon = 19\pm0.7$ % $p = 0.183\pm0.003$ $\Psi = 53\pm1.4$ % $\bar{t}_m = 31\pm0.9$ s
ℒ Screw-wTME				
Granule-wTME		$\varepsilon = 31\pm0.9$ % $p = 0.209\pm0.003$ $\Psi = 38\pm1.4$ % $\bar{t}_m = 61\pm0.9$ s		$\varepsilon = 21\pm2.3$ % $p = 0.141\pm0.003$ $\Psi = 79\pm0.5$ % $\bar{t}_m = 42\pm0.9$ s
# Partially filled screw channel	ℒ More filled screw channel	⬭ Screw cutting porosity	⬭ Inherent intragranular (particle-particle) porosity	
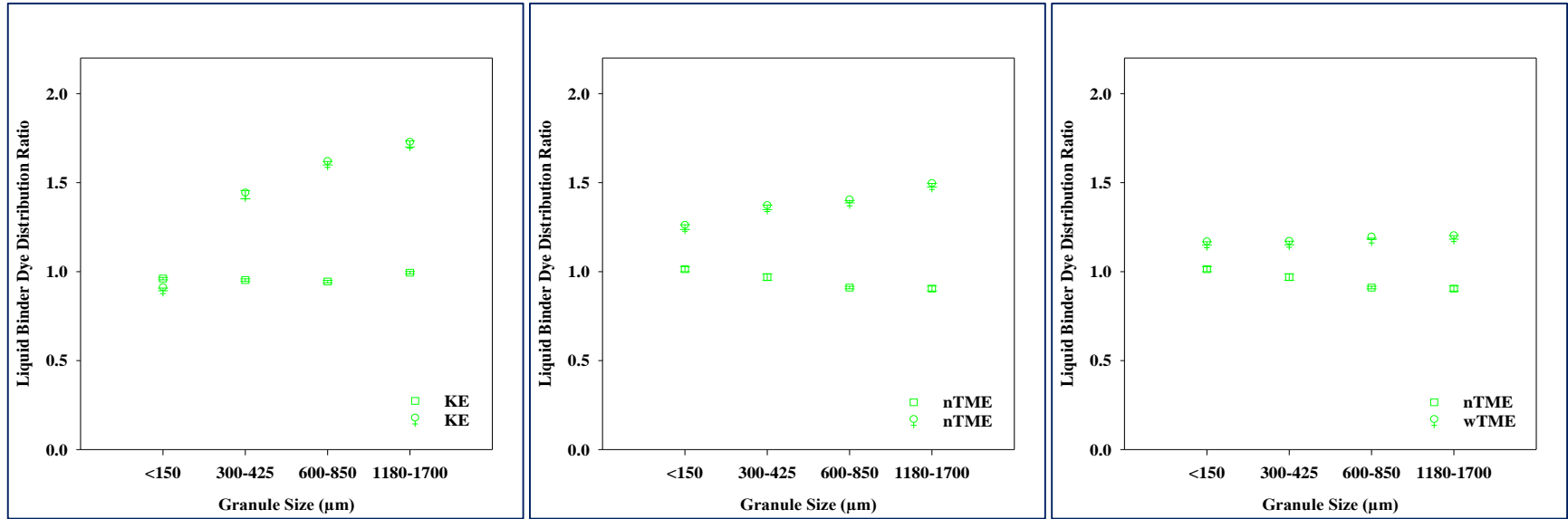
Figure 7-9. Binder distribution curve across different granule size classes for the conveying-type elements at optimal L/S ratio for ϕ: ♀ 0.74 and □ 1.00 which represent region I and II respectively.
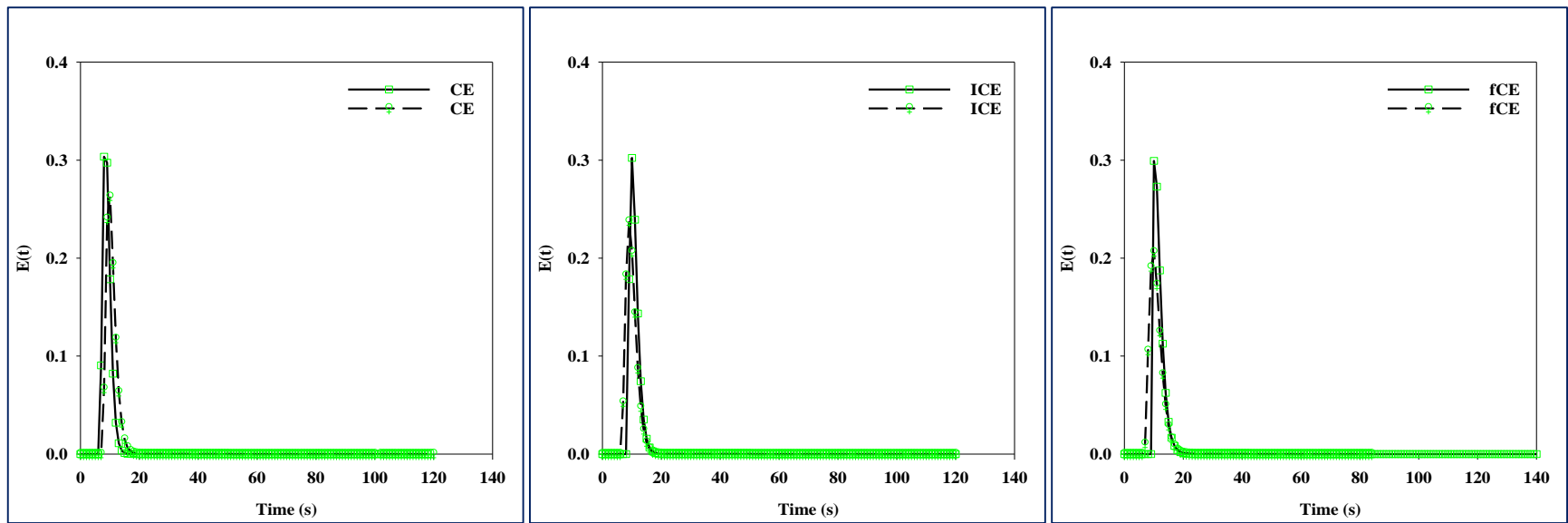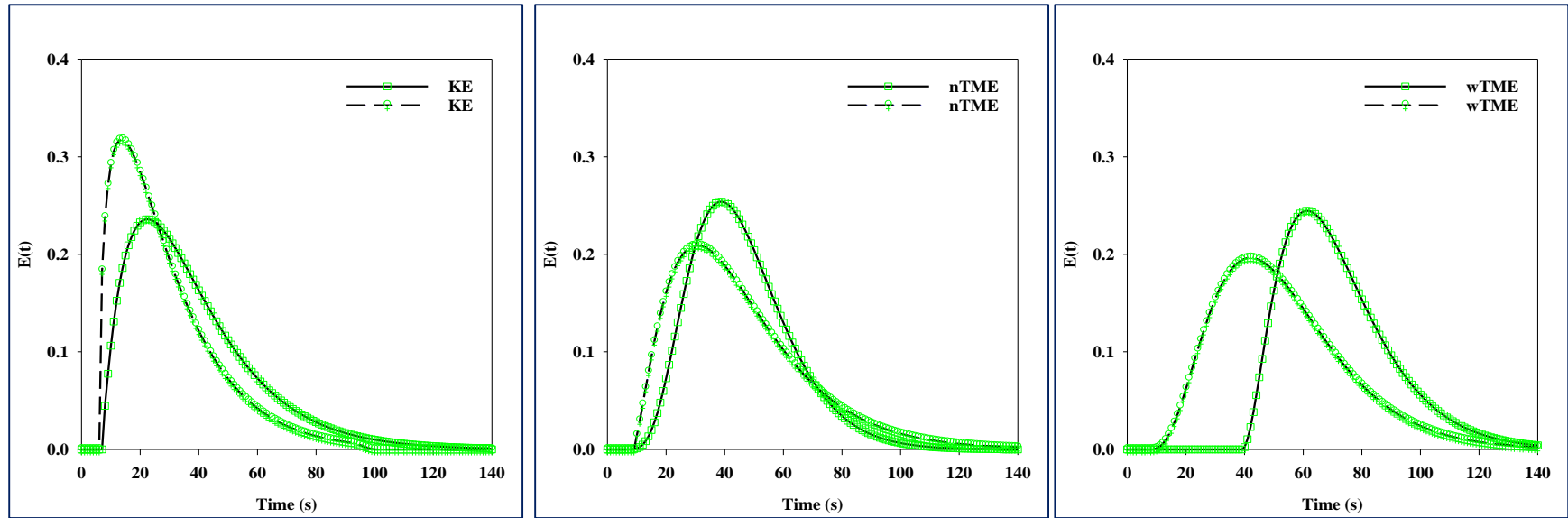
Figure 7-10. RTD distribution for the mixing-type elements at optimal L/S ratio for ϕ: ♀ 0.74 and □ 1.00 which represent region I and II respectively.

With inclusion of KE in the screw configuration, there were between $\approx$ 58-92 % (low L/S) and $\approx$ 47-94 % (opt L/S) of < 150 μm granules produced in region II. The continued generation of excessive percentage of < 150 μm granules with inclusion of KE in this region is attributed to the KE staggering angle of 60° used in this work, not providing enough high shear environment for solid and liquid exchange which are required to sufficiently distribute the liquid binder in this interfacial driven region. As a result, the liquid binder dye is more concentrated in larger sized granules in region II, (see Figure 7-9).

The RTD profiles of KE's in region I and region II are shown in Figure 7-9. In contrast to the conveying-type elements, with inclusion of KE's in the screw configuration for region I, the tracer initially appears at $\approx$ 7 s which represents t_{min}. Consecutively, maximum tracer concentration was reached at $\bar{t}_m \approx$ 22 s and the tracer disappeared after a long time (from $\approx$ 7 – 120 s).

The longer tracer disappearing time resulted in RTD profiles shifting to the right which is consistent with improved binder distribution with inclusion of KE in the screw configuration in region I, (see Figure 7-10). This spread in the RTD profile is attributed to a decrease in conveying rate (reduction in p) which caused an increase in the $\bar{t}_m$ of the material inside the granulator, (see Table 7-3 and Figure 7-10). Thus, longer RT's were effective in sufficiently mixing the solid and liquid binder when using KE in region I.

Moreover, the higher value of $\Psi \approx$ 39 % in region I demonstrates that there is material back mixing which occurs continuously within the KE zone, giving the material more chances to be fragmented, compacted and stretched as indicated by the elongated granule structure, resulting in a decrease in the inherent intragranular porosity ($\varepsilon \approx$ 12 %), (see Table 7-3). The increase in material back mixing resulted in the KE's operating in a 'more' partially filled screw level, (see Table 7-3). This screw fill level promotes backflow which is transmitted from the disc-disc and disc-barrel gaps. This flow mechanism of the KE's encourages better mixing, reducing the mass of < 150 μm granules produced significantly in region I, (see Figure 7-7).

With lower W_A in region II, narrow RTD profiles were produced resulting in shorter $\bar{t}_m \approx$ 13.7 s, (see Figure 7-10). In absolute values, the $\bar{t}_m$ of KE is approximately $\approx$ 37% more than that of the conveying-type elements. The short $\bar{t}_m$ indicates that the KE's have a positive conveying capacity (p = 0.590) which caused the material to be quickly conveyed out of the TSG. It is suggested that the positive conveying capacity indicates that the TSG was not highly

compacted which therefore explains the significant presence of < 150 µm granules, clearly reflecting a decrease in the mixing performance of the KE.

Along with the KE staggering angle, the short width of the KE's used in this work was not sufficient to produce strong back mixing of material which is required to dissipate the high interfacial energy between the solid and liquid binder in region II. As a result, the $\bar{t}_m$, percentage of < 150 µm granules and intragranular porosity like those reported for fCE are produced in region I when using KE's.

However, the higher a value of $\Psi \approx 31$ % indicates some increase in stress which resulted in some improvement of the liquid binder distribution when using KE's rather than the fCE's in region II, (see Figure 7-9 and Table 7-3). This means that further improvement of liquid distribution requires a coupling between increased $\bar{t}_m$ and φ in region II. Clearly, the KE's are not capable of distributive mixing at short length for region II. These result are in contrast to previous research, where it was reported that short KE lengths were adequate in distributing the liquid binder through granule fragmentation mechanism [74,75,78,115].

7.6 Tooth Mixing Elements (TME's)

The prominent findings of the granulation behavior of region I and region II are summarized in Tables 7-4 - 7-5. In region I the inclusion of TME's in the screw configuration resulted in increased agglomeration with fewer < 150 µm granules in the final batches, (see Figure 7-7 and Tables 7-3 - 7.4). However, in region II the reduction in the mass of < 150 µm granules showed a stronger dependency on the TME-type, where fewer < 150 µm granules are observed for wTME than for the nTME's, (see Figure 7-7 and Tables 7-3 - 7-5).

Although, the TME-types have similar geometries, the wider angular cut of the w-TME's provides more cross-sectional V_{free} for granules to be compacted. The compaction was sufficient to squeeze the liquid binder to the outer granular surface, which provided a greater chance for further agglomeration, resulting in increased granule size and reduction of < 150 µm granules for region I and II, (see Figures 7-7 - 7-8).

Table 7-4. A summary of the granulation results were the ε, $\bar{t}_m$ and a shown were obtained at optimal L/S for Region I

Screw Type	< 150 μm granules	ε	$\bar{t}_m$	Ψ	p	Screw Fill State
CE	≈ 52-62 % (low L/S), ≈ 31-53 % (opt L/S)	≈ 44 %	≈ 8.5 s	≈ 7.2 %	≈ 0.739	Starved
fCE	≈ 47-62 %(low L/S), ≈ 25-54 % (opt L/S)	≈ 28 %	≈ 9.9 s	≈ 8.0 %	≈ 0.651	Partially Filled
ICE	≈ 43-55 %(low L/S), ≈ 20-39 % (opt L/S)	≈ 24 %	≈ 10 s	≈ 24 %	≈ 0.584	Partially Filled
KE	≈ 30-47 % (low L/S), ≈ 7-12 % (opt L/S)	≈ 12 %	≈ 22 s	≈ 39 %	≈ 0.180	Partially Filled
nTME	≈ 14-27 % (low L/S), ≈ 3-7 % (opt L/S)	≈ 30 %	≈ 39 s	≈ 56 %	≈ 0.132	Fully ('almost'Completely) Filled
wTME	≈ 10-17 % (low L/S), ≈ 2-6 % (opt L/S)	≈ 31 %	≈ 61 s	≈ 38 %	≈ 0.209	Fully ('almost'Completely) Filled

Table 7-5. A summary of the granulation results were the ε, RT and a shown were obtained at optimal L/S for Region II

Screw Type	< 150 μm granules	ε	$\bar{t}_m$	Ψ	p	Screw Fill State
CE	≈ 83-95 % (low L/S), ≈ 81-95 % (opt L/S)	≈ 65 %	≈ 9.9 s	≈ 6.3 %	≈ 0.701	Starved
fCE	≈ 79-92 % (low L/S), ≈ 75-92 % (opt L/S)	≈ 35 %	≈ 9 s	≈ 7.5 %	≈ 0.695	Partially Filled
ICE	≈ 73-90 % (low L/S), ≈ 61-89 % (opt L/S)	≈ 25 %	≈ 10 s	≈ 15 %	≈ 0.515	Partially Filled
KE	≈ 58-92 % (low L/S), ≈ 47-94 % (opt L/S)	≈ 27 %	≈ 13.7 s	≈ 31 %	≈ 0.590	Partially Filled
nTME	≈ 27-47 % (low L/S), ≈ 14-25 % (opt L/S)	≈ 19 %	≈ 31 s	≈ 53 %	≈ 0.183	Fully (Completely) Filled
wTME	≈ 23-31 % (low L/S), ≈ 10-14 % (opt L/S)	≈ 21 %	≈ 42 s	≈ 79 %	≈ 0.141	Fully (Completely) Filled

The reduction of < 150 μm granules with inclusion of TME-type is in contrast with Thompson et al. (2010) were an increase in smaller sized granules and fines in the final batches was observed [75]. This result is attributed to the low compressive stresses exerted by the different TME-type used in their work which were not sufficient to produce strong enough granules that could withstand fragmentation in the cutting region of the screw elements inside the barrel. However, in agreement with the results reported in this work, Djuric et al. [74] reported that the TME-type led to granules that were less friable than those produced by CE-type as observed with decrease in intragranular porosity results, (see Table 7-2 - 7-3).

Table 7-3 illustrates the $\bar{t}_m$ for the nTME's and wTME's, which represent a significant increase in $\bar{t}_m$ in region I compared to the $\bar{t}_m$ from the CE-type and KE's. Clearly, good mixing in this region occurs in both states, 'more' partially filled (KE) and 'more' filled (TME-type), which is indicated by the improved liquid distribution across the granule size classes, (see Figure 7-9). The resulting broad spread of the RTD profiles and low p from the TME-types, (see Figure 7-10 and Table 7-3) also implies that cross-sectional mixing is increased in region I.

Most interesting is that the shape and spread of the RTD curve does not change significantly by changing the screw configuration from KE to TME-types in region I, (see Figure 7-10). This result is attributed to the screw elements operating in a 'more 'filled state which causes their mixing performance to be strongly dependent on the material volume flow. However, Table 7-3 shows that KE disc are 'more' partially filled whilst the TME-type operate in a 'more' filled state. This means that mixing in region I is not strongly dependent on the material volume flow through the screw geometry but rather on its wetting properties where maximum stress threshold exists which can be exerted on a material before the particles begin to rearrange themselves through the fragmentation mechanism.

This observation is illustrated in Tables 7-3 - 7-5 were the inherent intragranular porosity decreases from CE-type to KE. However, with inclusion of TME-type the porosity begins to increase due to increase in granules being cut by the screw elements. The granule cutting is indicated by the presence of large voids in the granule, (see Table 7-3). Therefore, it is plausible to conclude that there is a stress threshold between KE and nTME's where improved liquid binder distribution and decrease in the inherent intragranular porosity is observed, (see Table 7-3). However, between nTME's and wTME's, the porosity increases and granules size

decreases due to increase in the granules being cut by the screw elements. This causes particles to rearrange themselves because of the dominance of the fragmentation mechanism.

For region II, the $\bar{t}_m$ was found to be ≈ 31 s and ≈ 42 s for nTME's and wTME's respectively, (see Figure 7-10 and Table 7-3). Consequently, the spread of the RTD profile increased significantly. The significant differences in the RTD profiles of KE and TME-type in region II is because in comparison to the KE's, the TME-type are placed in the direction perpendicular to positive material flow. This guarantees that the material flows backwards through the intermeshing gap and mixes with other material in the screw channel.

With increased Ψ, material forward conveying rate is decreased reducing the inherent throughput as reflected by the low p values and increased $\bar{t}_m$ as less material volume is displaced per unit time. The material Ψ through the screw geometry results in the TME-type operating in a 'more' filled state, (see Table 7-3), resulting in increased agglomeration and fewer < 150 μm granules for region II.

With a decrease in W_A the interfacial tension plays a role in defining the extent of mixing. For the TME-type elements the increasing material Ψ results in increased interfacial tension dissipation due to increased material shearing caused by the strong back mixing driven flow. Clearly, the RTD profiles were determined by mass flow rates along the screws which are more a consequence of the screw geometry. However, due to higher $\bar{t}_m$ the 'more' filled zones contribute more to mixing than the starved and partially filled zones in region II.

The broader tail of RTD curves and low p values indicates that the material is passing for a longer time inside the extruder and consequently the mixing quality increases whilst the intragranular porosity decreases, (see Table 7-3). It therefore seems that the TME-type increase cross-sectional mixing across the barrel width and the volume of non-mixed regions are significantly reduced by the increased material back mixing, (see Figure 7-10 and Table 7-3). Thus, it is concluded that in region II the TME-types are capable of distributive and dispersive mixing by adjusting their angular cut due to improved liquid binder distribution and granule growth observed.

7.7 Conclusions

This study examined the influence of various screw element types on the wetting and nucleation stage in TSG to gain new understanding of the role their characteristic mixing behaviors play in the reduction of < 150 μm granules when using hydrophilic/hydrophobic powders and rationalize the positioning of the various screw elements along the barrel by studying the granule size, granule porosity, liquid binder and residence time distribution results.

The main observations and conclusions described in Chapter 7 are highlighted below:

- The increase in the axial cuttings through the screw flights of the conveying-type elements achieved a partially filled screw level. However, this state did not significantly improve the liquid distribution resulting in the formation of a large percentage of < 150 μm granules in region I and II which display characteristic hydrophobic (low W_A) and hydrophilic (high $W_{A)}$ wetting behavior.

- In region I, the mixing did not show a strong dependency on the screw fill levels (states) of KE's and TME-type as it was improved in both 'more' partially and 'more' filled screw states resulting in a decrease in the < 150 μm granules produced.

- Furthermore, improved mixing due to higher residence times was observed, although this led to granules with increased porosities due to increased granule voids from screw elements cuttings. These results indicate that there is a stress threshold which can be exerted on materials in region I before the particles begin to rearrange themselves through fragmentation mechanism.

- The KE's did not have a significant effect in improving liquid binder distribution in region II. Based on these observations, it is concluded that KE's should not be placed in the first mixing zone after the liquid injection point in TSG when using hydrophilic/hydrophobic mixtures, as these were shown not to be capable of achieving sufficient liquid binder distribution, required to produce uniform granules that are essential for improved product quality.

- In contrast, the significantly improved binder distribution observed in the TME-type elements that resulted in fewer < 150 μm granules and stronger consolidated agglomerates demonstrates that depending on their angular cut, these elements can be used for distributive and dispersive mixing of solids and liquids to achieve sufficient homogenization, fragmentation and consolidation.

This work underlines the importance of screw element selection and placement which play an important role in controlling the resultant granule properties when using problematic formulations. However, there is a need to investigate the contribution of the various elements in particle segregation behavior in TSG in order to provide knowledge to industry with how to enable effective process design and control.

8 ASSESSING PARTICLE SEGREGATION USING NEAR-INFRARED CHEMICAL IMAGING IN TSG

8.1 Introduction

Segregation during granulation is a common problem which occurs when particles with different physical properties (size, density, shape, flowability, wettability) in a mixture separate from their homogeneous state [116]. This phenomenon occurs in competition with mixing, affecting final product content uniformity [117].

In wet granulation, the research on particle segregation has thus far focused on the effects of powder wetting properties and process parameters in batch granulation (high shear). In a batch high shear mixer, the granulation mechanisms function through frequent particle-particle collisions created by fast impeller speed, followed by consolidation and growth in a large volume bowl (1 to 600 L) [113,118]. The large volume makes it difficult to control the granulation process resulting in high variability in mixing [119,120]. This consequently promotes particle segregation, impacting onward processing and the content uniformity of the final product [121].

TSG is considered a much better alternative to batch high shear granulation due to its small internal free volume ($\sim$ 300 mL) which makes the material being processed experience the same environment at steady state. Also, the material typically spends a small amount of time in a single unit operation, reducing the opportunity for unlike particles to become disassociated. It is postulated that these advantages will produce robust granules with lower variability and segregation potential, this will be explored in the following sections.

TSG is a regime separated process with the granulation mechanisms occurring one after the other along the length of the barrel channel [5]. This complexity of the TSG system requires fundamental understanding on how particle segregation along the barrel length contributes to dominant granule formation mechanisms affecting content uniformity in final granular product.

Traditional methods of assessing particle segregation are based on determining the fraction of particles in bulk mixtures. This is typically achieved using wet chemical analysis e.g. high-performance liquid chromatography, mass spectrometry, dissolution tests etc. or by measuring bulk properties of mixtures using electrical and thermal conductivity [96,117]. However, these

techniques are destructive, very time consuming and are not applicable to a wide range of materials.

Near-Infrared Spectroscopy (NIRS) has gained wide acceptance in many industries, especially in the pharmaceutical industry for assessing particle segregation either online or offline at different stages of the manufacturing process i.e. blending, granulation, tableting, coating etc. [122,123]. This is due to its advantages as a fast, non-destructive and non-invasive technique which offers reliable quantification for a wide range of materials. Despite the above-mentioned benefits, NIRS does not offer visual insight into the internal structure and spatial allocation of single components in the final product.

Recent advancements in NIR technologies has made it possible to acquire hyperspectral images using Near-Infrared Chemical Imaging (NIR-CI) technique. NIR-CI permits samples to be analyzed on a micro-level scale, thus allowing for the identification of single components within a sample. Moreover with NIR-CI, samples are characterized with simplicity, speed and improved spatial and spectral resolution [124–127]. In the pharmaceutical industry, this technique is used in process analysis, quality control and product evaluation in order to gain greater process understanding and to identify manufacturing problems which can lead to final product rejection [121,125,127–130]. This technique can also be used in-line for real time release of the drug product and to automatically adjust the process parameters in order to maintain the product quality attributes within specification limits.

In TSG, most of the studies have successfully utilized NIR-CI to characterize liquid distribution homogeneity by analyzing moisture content and material residence time [126,129,131]. Here, NIR-CI is employed to investigate how mixing in different TSG compartments when varying screw configuration and liquid binder viscosity affects particle segregation in the resultant granules when using two-component mixtures. The experimental results were interpreted by means of fundamental granulation mechanisms taking place inside the TSG to improve understanding of granule segregation related problems in the pharmaceutical industry. Examination of the data showed a direct correlation between dispersion due to shear force and de-mixing of particles, which allowed for identification of fundamental granule formation mechanisms affecting content uniformity in final granules from TSG. A regime map of particle segregation behavior is proposed, which links de-mixing potential to controlling granulation mechanisms with a new dimensionless mixing number. The

regime map serves as a useful tool to understand how to enable effective formulation development, adequate process design and control in TSG.

8.2 Experimental Design

Two-component mixture of coarser Lactose 200M ($\phi = 0.74$) with fine Magnesium Stearate (MgSt) ($1 - \phi = 0.26$) was selected for the current study, as the critical surface coverage volume fraction for this mixture was found to be $\phi_c \approx 0.70$, were the lactose particle is completely covered by the small magnesium stearate particles (see Chapter 5.5). The liquid binder was comprised of 0 wt%, 2.5 wt%, 5 wt% HPC with µ: 1.00 m Pa s, 3.10 m Pa s and 9.40 m Pa s respectively. A quinoline yellow dye E104 (Fiori Colori, Italy) 1 g was added to the liquid binder to assist with the visual observations of the granule structure. The granulation experiments were carried out using the granulation equipment detailed in Chapter 3.2.2. The mixing along the TSG barrel was examined by separating its length into different zones as shown in Figure 8-1.

		Material in	Liquid in	CE		Zone 1
	Material in	Liquid in	CE	ICE		Zone 2
Material in	Liquid in	CE	ICE	KE		Zone 3
Material in	Liquid in	CE	ICE	KE	nTME	Zone 4
Material in	Liquid in	CE	ICE	KE	nTME	wTME	Zone 5
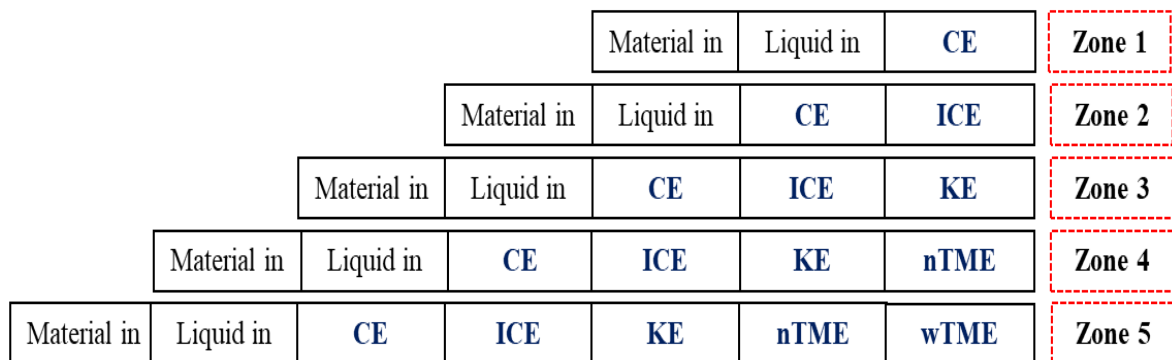
Figure 8-1. Schematic diagram of the TSG configuration.

Based on the experimental findings detailed in Chapter 7, initially the conveying elements (CE) were placed in the wetting and nucleation Zone 1. The large cut conveying elements (lCE's) were placed in Zone 2, which is after the wetting zone, in order to compress material and achieve a higher degree of fill before the mixing zone, both of which are required to promote better mixing. The first mixing zone is in Zone 3 which consists of kneading elements (KE's) to distribute the solid and liquid binder along the length of the screw. Material then enters Zone 4, which consists of narrow tooth mixing elements (nTME's) where it is further mixed. Downstream in Zone 5, the wide tooth mixing elements (wTME's) were placed. The nTME's and wTME's are effective in applying a combination of both shear and compressive

stresses, which promote dispersive mixing. Each zone is separated by CE's, to relieve stress build up from the mixing zones. This ensures that the torque does not become increasingly large and the material does not jam. The granules collected were measured for compositional analysis using the NIR-CI method detailed in Chapter 3.3.7.

8.3 Zone 1: Wetting and Nucleation

Figure 8-2 shows the compositional analysis results across different granule size classes taken from the initial wetting and nucleation Zone 1. The compositional analysis results are presented based on magnesium stearate (fine particle) content i.e. assay homogeneity. Here, the magnesium stearate composition is referred to as fine particle composition. In Figure 8-2, the solid lines indicate the theoretical fine particle composition based on the initial formulation composition used in this study and the resultant fine particle composition across different granule size classes is represented by the symbols.

Figure 8-2. Zone 1 Compositional analysis results across different granule size classes for μ: ● 1.00 m Pa s, ● 3.10 m Pa s and ● 9.40 m Pa s. The resultant granule images are also shown.

The fine particle distribution across different granule size classes reveals a clear trend (see Figure 8-2). In smaller granule size classes (150 - 425 μm), these granules are observed to be

super potent in fine particle composition. However, the larger granule size classes (425 - 1700 µm) are observed to be sub-potent in fine particle composition.

The observed trend in fine particle distribution across the granule size classes is attributed to the presence of fine particles i.e. hydrophobic which led to preferential wetting of coarse hydrophilic particles by immersion nucleation. Immersion nucleation is when powder particles are captured on the surface of a liquid binder droplet and are subsequently immersed due to the larger droplet to primary particle ratio [55].

By contrast, Scott et al. [132] reported that capillary forces act to engulf the primary particles into the liquid droplet binder and increase with decreasing particle size, which should lead to preferential wetting of fine particles. Here, preferential wetting and nucleation of coarse particles is driven by a competition between capillary forces and interfacial effects whereby the high interfacial energy at the solid/liquid contact area acts to prevent engulfment of fine particles at low viscosity. This then induced uneven distribution of these particles which resulted in all granule sizes having less than the expected composition of fine particles at low viscosity, (see Figure 8-2). These results indicate that there was a greater tendency for fine particles to segregate from the coarse particles. This tendency produced granules which were more porous in structure, as shown by the clear voids in the internal structure of the granules, (see Table 8-1).

From the internal granule structure i.e. x-ray images, there are two distinct regions that can be observed: the inner core and the outer shell, (see Table 8-1). In the inner core, the coarse particles are held tightly together with fine particles, which are loosely held being on the outer shell of the granule. The differences in the core and outer granule shell demonstrate that the coarse particles are preferentially wetted whilst fine particles adhere to the granule core through a mechanism of growth by layering, (see Table 8-1). The fact that layering is observed in this zone, it implies that powder-binder interactions are the driving force behind agglomeration in Zone 1 which is in line with literature [111].

The composition of the fine particles on the granule shell increased with viscosity, which allowed the yield of the large granules to increase (see, Figures 8-3 - 8-5). This increase in yield is linked to the viscosity of the binder in which the viscous flow retardation reduces the effect of capillary and interfacial forces, thereby slowing down the stages of nuclei formation (liquid penetration and spreading). This then leaves a layer of liquid binder available for growth

by layering. The reduced mobility of the nuclei formation kinetics resulted in initial nucleation by solid spreading, where the fine particles initially spread around the exterior of the liquid drop, forming a liquid marble, (see images in Figure 8-2). This was followed by forced nucleation by immersion as the liquid marble experienced deformation due to shear forces inside the TSG. It is suggested that when using low viscous binders, these nucleation steps occur at a faster rate making it difficult to capture them.

Table 8-1. NIR hyperspectral and X-rays images for granules in Zone 1

Binder Viscosity (m Pa s)	NIR Chart (%)	Granule Size			
		150- 212 μm	600 – 850 μm	1800 – 1700 μm	1800 – 1700 μm X-ray
1.00		cv 16±0.90	cv 22±0.35	cv 18±0.43	
3.10		cv 14±0.81	cv 14±0.60	cv 12±0.34	
9.40		cv 11±0.93	cv 15±0.75	cv 15±0.68	

Figure 8-3. Granule yield for different size classes for 1.00 m Pa s.
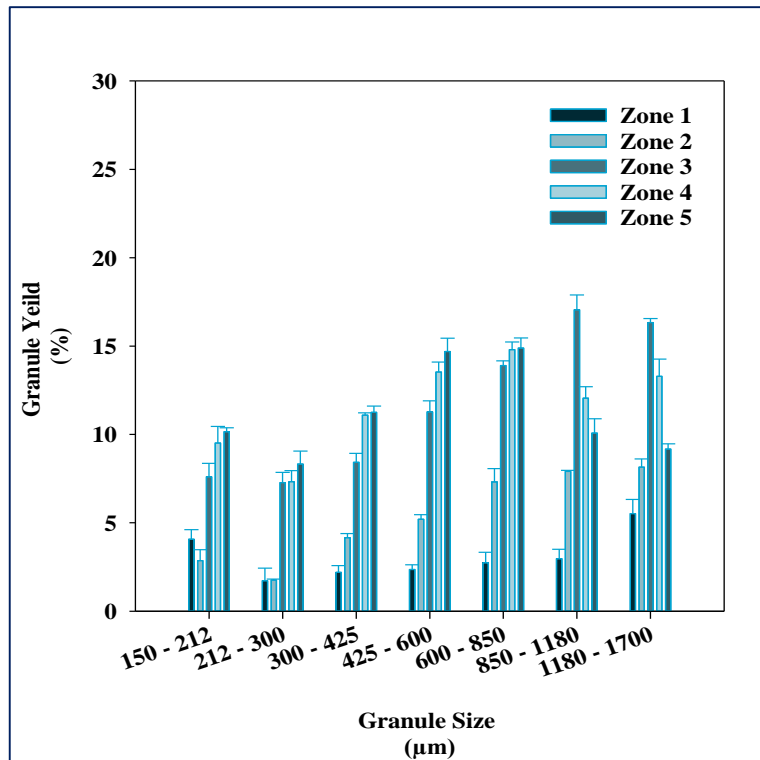
Figure 8-4. Granule yield for different size classes for 3.10 m Pa s.

143
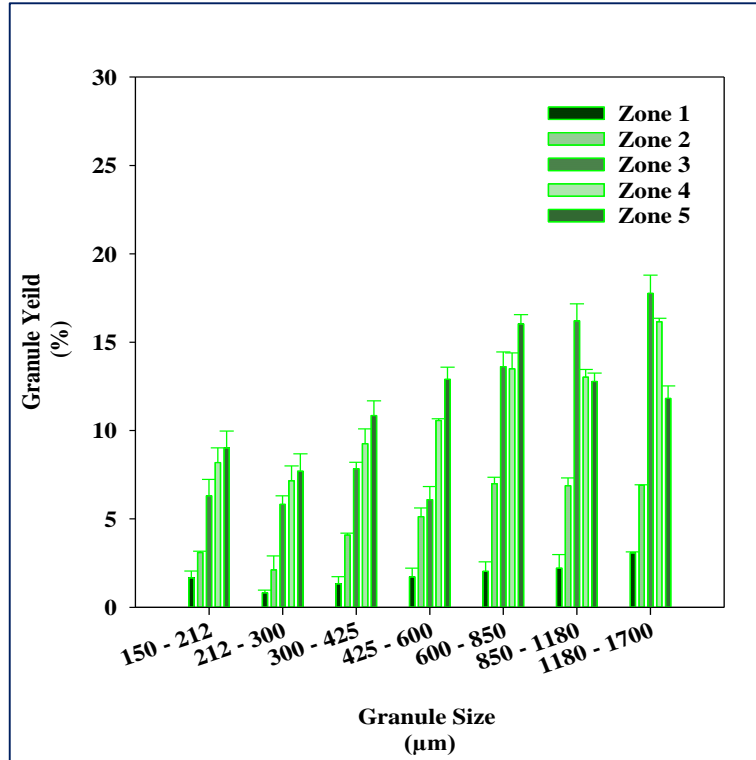
Figure 8-5. Granule yield for different size classes 9.40 m Pa s.

The applied shear, forced the liquid binder to be pushed to the surface of the granule where, on the granule surface, more particles were picked up by layering mechanism. This is evident from the progressive increase in the composition of fine particles on the granule surface and formation of large and dense nuclei with increased viscosity, (see Figure 8-2 and Table 8-1). According to Eshtiaghi et al. [57]for liquid marbles to resist nucleation by immersion under applied shear, more hydrophobic formulations need to be used. Generally, there was an overall low granule yield and high fine particle variability (high cv) in granules produced from Zone 1, (see Figures 8-2 – 8-5 and Table 8-1). From these results, it can be seen that the CE's have an appreciable effect on particle segregation inside TSG, due to lower shear exerted by these elements. This lower shear minimizes the mixing, reducing the system capability to attain strong liquid binder and particle combinations under the conditions used.

8.4 Zone 2: Breakage

A breakage zone was introduced after the wetting and nucleation stage to facilitate primary granule breakage, which could make it easier to redistribute the liquid binder in a later mixing zone. The NIR-CI results of the fine particle composition as a function of granule size in the TSG breakage Zone 3 are shown in Figure 8-6 and Table 8-2.
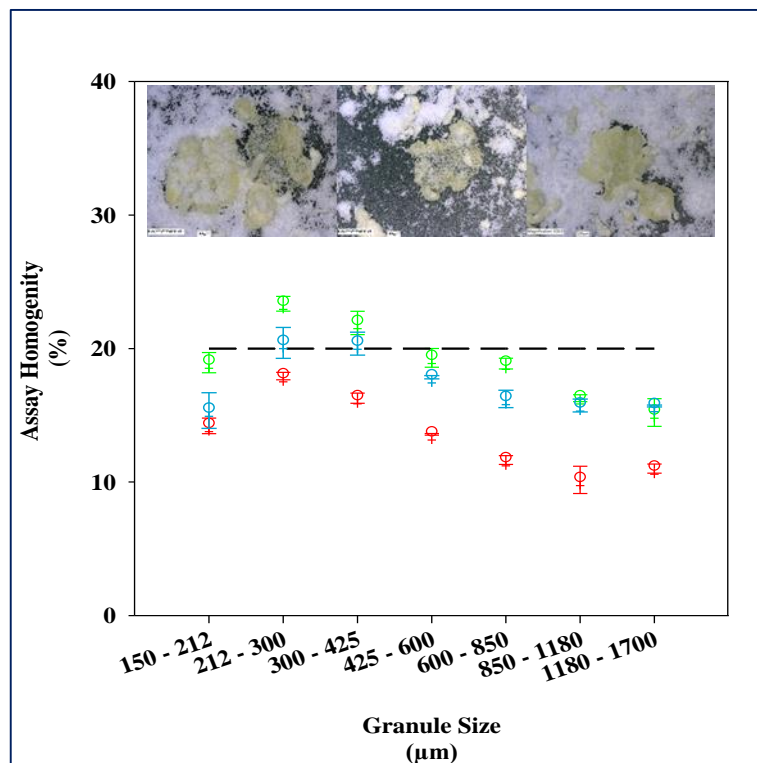
Figure 8-6. Zone 2 Compositional analysis results across different granule size classes for µ: ● 1.00 m Pa s, ● 3.10 m Pa s and ● 9.40 m Pa s. The resultant granule images are also shown.

Figure 8-6 and Table 8-2 shows that the span of the fine particle composition decreases in the breakage Zone 2. This observation is due to primary granules experiencing breakage driven increased shearing forces and by the reduced internal free volume, which increased the barrel fill level; thus promoting granule-granule and screw surface-granule collisions. It is suggested that during granule-granule collisions, particles segregate by abrasion where particles are transferred from one granule to another, whilst the screw surface-granule collisions cause particle segregation by chipping. The terms abrasion and chipping describe particle segregation by granule breakage mechanisms, which should result in significant variability in fine particle composition within the same granule size class due to the random manner at which these mechanisms occur. Figure 8-6 and Table 8-2 clearly confirm that this is indeed the case, especially for low viscous binders.

The high variability in fine particle composition within each granule size at low binder viscosity is due to low viscous binders producing granules with weaker liquid bridge strength. This makes the granules more susceptible to breakage under constant forces of agglomeration inside the TSG barrel, which led to a notable reduction in their yield (see Figure 8-3).

145

Table 8-2. NIR hyperspectral and X-rays images for granules in Zone 2

Binder Viscosity (m Pa s)	NIR Chart (%)	Granule Size			
		150- 212 μm	600 – 850 μm	1800 – 1700 μm	1800 – 1700 μm X-ray
1.00		cv 15±1.57	cv 20±1.43	cv 19±1.88	
3.10		cv 8.1±0.40	cv 8.0±0.63	cv 8.5±0.33	
9.40		cv 7.8±0.75	cv 7.0±0.90	cv 7.5±0.92	

Granule breakage left an internal core mainly consisting of coarse particles, which is indicated by the low fine particle composition in larger granules at low viscosities (see Figure 8-6 and Table 8-2). However, breakage caused more fine particles to accumulate in the smallest granules sizes, increasing the fine particle composition in these granules and clearly demonstrating particle segregation behavior, (see Table 8-2). Thus, granule breakage does not contribute to uniform particle distribution but leads to granules with a porous structure, (see Table 8-2). When more viscous binders were introduced, an increase in the granule yield was observed, (see Figures 8-4 - 8-5). This increase in granule yield is associated with viscous drag reducing particle rearrangement whilst encouraging further growth by layering to a significant degree on the granular surface. The granule growth led to an increase in fine particle

composition in larger granules (425 -1700 µm), (see Figure.8-6). These findings imply that more viscous binders reduced the rate at which granule breakage was occurring because granules formed by viscous binders have stronger bonds to withstand breakage. The lower breakage rates when using more viscous binders minimized the random manner at which breakage and distribution of solid particles occurred. This resulted in significantly reduced fine particle variability in each granule size class (see Table 8-2). However, the reduced mobility of particles did not promote uniform distribution of particles as seen from the images, which reveal scattering of fine particles on the granular surface (see Table 8-2). This is because viscous binders require greater amounts of energy to be redistributed sufficiently and to increase granule homogeneity, which the lCE were not able to provide.

8.5   Zone 3-5: Growth

Figure 8-7 shows the evolution of the fine particle composition across different granule size classes in the initial mixing Zone 3. The composition of the fine particles on the granule surface increased for small sized granules (150 - 425 µm) which corresponded to increased yield of granules (see Figures 8-3 and 8-7).
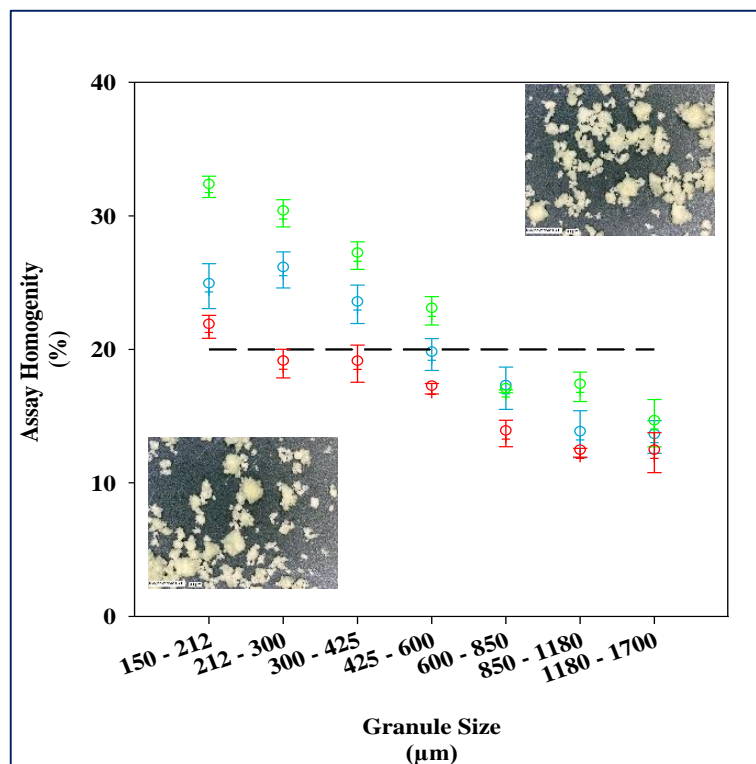
Figure 8-7. Zone 3 Compositional analysis results across different granule size classes for µ: ● 1.00 m Pa s, ● 3.10 m Pa s and ● 9.40 m Pa s. The resultant granule images are also shown.

147

Table 8-3. NIR hyperspectral and X-rays images for granules in Zone 3

Binder Viscosity	NIR Chart (%)	Granule Size			
		150 – 212 µm	600 – 850 µm	1800 – 1700 µm	1800 – 1700 µm X-ray
1.00		cv 10±1.2	cv 9.8±1.4	cv 7.0±0.70	
3.10		cv 7.2±1.0	cv 7.8±0.70	cv 7.7±0.30	
9.40		cv 7.4±0.35	cv 7.6±0.55	cv 7.8±0.60	

In this zone, fine particles are picked up through particle's adhering to primary granules or small granules combining. This occurred as additional fluid becomes available due to the KE's facilitating the liquid binder to be squeezed to the outer granule surface, revealing a new surface for particles to stick too [115,133]. Most interestingly, with increased adherence and combination of granules, the fine particle variability within each granule size class decreased at low viscosity (see Table 8-3), whilst for more viscous binders it remained reduced. Although it was expected that the slow penetration behavior of more viscous binders would reduce the granule growth rate, the use of more viscous binders led to a system that displayed increased granule growth behavior (see Figures 8-4 - 8-5).
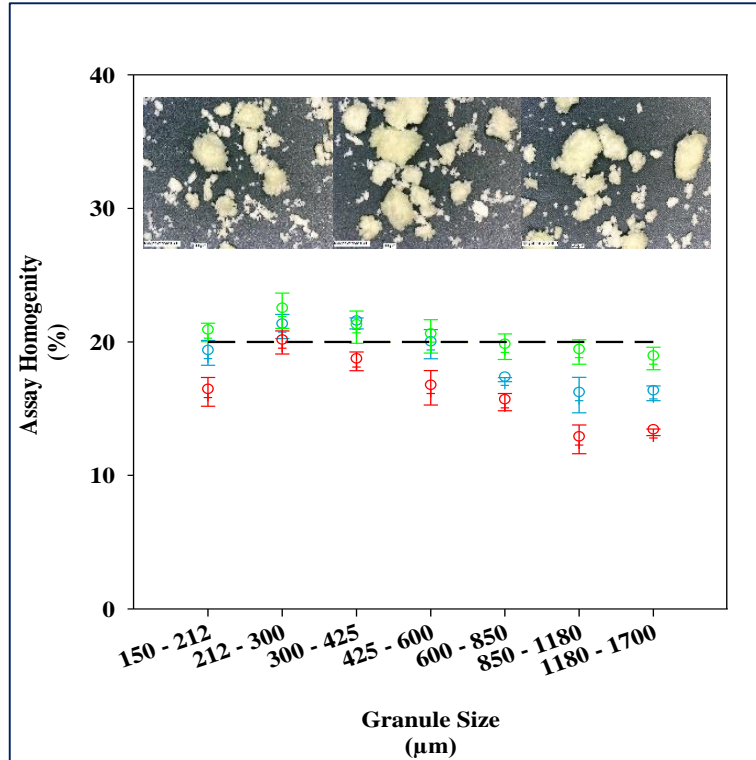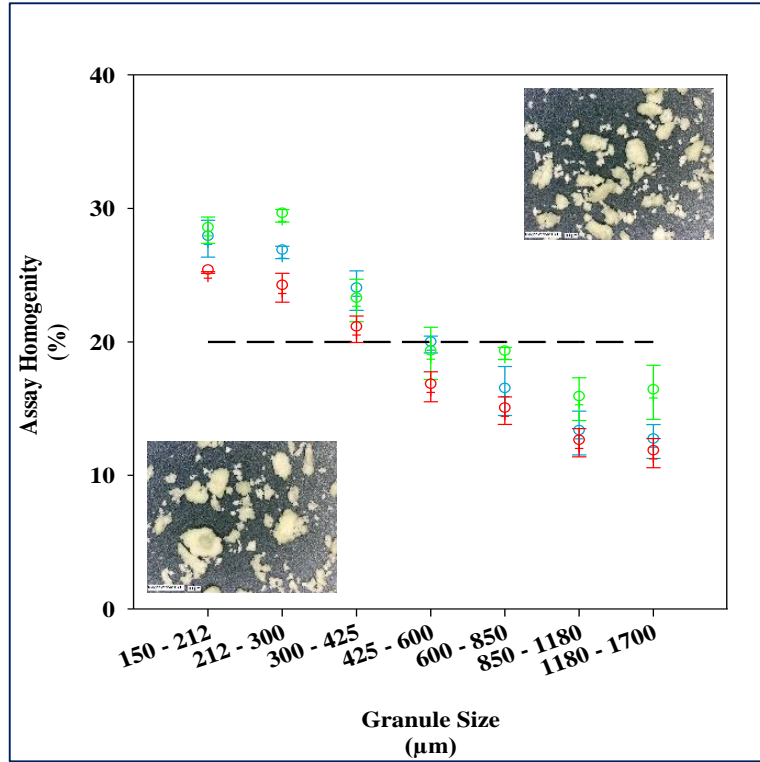
Figure 8-8. Zone 4 Compositional analysis results across different granule size classes for μ: ● 1.00 m Pa s, ● 3.10 m Pa s and ● 9.40 m Pa s. The resultant granule images are also shown.
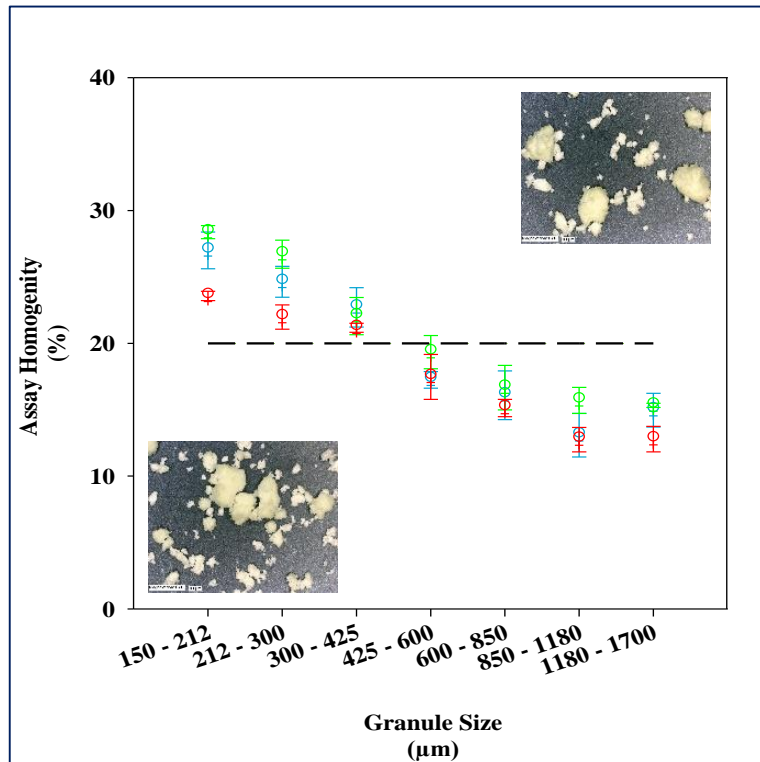
Figure 8-9. Zone 5 Compositional analysis results across different granule size classes for μ: ● 1.00 m Pa s, ● 3.10 m Pa s and ● 9.40 m Pa s. The resultant granule images are also shown.

This is due to the slow liquid droplet spreading behavior of viscous binders leaving a layer of liquid on the outer surface of granules for further agglomeration. It therefore appears that further particle adherence occurs through constant rewetting in Zone 3. In the subsequent mixing Zone 4-5, growth of granules size range 850 - 1700 μm was much slower due to continuous granule breakage with longer granulation section i.e. longer residence time (see Figures 8-3 - 8-5). Thus, there is a transition from growth to minimal granule growth behavior with longer granulation times in TSG. This indicates that in these zones, the material undergoes extensive shearing which breaks the larger granules down, reducing their yield.

Table 8-4. NIR hyperspectral and X-rays images for granules in Zone 4

Binder Viscosity (m Pa s)	NIR Chart (%)	Granule Size			
		150 – 212 μm	600 – 850 μm	1800 – 1700 μm	1800 – 1700 μm X-ray
1.00		cv 5.6±0.68	cv 7.7±0.74	cv 8.0±1.2	
3.10		cv 4.8±0.54	cv 6.4±0.4	cv 6.5±0.7	
9.40		cv 5.2±0.23	cv 5.78±0.4	cv 5.55±0.32	

Interestingly, even with the increased granule breakage, the number of un-granulated fines decreased significantly. This finding implies that in addition to breakage there is simultaneous

consolidation taking place inside TSG. The presence of granule consolidation is evident from the general trend in the granule structure changing from porous to tightly packed as material moves through Zones 1-5, (see Table 8-1 - 8-5). In practice this means that breakage of larger granules created granule fragments which underwent further consolidation with available small granules, increasing the yield of these granules (150 - 850 μm), (see Figure 8-3 - 8-5).

Table 8-5. NIR hyperspectral and X-rays images for granules in Zone 5

Binder Viscosity (m Pa s)	NIR Chart (%)	Granule Size			
		150 – 212 μm	600 – 850 μm	1800 – 1700 μm	1800 – 1700 μm X-ray
1.00		cv 4.32±0.47	cv 4.67±0.2	cv 5.2±0.3	
3.10		cv 4.93±0.45	cv 4.42±0.27	cv 4.80±0.67	
9.40		cv 5.25±0.88	cv 5.48±0.38	cv 5.98±0.77	

In Figures 8-8 - 8-9, the increased granule breakage and consolidation is shown to have resulted in a significant reduction in the fine particle variability (see Table 8-4 - 8-5), which

implies a narrowing of the span of the particle distribution in individual granule size classes with increase in dispersion due to shear force. The fine particle distribution across granule size classes in Zone 4 - 5 resemble each other, (see Figures 8-8 - 8-9). This similarity shows a significant step-wise trend occurring around mean granule size range of 425 - 600 μm, with smaller granules having relatively higher fine particle composition in comparison to the larger granules. The step-wise trend of fine particle distribution reveals a degree of reliance on fine particle distribution on dispersion by shear force. This reliance can be explained by taking into consideration the events happening in the mixing zones of TSG.

As shown, in Zone 3 the kneading action caused more liquid to become available on the granule surface, thereby promoting granule growth through coalescence and consolidation; hence the granule yield of larger granules improved (see Figures 8-3 - 8-5 and 8-7). It is suggested that shear forces exerted in Zone 3 allowed for the critical liquid binder level on the granular surface to be reached. When more shearing forces were applied in Zone 4 - 5, this then led to a partitioning of larger granules having coarser particles and small granules having more fine particles (see Figure 8-8- 8-9).

These results suggest that particle segregation in Zone 4 - 5 occurred through dynamic dislodging mechanism of fine particles from the granule surface, resulting in the composition shifting from high to low with increase in granule size. The dislodging mechanism seems more probable due to the step-wise trend observed (see Figure 8-8 - 8-9) and is attributed to the increased barrel fill level of Zone 4 - 5 creating enhanced particle/particle or granule/granule collisions, which granule growth mechanism relies on.

Although these collisions are promoted, the consistent breakage of granules significantly reduce the success of these collisions which resulted in a decrease in the yield of larger granules (see Figure 8-3 - 8-5). This means that segregation essentially relies on the conditions under which colliding particles will stick together making the dynamic yield strength of the wet granules and dispersion due to applied shear force as the key factors which determine the survivability of granules under constant shearing when formed and the extent of particle distribution.

8.6 Mapping Approach: Particle Segregation

In the results presented, particles segregation in TSG is shown to be influenced by the length of the granulation section i.e. residence time, dispersion due to shear force from the screw elements, liquid binder viscous forces and saturation. Depending on these factors, different particle segregation mechanisms may dominate. To generalize the results presented in this paper with the aim of offering general guidance for a wider range of TSG systems, a particle segregation regime map is proposed. This links demixing potential (Equation 3-7), which essentially considers uniformity variations within a batch, and a dimensionless mixing number (DMN):

$$DMN = \frac{T}{V_{Free}} \times \frac{\bar{t}_m}{\mu}$$

Equation 8-1

Conceptually the DMN represents the effective mixing capability of the TSG linked with viscous dissipation. Figure 8-10 shows the results of the demixing potential plotted as a function of the characteristic DMN which were calculated for each TSG zone investigated. As can be seen, the demixing potential increases significantly at low DMN. This is because at low DMN, only a small amount of mechanical torque has been consumed during TSG mixing. The segregation mechanism in this stage is characterized by a preferential wetting of coarse particles followed by layering of the resultant nuclei (primary granules) by fine particles (Zone 1) and breakage of such nuclei to encourage further layering of fine particles (Zone 2). As the DMN increased, indicating that more mechanical torque is consumed in the system by mixing, the liquid binder was encouraged to be squeezed to the granule surface through a consolidation process and therefore more growth was promoted by coalescence in Zone 3. In the final mixing Zones 4-5, more aggressive mixing in the process caused the fine particles to be more dispersed throughout the granules rather than merely loosely sticking on the surface.
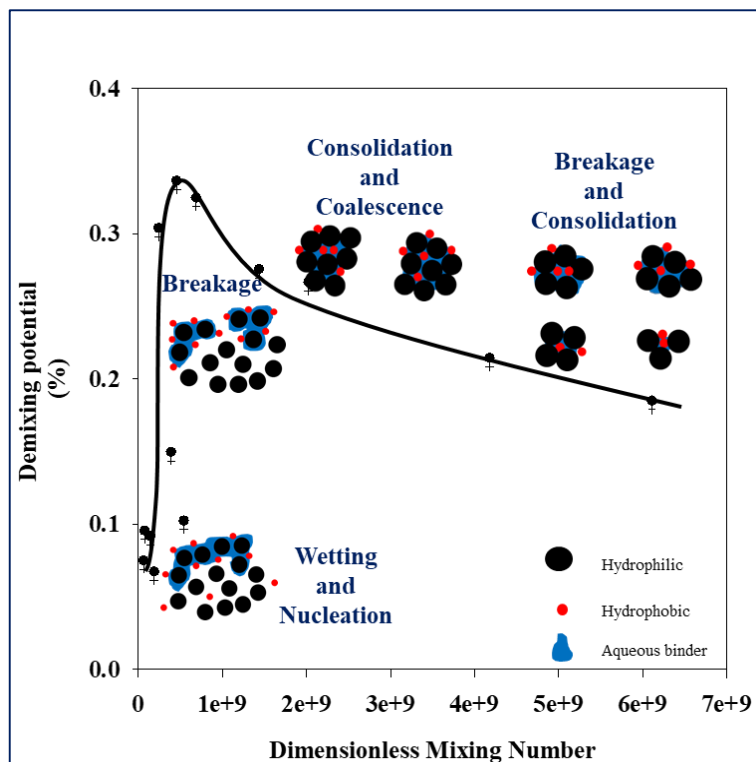
Figure 8-10. Proposed particle segregation map.

A further increase in the DMN means more mechanical torque in the system by mixing. Given that the potential of the liquid binder to result in more growth is already consumed in the consolidation and coalescence stage, the dominant mixing events occurring here are simultaneous breakage and consolidation (Zone 4-5). The breakage and consolidation mechanisms work to reduce the large size of granules formed from the consolidation and coalescence stage in Zone 3 and increase granule strength. This offers more granule size classes with well-mixed and compact fine and coarse particle content within the bulk final product. In an ideal TSG process, a low demixing potential is desirable to minimize particle segregation problems. The particle segregation regime map serves as a useful tool for understanding how particles segregate along the TSG barrel length as well as being a helpful tool in trouble-shooting the process.

8.7 Conclusion

In this study, a novel NIR-CI method to study particle segregation in granules from TSG was presented which is applicable for a wide range of formulations. The experiments performed considered the influence of liquid viscosity and TSG mixing characteristics i.e.

154

screw element which allowed for the identification of key segregation mechanisms affecting product uniformity of content.

The main observations and conclusions described in Chapter 8 are highlighted below:

- The key mechanisms dominating particle segregation were preferential wetting and nucleation and breakage which caused high variability in fine particle composition across different granule size classes.

- However, viscous forces acted to hinder capillary effects thereby minimizing particle movement reducing this variability especially with increased shear forces experienced by the material inside the granulator.

- The dispersion due to shear force was shown to have direct influence on particle distribution but also manifests to a regular decrease in yield of larger granules.

- Particle segregation behavior was linked to dispersion due to shear force through a proposed regime mapping approach to provide a general guideline of how particles segregate along the TSG barrel length.

It is believed that the discussions presented here will be useful for the pharmaceutical industry to better understand particle segregation phenomena in TSG when using hydrophobic product in order to optimize processes related to granule production and quality.

9   OVERALL THESIS CONCLUSIONS AND FUTURE WORK

The primary objective of this thesis was to improve understanding on how the initial interaction between the liquid binder and primary powder particles influence the granulation rate processes taking place in TSG when using a hydrophobic component in the formulation composition.

The initial work in this thesis detailed in Chapter 4 was focused on characterizing the static interaction between the liquid binder and primary powder particles. Two competing spreading mechanisms of single liquid droplets on a powder bed were identified: the d_h spreading and d_v imbibition. The d_h spreading describes the length the liquid droplet travels horizontally across the powder bed and is dominant when $0° < \theta^* < 60°$ where liquid movement is driven by capillary forces resulting in fast nucleation kinetics i.e. liquid binder droplet spreads and penetrate almost immediately into the powder bed. In contrast, the d_v imbibition is the length the liquid droplet travels vertically into the powder bed and is dominant when $60° < \theta^* < 140°$, where the wetting and nucleation kinetics are slow as liquid movement was found to be dependent on interfacial tension. Existing models that predict the d_h and d_v spreading behaviour were applied to experimental data and were unsuccessful in predicting the experimental behaviour. It is suggested that further investigations are needed to propose suitable d_h and d_v imbibition spreading theories.

Overall conclusions in Chapter 4 indicated that the powder wetting behaviour has the most significant influence on the two competing spreading mechanisms of a single liquid droplet. This led to thesis work progressing in two directions a) characterisation of the wetting behaviour and b) linking this behaviour to the resultant granule properties. In characterisation of the wetting behaviour, a new dimensionless surface coverage wetting model to predict the contact angle behaviour of two-component mixtures has been proposed, as the Cassie-Baxter theory that predicts the same was found to be inconsistent with experimental data. The key aspect of the model is the consideration of particle surface coverage and its relation to the contact angle behaviour. Chapter 5 presents the results from a series of experiments measuring the contact angle behaviour of different two-component mixtures and these results are compared with the model predictions. The surface coverage wetting model predicts a non-linear relationship between normalized cosine of the contact angle and the volume fraction of the components within a particulate mixture. Excellent agreement is found between the

experimental data and model predictions for a wide range of materials. The proposed model is expected to be valuable to particle wetting applications pertaining to various industries however, pragmatically, the model presented can of course be further enhanced by unifying it with the original Cassie-Baxter model.

The static powder bed behaviour was linked to 'real' granulation behaviour using two distinct mapping approaches that describe how a combination of powder properties and process variables affect the resultant granular properties. The first mapping approach, Chapter 6 investigated the influence of TSG process variables (screw configuration, screw placement) upon the resultant granule properties. This approach allows the granulation behaviour to be linked to powder wetting properties and TSG flow regimes using the specific mechanical energy (SME). A correlation between SME and the resultant granule properties i.e. extent of granule formation and strength is shown. This was shown to be directly related to the TSG mass hold-up levels, were at low SME levels, the TSG is observed to be operating in starved conditions i.e. low mass hold-up resulting in granules with reduced extent of granule formation and strength. However, the extent of granule formation and strength improved with increase in SME levels due to increase in TSG mass hold-up encouraging the material to spend more time in the barrel channel being mixed. The results presented in Chapter 6 are useful to TSG practise in the pharmaceutical industry since it was shown that the influence of powder wetting properties and process variables on the granulation behavior can be described by a single parameter, specific mechanical energy. However, it was concluded from this investigation that influence of various screw elements requires further exploration, in view that little attention has been given to the subject in literature especially in understanding how to systematically arrange the screw configuration in TSG.

There is a black box approach to the arrangement of the screw elements in the screw configuration in most of the work reported in the TSG area. In order to move beyond this 'black box approach', Chapter 7 attempts to rationalize the positioning of various screw elements along the TSG barrel length by studying the extent of granule formation 'yield', reduction in un-granulated fines and other critical product quality attributes e.g. strength, porosity, residence time distribution. A tentative approach to placing the screw elements in TSG is proposed. However, it was identified that there was need to investigate the contribution of the various elements in particle segregation behavior in TSG in order to provide knowledge to industry

with how to enable effective process design and control when using a hydrophobic component in the formulation composition.

In Chapter 7, a second mapping approach is presented which links a new Dimensionless Mixing Number (DMN), proposed to characterise the most important parameters in TSG which significantly affect particle segregation: residence time, torque, viscosity and free volume. This then allowed for the controlling mechanisms affecting particle segregation to be identified by employing NIR-CI. In the pharmaceutical industry, the NIR-CI may prove to be useful for rapid assessment of granules in pharmaceutical processing. From an industrial point of view, understanding the key granulation mechanisms affecting particle segregation in TSG will allow researchers to apply this knowledge and therefore design a more robust and predictable TSG process. Further research in this work would be to investigate TSG mixing behaviour by numerical simulation using discrete element method (DEM) to identify key interactions governing TSG powder flow regimes and how these influence its mixing behaviour when using different process variables and formulation compositions. This will provide a solid understanding on mixing in TSG in order to construct predictive analytical theories which have important implications in pharmaceutical research and development.

Further recommendations from this contribution:

- The nucleation ratio provided a meaningful insight into the resultant granulation behaviour, indicating its potential as a predictive tool for granule size. Currently no library of nucleation ratios exist, therefore further research is required for different powders and liquid binders. A model to predict nucleation ratio is also required. The main advantage of predicting the granule size in this way is the reduced cost of equipment and sample analysis time which are crucial components in pharmaceutical manufacturing.

10 LITERATURE CITIED

[1]   B.J. Ennis, G. Tardos, R. Pfeffer, A microlevel-based characterization of granulation phenomena, Powder Technol. 65 (1991) 257–272.

[2]   S.M. Iveson, J.D. Litster, K. Hapgood, B.J. Ennis, Nucleation, growth and breakage phenomena in agitated wet granulation processes: a review, Powder Technol. 117 (2001) 3–39.

[3]   K.P. Hapgood, B. Khanmohammadi, Granulation of hydrophobic powders, Powder Technol. 189 (2009) 253–262.

[4]   M. Jacob, Chapter 9 Granulation equipment, Handb. Powder Technol. 11 (2007) 417–476.

[5]   T.C. Seem, N.A. Rowson, A. Ingram, Z. Huang, S. Yu, M. de Matas, I. Gabbott, G.K. Reynolds, Twin screw granulation — A literature review, Powder Technol. 276 (2015) 89–102.

[6]   K.P. Hapgood, M.X.L. Tan, D.W.Y. Chow, A method to predict nuclei size distributions for use in models of wet granulation, Adv. Powder Technol. 20 (2009) 293–297.

[7]   K.P. Hapgood, L. Farber, J.N. Michaels, Agglomeration of hydrophobic powders via solid spreading nucleation, Powder Technol. 188 (2009) 248–254.

[8]   T. Young, An Essay on the Cohesion of Fluids, Philos. Trans. R. Soc. London. 95 (1805) 65–87.

[9]   R.N. Wenzel, Resistance of solid surfaces to wetting by water, Ind. Eng. Chem. 28 (1936) 988–994.

[10]   A.B.D. Cassie, S. Baxter, Wettability of porous surfaces, Trans. Faraday Soc. 40 (1944) 546. .

[11]   A.B.D. Cassie, Contact angles, Discuss. Faraday Soc. 3 (1948) 11.

[12]   P.G. de Gennes, Wetting: statics and dynamics, Rev. Mod. Phys. 57 (1985) 827–863.

[13]   H.Y. Erbil, The debate on the dependence of apparent contact angles on drop contact area or three-phase contact line: A review, Surf. Sci. Rep. 69 (2014) 325–365.

[14]   C.F. Lerk, A.J.M. Schoonen, J.T. Fell, Contact angles and wetting of pharmaceutical powders, J. Pharm. Sci. 65 (1976) 843–847.

[15]   W.-C. liao, J.L. Zatz, Critical Surface Tensions of Pharmaceutical Solids, J. Pharm. Sci. 68 (1979) 488–494.

[16]   M. Aulton, Michael E., Banks, Influence on the hydrophobicity of the powder mix on fluidised bed granulation, Int. Conf. Powder Technol. Pharm. (1979).

[17]   H.A.H. Mohammad, J.T. Fell, Contact angles of powder mixtures consisting of spherical particles, Int. J. Pharm. 11 (1982) 149–154.

[18]   D.C. Pease, The Significance of the Contact Angle in Relation to the Solid Surface, J. Phys. Chem. 49 (1945) 107–110.

[19]   L. Gao, T.J. McCarthy, How Wenzel and cassie were wrong., Langmuir. 23 (2007) 3762–5.

[20]   A. Marmur, Equilibrium contact angles: theory and measurement, Colloids Surfaces A Physicochem. Eng. Asp. 116 (1996) 55–61.

[21]   R. Tadmor, Line energy and the relation between advancing, receding, and Young contact angles, Langmuir. 20 (2004) 7659–7664.

[22]   P. Joos, P. Van Remoortere, M. Bracke, The kinetics of wetting in a capillary, J. Colloid Interface Sci. 136 (1990) 189–197. .

[23]   E.B. Dussan, On the Spreading of Liquids on Solid Surfaces: Static and Dynamic Contact Lines, Annu. Rev. Fluid Mech. 11 (1979) 371–400.

[24]   T.D. Blake, K.J. Ruschak, Wetting: Static and Dynamic Contact Lines BT - Liquid Film Coating: Scientific principles and their technological implications, in: S.F. Kistler, P.M. Schweizer (Eds.), Springer Netherlands, Dordrecht, 1997: pp. 63–97.

[25]   R. Rowe, Binder-substrate interactions in granulation: a theoretical approach based on surface free energy and polarity, Int. J. Pharm. 52 (1989) 149–154.

[26]   A. Jarray, V. Gerbaud, M. Hémati, Prediction of solid–binder affinity in dry and aqueous systems: Work of adhesion approach vs. ideal tensile strength approach, Powder Technol. 271 (2015) 61–75.

[27]   D.A. Bolleddula, A. Berchielli, A. Aliseda, Impact of a heterogeneous liquid droplet on a dry surface: application to the pharmaceutical industry., Adv. Colloid Interface Sci. 159 (2010) 144–59.

[28]   A. Khoufech, M. Benali, K. Saleh, Influence of liquid formulation and impact conditions on the coating of hydrophobic surfaces, Powder Technol. 270 (2015) 599–611.

[29]   D. Bonn, J. Eggers, J. Indekeu, J. Meunier, E. Rolley, Wetting and spreading, Rev. Mod. Phys. 81 (2009) 739–805.

[30]   L.H. Tanner, The spreading of silicone oil drops on horizontal surfaces, J. Phys. D. Appl. Phys. 12 (1979) 1473.

[31]   H. Haidara, B. Lebeau, C. Grzelakowski, L. Vonna, F. Biguenet, L. Vidal, Competitive spreading versus imbibition of polymer liquid drops in nanoporous membranes: Scaling behavior with viscosity, Langmuir. 24 (2008) 4209–4214.

[32]   C. Grzelakowski, D. Ben Jazia, B. Lebeau, L. Vonna, D. Dupuis, H. Haidara, On the Influence of Pore Structure on the Free-Imbibition of Sessile Drops into Nanoporous Substrates, Langmuir. 25 (2009) 5855–5860.

[33]   H.R. Charles-Williams, R. Wengeler, K. Flore, H. Feise, M.J. Hounslow, A.D. Salman, Granule nucleation and growth: Competing drop spreading and infiltration processes, Powder Technol. 206 (2011) 63–71.

[34]   A.M. Cazabat, S. Gerdes, M.P. Valignat, S. Villette, Dynamics of Wetting: From Theory to Experiment, Interface Sci. 5 (1997) 129–139.

[35]   E. Bormashenko, Why does the Cassie–Baxter equation apply?, Colloids Surfaces A Physicochem. Eng. Asp. 324 (2008) 47–50.

[36]   S. Mechkov, a M. Cazabat, G. Oshanin, Post-Tanner spreading of nematic droplets., J. Phys. Condens. Matter. 21 (2009) 464134.

[37]   H. Michael, S.D. W., Simple Approach for Spreading Dynamics of Polymeric Fluids, Macromol. Chem. Phys. 213 (2012) 654–665.

[38]   I. V Roisman, Dynamics of inertia dominated binary drop collisions, Phys. Fluids. 16 (2004) 3438–3449.

[39]   J. Fukai, Y. Shiiba, T. Yamamoto, O. Miyatake, D. Poulikakos, C.M. Megaridis, Z. Zhao, Wetting effects on the spreading of a liquid droplet surface : Experiment and modeling colliding with a flat, Phys. Fluids. 7 (1995) 236–247.

[40]   T. Mao, D.C.S. Kuhn, H. Tran, Spread and rebound of liquid droplets upon impact on flat surfaces, AIChE J. 43 (1997) 2169–2179.

[41]   R. Andrade, O. Skurtys, F. Osorio, Development of a new method to predict the maximum spread factor for shear thinning drops, J. Food Eng. 157 (2015) 70–76.

[42]   H. Park, W.W. Carr, J. Zhu, J.F. Morris, Single drop impaction on a solid surface, AIChE J. 49 (2003) 2461–2471.

[43]   H. Jones, Cooling, freezing and substrate impact of droplets formed by rotary atomization, J. Phys. D. Appl. Phys. 4 (1971) 1657.

[44]   T. Bennett, D. Poulikakos, Splat-quench solidification: estimating the maximum spreading of a droplet impacting a solid surface, J. Mater. Sci. 28 (1993) 963–970.

[45]   E.W. Collings, A.J. Markworth, J.K. McCoy, J.H. Saunders, Splat-quench solidification of freely falling liquid-metal drops by impact on a planar substrate, J. Mater. Sci. 25 (1990) 3677–3682.

[46]   S. Chandra, C.T. Avedisian, On the Collision of a Droplet with a Solid Surface, Proc. Math. Phys. Sci. 432 (1991) 13–41.

[47]   M. Pasandideh-Fard, Y.M. Qiao, S. Chandra, J. Mostaghimi, Capillary effects during droplet impact on a solid surface, Phys. Fluids. 8 (1996) 650.

[48]   R. Choudhury, J. Choi, S. Yang, Y.-J. Kim, D. Lee, Maximum spreading of liquid drop on various substrates with different wettabilities, Appl. Surf. Sci. 415 (2017) 149–154.

[49]   J. Madejski, Solidification of droplets on a cold surface, Int. J. Heat Mass Transf. 19

(1976) 1009–1013.

[50]   M. Pasandideh-Fard, Y.M. Qiao, S. Chandra, J. Mostaghimi, Capillary effects during droplet impact on a solid surface, Phys. Fluids. 8 (1996) 650–659.

[51]   C. Ukiwe, D.Y. Kwok, On the maximum spreading diameter of impacting droplets on well-prepared solid surfaces., Langmuir. 21 (2005) 666–73.

[52]   D.C. Vadillo, A. Soucemarianadin, C. Delattre, D.C.D. Roux, Dynamic contact angle effects onto the maximum drop impact spreading on solid surfaces, Phys. Fluids. 21 (2009) 122002.

[53]   B. Waldie, Growth mechanism and the dependence of granule size on drop size in fluidized-bed granulation, Chem. Eng. Sci. 46 (1991) 2781–2785.

[54]   S.. Schaafsma, P. Vonk, N.W.. Kossen, Fluid bed agglomeration with a narrow droplet size distribution, Int. J. Pharm. 193 (2000) 175–187.

[55]   T. Schæfer, C. Mathiesen, Melt pelletization in a high shear mixer. IX. Effects of binder particle size, Int. J. Pharm. 139 (1996) 139–148.

[56]   N. Eshtiaghi, J.S. Liu, W. Shen, K.P. Hapgood, Liquid marble formation: Spreading coefficients or kinetic energy?, Powder Technol. 196 (2009) 126–132.

[57]   N. Eshtiaghi, K.P. Hapgood, A quantitative framework for the formation of liquid marbles and hollow granules from hydrophobic powders, Powder Technol. 223 (2012) 65–76.

[58]   T.H. Nguyen, N. Eshtiaghi, K.P. Hapgood, W. Shen, An analysis of the thermodynamic conditions for solid powder particles spreading over liquid surface, Powder Technol. 201 (2010) 306–310.

[59]   M.J. Hounslow, M. Oullion, G.K. Reynolds, Kinetic models for granule nucleation by the immersion mechanism, Powder Technol. 189 (2009) 177–189.

[60]   K.P. Hapgood, J.D. Litster, S.R. Biggs, T. Howes, Drop Penetration into Porous Powder Beds, J. Colloid Interface Sci. 253 (2002) 353–366. [61]   M. Denesuk, G.L. Smith, B.J.J. Zelinski, N.J. Kreidl, D.R. Uhlmann, Capillary Penetration of Liquid Droplets into Porous Materials, J. Colloid Interface Sci. 158 (1993) 114–120.

[62]   S. Middleman, Modeling Axisymmetric Flows: Dynamics of Films, Jets, and Drops, Academic Press, 1995.

[63]   T. Nguyen, W. Shen, K. Hapgood, Drop penetration time in heterogeneous powder beds, Chem. Eng. Sci. 64 (2009) 5210–5221.

[64]   M.L.M. Oostveen, G.M.H. Meesters, J.R. van Ommen, Quantification of powder wetting by drop penetration time, Powder Technol. 274 (2015) 62–66.

[65]   A. Clarke, T.D. Blake, K. Carruthers, A. Woodward, Spreading and imbibition of liquid droplets on porous surfaces, Langmuir. 18 (2002) 2980–2984.

[66]   V.M. Starov, S.R. Kostvintsev, V.D. Sobolev, M.G. Velarde, S.A. Zhdanov, Spreading of Liquid Drops over Dry Porous Layers: Complete Wetting Case, J. Colloid Interface Sci. 252 (2002) 397–408.

[67]   M. Hilpert, A. Ben-David, Infiltration of liquid droplets into porous media: Effects of dynamic contact angle and contact angle hysteresis, Int. J. Multiph. Flow. 35 (2009) 205–218.

[68]   R.K. Holman, M.J. Cima, S.A. Uhland, E. Sachs, Spreading and Infiltration of Inkjet-Printed Polymer Solution Droplets on a Porous Substrate, J. Colloid Interface Sci. 249 (2002) 432–440.

[69]   H.N. Emady, D. Kayrak-Talay, W.C. Schwerin, J.D. Litster, Granule formation mechanisms and morphology from single drop impact on powder beds, Powder Technol. 212 (2011) 69–79.

[70]   W. Pietsch, Size Enlargement by Agglomeration BT - Handbook of Powder Science & Technology, in: M.E. Fayed, L. Otten (Eds.), Springer US, Boston, MA, 1997: pp. 202–377.

[71]   H. Rumpf, The strength of granules in agglomerates. Agglomeration, Knepper, W.A., (Ed), New York: Wiley Interscience, 1962.

[72]   D. Djuric, P. Kleinebudde, Impact of screw elements on continuous granulation with a twin-screw extruder, J. Pharm. Sci. 97 (2008) 4934–4942.

[73]   H.-J. Sämann, Screw Elements for Co-rotating, Closely Intermeshing, Twin-Screw Extruders, in: Co-Rotating Twin-Screw Extruder, Carl Hanser Verlag GmbH & Co. KG, 2007:

pp. 215–235.

[74]   D. Djuric, P. Kleinebudde, Impact of screw elements on continuous granulation with a twin-screw extruder, J. Pharm. Sci. 97 (2008) 4934–4942.

[75]   M.R. Thompson, J. Sun, Wet granulation in a twin-screw extruder: implications of screw design., J. Pharm. Sci. 99 (2010) 2090–103.

[76]   H. Li, M.R. Thompson, K.P. O'Donnell, Understanding wet granulation in the kneading block of twin screw extruders, Chem. Eng. Sci. 113 (2014) 11–21.

[77]   Y. Liu, M.R. Thompson, K.P. O'Donnell, Function of upstream and downstream conveying elements in wet granulation processes within a twin screw extruder, Powder Technol. 284 (2015) 551–559.

[78]   A.S. El Hagrasy, J.D. Litster, Granulation rate processes in the kneading elements of a twin screw granulator, AIChE J. 59 (2013) 4100–4115.

[79]   B. Van Melkebeke, C. Vervaet, J.P. Remon, Validation of a continuous granulation process using a twin-screw extruder., Int. J. Pharm. 356 (2008) 224–30.

[80]   M.R. Thompson, J. Sun, Wet Granulation in a Twin-Screw Extruder: Implications of Screw Design, J. Pharm. Sci. 99 (2010) 2090–2103.

[81]   K.T. Lee, A. Ingram, N.A. Rowson, Twin screw wet granulation: The study of a continuous twin screw granulator using Positron Emission Particle Tracking (PEPT) technique, Eur. J. Pharm. Biopharm. 81 (2012) 666–673.

[82]   S. Yu, G.K. Reynolds, Z. Huang, M. de Matas, A.D. Salman, Granulation of increasingly hydrophobic formulations using a twin screw granulator, Int. J. Pharm. 475 (2014) 82–96.

[83]   A. Kumar, J. Vercruysse, M. Toiviainen, P.-E. Panouillot, M. Juuti, V. Vanhoorne, C. Vervaet, J.P. Remon, K. V Gernaey, T. De Beer, I. Nopens, Mixing and transport during pharmaceutical twin-screw wet granulation: experimental analysis via chemical imaging., Eur. J. Pharm. Biopharm. Off. J. Arbeitsgemeinschaft Für Pharm. Verfahrenstechnik e.V. 87 (2014) 279–89.

[84]   J. Vercruysse, A. Burggraeve, M. Fonteyne, P. Cappuyns, U. Delaet, I. Van Assche, T. De Beer, J.P. Remon, C. Vervaet, Impact of screw configuration on the particle size distribution of granules produced by twin screw granulation, Int. J. Pharm. 479 (2015) 171–180.

[85]   R. Sayin, A.S. El Hagrasy, J.D. Litster, Distributive mixing elements: Towards improved granule attributes from a twin screw granulation process, Chem. Eng. Sci. 125 (2015) 165–175.

[86]   J. Kirchhoff, Mixing and Dispersing: Principles, in: Co-Rotating Twin-Screw Extruder, Carl Hanser Verlag GmbH & Co. KG, 2007: pp. 159–179.

[87]   R. Rudolf, General Overview of the Compounding Process: Tasks, Selected Applications, and Process Zones, in: Co-Rotating Twin-Screw Extruder, Carl Hanser Verlag GmbH & Co. KG, 2007: pp. 57–89.

[88]   J. Vercruysse, M. Toiviainen, M. Fonteyne, N. Helkimo, J. Ketolainen, M. Juuti, U. Delaet, I. Van Assche, J.P. Remon, C. Vervaet, T. De Beer, Visualization and understanding of the granulation liquid mixing and distribution during continuous twin screw granulation using NIR chemical imaging, Eur. J. Pharm. Biopharm. 86 (2014) 383–392.

[89]   A. Kumar, M. Alakarjula, V. Vanhoorne, M. Toiviainen, F. De Leersnyder, J. Vercruysse, M. Juuti, J. Ketolainen, C. Vervaet, J.P. Remon, K. V. Gernaey, T. De Beer, I. Nopens, Linking granulation performance with residence time and granulation liquid distributions in twin-screw granulation: An experimental investigation, Eur. J. Pharm. Sci. 90 (2016) 25–37.

[90]   R. Meier, M. Thommes, N. Rasenack, K.-P. Moll, M. Krumme, P. Kleinebudde, Granule size distributions after twin-screw granulation – Do not forget the feeding systems, Eur. J. Pharm. Biopharm. 106 (2016) 59–69.

[91]   T. Chan Seem, N.A. Rowson, I. Gabbott, M. de Matas, G.K. Reynolds, A. Ingram, Asymmetric distribution in twin screw granulation, Eur. J. Pharm. Biopharm. 106 (2016) 50–58.

[92]   A. Kumar, J. Dhondt, J. Vercruysse, F. De Leersnyder, V. Vanhoorne, C. Vervaet, J.P. Remon, K. V. Gernaey, T. De Beer, I. Nopens, Development of a process map: A step towards a regime map for steady-state high shear wet twin screw granulation, Powder Technol. 300

(2016) 73–82.

[93]   D. Djuric, P. Kleinebudde, Continuous granulation with a twin-screw extruder: Impact of material throughput, Pharm. Dev. Technol. 15 (2010) 518–525.

[94]   J.G. Osorio, R. Sayin, A. V. Kalbag, J.D. Litster, L. Martinez-Marcos, D.A. Lamprou, G.W. Halbert, Scaling of continuous twin screw wet granulation, AIChE J. (2016).

[95]   L.J. Gorringe, G.S. Kee, M.F. Saleh, N.H. Fa, R.G. Elkes, Use of the channel fill level

[96]   Li, M.R. Thompson, K.P. O'Donnell, Examining drug hydrophobicity in continuous wet granulation within a twin screw extruder., Int. J. Pharm. 496 (2015) 3–11.

[97]   P. Kumar, C. Singh, A Study on Solubility Enhancement Methods for Poorly Water Soluble Drugs, Am. J. Pharmacol. Sci. 1 (2013) 67–73.

[98]   T.H. Nguyen, W. Shen, K. Hapgood, Effect of formulation hydrophobicity on drug distribution in wet granulation, Chem. Eng. J. 164 (2010) 330–339.

[99]   M.X.L. Tan, T.H. Nguyen, K.P. Hapgood, Drug distribution in wet granulation: foam versus spray, J. Drug Dev. Ind. Pharm. 39 (2013) 1389–1400.

[100]   N. Eshtiaghi, B. Arhatari, K.P. Hapgood, Producing hollow granules from hydrophobic powders in high-shear mixer granulators, Adv. Powder Technol. 20 (2009) 558–566.

[101]   S. Yu, G.K. Reynolds, Z. Huang, M. de Matas, A.D. Salman, Granulation of increasingly hydrophobic formulations using a twin screw granulator., Int. J. Pharm. 475 (2014) 82–96.

[102]   H. Li, M.R. Thompson, K.P. O'Donnell, Progression of wet granulation in a twin screw extruder comparing two binder delivery methods, AIChE J. 61 (2015) 780–791.

[103]   Y. Liu, M.R. Thompson, K.P. O'Donnell, N.S. Grasman, Effect of temperature on the wetting behavior of hydroxypropyl methylcellulose in a twin-screw granulator, Powder Technol. 302 (2016) 63–74.

[104]   R. Sayin, A.S. El Hagrasy, J.D. Litster, Distributive mixing elements: Towards improved granule attributes from a twin screw granulation process, Chem. Eng. Sci. 125 (2015) 165–175.

[105]   A.S. El Hagrasy, J.R. Hennenkamp, M.D. Burke, J.J. Cartwright, J.D. Litster, Twin screw wet granulation: Influence of formulation parameters on granule properties and growth behavior, Powder Technol. 238 (2013) 108–115.

[106]   M.J. Adams, M.A. Mullier, J.P.K. Seville, Agglomerate strength measurement using a uniaxial confined compression test, Powder Technol. 78 (1994) 5–13.

[107]   E.M. Davis, R.J. Davis, Fundamentals of Chemical Reaction Engineering, 2003.

[108]   J.B. Lee, S.H. Lee, Dynamic wetting and spreading characteristics of a liquid droplet impinging on hydrophobic textured surfaces., Langmuir. 27 (2011) 6565–73.

[109]   C. Grzelakowski, D. Ben Jazia, B. Lebeau, L. Vonna, D. Dupuis, H. Haidara, On the influence of pore structure on the free-imbibition of sessile drops into nanoporous substrates, Langmuir. 25 (2009) 5855–5860.

[110]   S.K. Singh, S. Khandekar, D. Pratap, S.A. Ramakrishna, Wetting dynamics and evaporation of sessile droplets on nano-porous alumina surfaces, Colloids Surfaces A Physicochem. Eng. Asp. 432 (2013) 71–81.

[111]   C. Mangwandi, L. JiangTao, A.B. Albadarin, R.M. Dhenge, G.M. Walker, High shear granulation of binary mixtures: Effect of powder composition on granule properties, Powder Technol. 270 (2015) 424–434.

[112]   K.P. Hapgood, J.D. Litster, R. Smith, Nucleation regime map for liquid bound granules, AIChE J. 49 (2003) 350–361.

[113]   H. Charles-Williams, R. Wengeler, K. Flore, H. Feise, M.J. Hounslow, A.D. Salman, Granulation behaviour of increasingly hydrophobic mixtures, Powder Technol. 238 (2013) 64–76.

[114]   A. Kumar, J. Vercruysse, V. Vanhoorne, M. Toiviainen, P.-E. Panouillot, M. Juuti, C. Vervaet, J.P. Remon, K. V. Gernaey, T. De Beer, I. Nopens, Conceptual framework for model-based analysis of residence time distribution in twin-screw granulation, Eur. J. Pharm. Sci. 71 (2015) 25–34.

[115]   H. Li, M.R. Thompson, K.P. O'Donnell, Understanding wet granulation in the kneading block of twin screw extruders, Chem. Eng. Sci. 113 (2014) 11–21.

[116] F. Lai, J.A. Hersey, J.N. Staniforth, Segregation and mixing of fine particles in an ordered mixture, Powder Technol. 28 (1981) 17–23.

[117] J.J. McCarthy, Turning the corner in segregation, Powder Technol. 192 (2009) 137–142.

[118] K.T. Lee, A. Ingram, N.A. Rowson, Comparison of granule properties produced using Twin Screw Extruder and High Shear Mixer: A step towards understanding the mechanism of twin screw wet granulation, Powder Technol. 238 (2013) 91–98.

[119] S. Oka, H. Emady, O. Kašpar, V. Tokárová, F. Muzzio, F. Štěpánek, R. Ramachandran, The effects of improper mixing and preferential wetting of active and excipient ingredients on content uniformity in high shear wet granulation, Powder Technol. 278 (2015) 266–277..

[120] S. Oka, D. Smrčka, A. Kataria, H. Emady, F. Muzzio, F. Štěpánek, R. Ramachandran, Analysis of the origins of content non-uniformity in high-shear wet granulation, Int. J. Pharm. 528 (2017) 578–585..

[121] T. Koide, T. Nagato, Y. Kanou, K. Matsui, S. Natsuyama, T. Kawanishi, Y. Hiyama, Detection of component segregation in granules manufactured by high shear granulation with over-granulation conditions using near-infrared chemical imaging, Int. J. Pharm. 441 (2013) 135–145.

[122] M. Manley, Near-infrared spectroscopy and hyperspectral imaging: non-destructive analysis of biological materials, Chem. Soc. Rev. 43 (2014) 8200–8214.

[123] G. Reich, Near-infrared spectroscopy and imaging: Basic principles and pharmaceutical applications, Adv. Drug Deliv. Rev. 57 (2005) 1109–1143.

[124] J.M. Amigo, C. Ravn, Direct quantification and distribution assessment of major and minor components in pharmaceutical tablets by NIR-chemical imaging, Eur. J. Pharm. Sci. 37 (2009) 76–82.

[125] O. Scheibelhofer, D.M. Koller, P. Kerschhaggl, J.G. Khinast, Continuous powder flow monitoring via near-infrared hyperspectral imaging, 2012 IEEE I2MTC - Int. Instrum. Meas. Technol. Conf. Proc. (2012) 748–753.

[126] J. Vercruysse, M. Toiviainen, M. Fonteyne, N. Helkimo, J. Ketolainen, M. Juuti, U.

Delaet, I. Van Assche, J.P. Remon, C. Vervaet, T. De Beer, Visualization and understanding of the granulation liquid mixing and distribution during continuous twin screw granulation using NIR chemical imaging, Eur. J. Pharm. Biopharm. 86 (2014) 383–392.

[127] P.R. Wahl, I. Pucher, O. Scheibelhofer, M. Kerschhaggl, S. Sacher, J.G. Khinast, Continuous monitoring of API content, API distribution and crushing strength after tableting via near-infrared chemical imaging, Int. J. Pharm. 518 (2017) 130–137. doi:10.1016/j.ijpharm.2016.12.003.

[128] T. Koide, Y. Yamamoto, T. Fukami, N. Katori, H. Okuda, Y. Hiyama, Analysis of Distribution of Ingredients in Commercially Available Clarithromycin Tablets Using Near-Infrared Chemical Imaging with Principal Component Analysis and Partial Least Squares, Chem. Pharm. Bull. (Tokyo). 63 (2015) 663–668..

[129] A. Kumar, M. Alakarjula, V. Vanhoorne, M. Toiviainen, F. De Leersnyder, J. Vercruysse, M. Juuti, J. Ketolainen, C. Vervaet, J.P. Remon, K. V. Gernaey, T. De Beer, I. Nopens, Linking granulation performance with residence time and granulation liquid distributions in twin-screw granulation: An experimental investigation, Eur. J. Pharm. Sci. 90 (2016) 25–37.

[130] E. Klotz, M. Wimmer-teubenbacher, O. Scheibelhofer, H. Scharfetter, W. Hsiao, S. Stegemann, Quantification of Printed Metformin Hydrochloride using NIR Spectroscopy, (n.d.) 17–18.

[131] A. Kumar, J. Vercruysse, M. Toiviainen, P.-E. Panouillot, M. Juuti, V. Vanhoorne, C. Vervaet, J.P. Remon, K. V. Gernaey, T. De Beer, I. Nopens, Mixing and transport during pharmaceutical twin-screw wet granulation: Experimental analysis via chemical imaging, Eur. J. Pharm. Biopharm. 87 (2014) 279–289.

[132] A.C. Scott, M.J. Hounslow, T. Instone, Direct evidence of heterogeneity during high-shear granulation, Powder Technol. 113 (2000) 205–213.

[133] M. Verstraeten, D. Van Hauwermeiren, K. Lee, N. Turnbull, D. Wilsdon, M. am Ende, P. Doshi, C. Vervaet, D. Brouckaert, S.T.F.C. Mortier, I. Nopens, T. De Beer, In-depth experimental analysis of pharmaceutical twin-screw wet granulation in view of detailed process understanding, Int. J. Pharm. 529 (2017) 678–693.

11 APPENDIX

11.1 Appendix A: Calculating Screw Element Free Volume

The total bulk V_{free} of the various screw elements was calculated from the cross-sectional area of TSG, (see Figure 11-1 and Table 11-1).
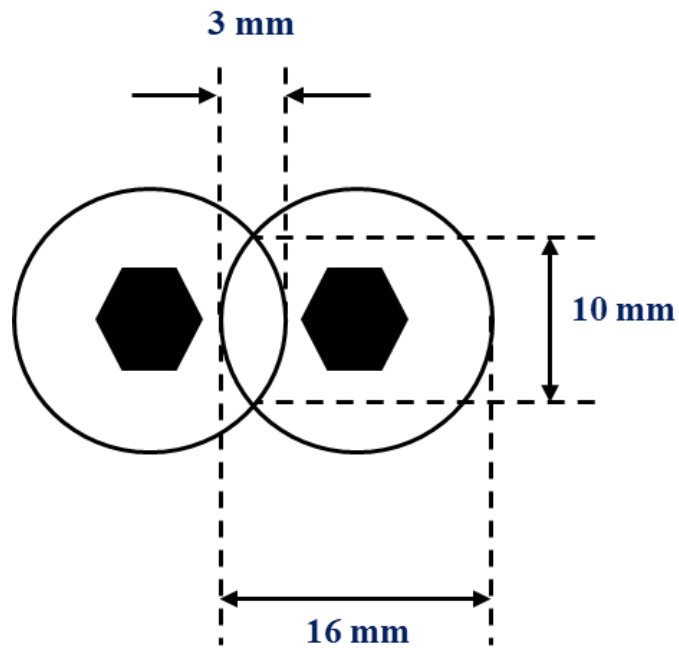

Figure 11-1. Cross-sectional area of TSG.

Table 11-1. Screw Element V_{free} of various screw elements

Area of ellispe	πab	23.55	mm^2
Area of a circle	πr^2	200	
Area of TSG	$2\pi r^2 - \pi ab$	378	
Area of triangle in the hexagonal	$\frac{1}{2}bh$	5.73	
Area of hexagonal	Area of triangle*6	34.37	
Volume CE	Water displacement	1	mm^3
Volume ICE		0.875	
Volume fCE		0.75	
Volume KE		0.26	
Volume nTME		0.225	
Volume wTME		0.4625	
V_{free} CE	Area of TSG*D-	5.50	cm^3
V_{free} ICE	Area of hexagonal*D-	5.50	
V_{free} fCE	Volume of Element	5.50	
V_{free} KE		1.38	
V_{free} nTME		1.38	
V_{free} wTME		2.75	

11.2 Appendix B: Mean residence time, toqrue and free volume for Chapter 8

Table 11-2. Data for liquid binder μ =1.0 m Pa s

Zone	Mean residence time (s)	Torque (Nm)	Free Volume (mm³)
1	8.20±0.2	2.60±0.1	54512
2	13.70±0.5	2.87±0.02	72684
3	23.28±0.1	5.60±0.4	90854
4	35.88±1.2	12.7±0.5	109025
5	40.92±0.9	19.0±0.4	127196

Table 11-3. Data for liquid binder μ =3.10 m Pa s

Zone	Mean residence time (s)	Torque (Nm)	Free Volume (mm³)
1	8.20±0.2	2.60±0.1	54512
2	13.70±0.5	2.87±0.02	72684
3	23.28±0.1	5.60±0.4	90854
4	35.88±1.2	12.7±0.5	109025
5	40.92±0.9	19.0±0.4	127196

Table 11-4. Data for liquid binder μ =9.40 m Pa s

Zone	Mean residence time (s)	Torque (Nm)	Free Volume (mm³)
1	8.20±0.2	2.6±0.1	54512
2	13.70±0.5	2.87±0.02	72684
3	23.28±0.1	5.6±0.4	90854
4	35.88±1.2	12.7±0.5	109025
5	40.92±0.9	19±0.4	127196